INJECTION-LOCKED OPTICALLY PUMPED SEMICONDUCTOR LASER

by

Yi-Ying Lai

A Dissertation Submitted to the Faculty of the

DEPARTMENT OF OPTICAL SCIENCES

In Partial Fulfillment of the Requirements

For the Degree of

DOCTOR OF PHILOSOPHY

In the Graduate College

THE UNIVERSITY OF ARIZONA

2015

THE UNIVERSITY OF ARIZONA
GRADUATE COLLEGE

As members of the Dissertation Committee, we certify that we have read the dissertation prepared by Yi-Ying Lai, titled Injection-Locked Optically Pumped Semiconductor Laser and recommend that it be accepted as fulfilling the dissertation requirement for the Degree of Doctor of Philosophy.

_____ Date: 05/29/15
Dr. Yushi Kaneda

_____ Date: 05/29/15
Dr. R. Jason Jones

_____ Date: 05/29/15
Dr. Jerome V. Moloney

Final approval and acceptance of this dissertation is contingent upon the candidate's submission of the final copies of the dissertation to the Graduate College.

I hereby certify that I have read this dissertation prepared under my direction and recommend that it be accepted as fulfilling the dissertation requirement.

_____ Date: 05/29/15
Dissertation Director: Yushi Kaneda

_____ Date: 05/29/15
Dissertation Director: R. Jason Jones

STATEMENT BY AUTHOR

This dissertation has been submitted in partial fulfillment of the requirements for an advanced degree at the University of Arizona and is deposited in the University Library to be made available to borrowers under rules of the Library.

Brief quotations from this dissertation are allowable without special permission, provided that an accurate acknowledgement of the source is made. Requests for permission for extended quotation from or reproduction of this manuscript in whole or in part may be granted by the head of the major department or the Dean of the Graduate College when in his or her judgment the proposed use of the material is in the interests of scholarship. In all other instances, however, permission must be obtained from the author.

SIGNED: Yi-Ying Lai

ACKNOWLEDGEMENTS

I would like to express my sincere gratitude to Dr. Yushi Kaneda for his patience and valuable guidance throughout my research and writing of this dissertation. Dr. Jerome V. Moloney's kind support and advice were indispensable in setting my path in the optic world. Dr. R. Jason Jones provided me with insightful suggestions on the dissertation.

Many people at University of Arizona have been a huge help. Dr. J. M. Yarborough offered timely encouragement throughout my graduate study. It has been my privilege to work with Yevgeniy Merzlyak and Kevin Winn in the lab. Their support made this dissertation possible. I also would like to thank Dr. Alexandre Laurain and Dr. Jorg Hader for sharing their insights and experiences on the simulations and experiments.

I would like to give special thanks to my amazing friends in Tucson, Taiwan and worldwide who accompanied me over the years and shared many cherish moments with me. And I cannot spare Chia-Ling Li and Wei-Liang Hsu acknowledgements for their generous accommodation.

I would like to express my deepest appreciation to my husband, Ting-Kai Huang, my parents, Hsin-Hsiung Lai and Yueh-Chin Chang, and my other family members for their lifelong love and dedication. I couldn't have travelled this far and accomplished this much without any of you.

TABLE OF CONTENTS

LIST OF FIGURES

LIST OF FIGURES - *Continued*

LIST OF FIGURES - *Continued*

LIST OF FIGURES - *Continued*

LIST OF FIGURES - *Continued*

LIST OF TABLES

ABSTRACT

High-power, single-frequency, narrow-linewidth lasers emitting at tailored wavelength are desired for many applications, especially for precision spectroscopy. By way of a free-space resonator, optically pumped semiconductor lasers (OPSLs), a.k.a. vertical external-cavity surface-emitting lasers (VECSELs), can provide near diffraction-limited, high-quality Gaussian beams and are scalable in output power. Free space resonators also allow the insertion of the birefringent filter and the etalon to enforce single-frequency operation. In addition, the emission wavelengths of OPSLs are tailorable through bandgap engineering. These advantages above make OPSL a strong candidate of laser sources for spectroscopic applications including atomic spectroscopy as well as optical lattice clocks.

In this research, a single-frequency laser source with high power is demonstrated by applying the injection-locking technique on OPSLs for the first time. The behaviors of the injection-locked OPSL are studied by varying parameters such as output coupling, injection wavelengths and injection power. It was found that the best injection wavelength is by approximately 2 nm shorter than the free-running slave laser at any given pump power. Below the lasing threshold for free-running operation, the laser starts the stimulated emission process as soon as it is pumped, working as a resonant amplifier.

With proper parameters, the output power of the injection-locked laser exceeds the output power of its free-running condition. Over 9 W of single-frequency output power at 1015 nm is achieved. The output beam is near-diffraction-limited with M_x^2 = 1.04 and M_y^2 = 1.02. By analyzing the surface photoluminescence (PL) and the output performance of the laser, the saturation intensity of OPSLs is estimated to be 100 kW/cm^2 when the passive loss of 1.4% is assumed. The injection-locked system adds fairly low phase noise to that of the master laser. By measuring the beat note between the master laser and the injection-locked laser, The RMS values of the phase noise are 0.112 rad and 0.081 rad when using the T = 3% and T = 4% output couplers respectively .

CHAPTER 1 INTRODUCTION

Many scientific studies such as atom cooling, atom trapping and atomic spectroscopy require narrow linewidth laser sources at specific wavelengths. Some of these wavelengths that are in the visible to ultraviolet (UV) region can be accessed by frequency doubling or quadrupling of a near-infrared light. However, in many cases, it is not achievable with either conventional bulk solid-state lasers or fiber-based laser sources since their emission wavelengths are restricted to the transitions of ions with discrete values. On the other hand, semiconductor lasers are capable of operation at tailored wavelength by way of bandgap engineering. However, conventional diode lasers are limited in power mainly because of the catastrophic optical damage (COD) on the emitting edge. Tapered amplifiers can yield a few hundred mW to a few W of output power, but their output beams are usually not diffraction limited, preventing efficient frequency conversion that must be performed in external optical resonators or in waveguide devices, both of which require near diffraction-limited output beams. Therefore, it is desirable to develop a laser source that can tailor its wavelength to cover the desired wavelength range, and also exhibit some other essential properties such as good beam quality, sufficient output power and high efficiency.

Optically pumped semiconductor lasers (OPSLs), also known as vertical external-cavity surface-emitting lasers (VECSELs), or semiconductor disk lasers

(SDLs), provide the possibility of tailoring the desired wavelength through bandgap engineering and proper wafer growth [1], [2], similar to conventional diode lasers. By controlling the semiconductor material composition, the available wavelengths of the lasers based on semiconductor materials cover from several hundred nm to several tens of microns. To date, the demonstrated fundamental wavelengths of OPSLs range from ~390 nm (based on the GaN/InGaN system) [3], [4], 674 nm (based on the GaInP/AlGaInP/GaAs material system) [5] to ~5 μm (based on the PbTe material system) [6], [7]. Deep ultraviolet (DUV) generation at 244 nm was demonstrated by the fourth harmonic generation of a 976 nm OPSL [8]. OPSLs can generate near diffraction-limited output by selectively pumping the TEM_{00} mode area given by the external cavity. Mode selection elements can be inserted to enforce single-frequency operation. By adjusting the cavity length with a piezoelectric actuator, fast and fine frequency tuning can be accomplished. Fast tuning allows the frequency to be stabilized to an external reference, such as spectroscopic references or reference cavities. The output power is scalable with different pump spot sizes to some extent [9], [10]. With proper design of wafer structure and heat management, the output power of OPSLs can reach over 100 W in multi-transverse mode [11], and several tens of watts in single transverse mode operation [12]–[14].

Our approach to a high-power single-frequency laser is by using an OPSL with the injection-locking technique. To achieve this goal, one may also directly

stabilize a high power laser [13], [14]. However, when stabilizing a high power laser, intracavity elements are required to maintain a single longitudinal mode, which will introduce loss into the high power laser cavity and reduce the output efficiency. Therefore, it is simpler and more efficient to accomplish two different goals, single-frequency operation and high-power operation, separately. The simplicity of the slave laser oscillator, which does not require longitudinal mode selection, would compensate for the complexity of the locking scheme. A single laser oscillator to achieve simultaneously single frequency operation and high power operation will lead to a complex optical configuration, and the longitudinal mode spacing would be small because of the large cavity length to accommodate a reasonably large cavity mode size. Smaller longitudinal mode spacing increases the likelihood of mode hopping in case of mechanical/temperature drift. By separating the functions into two lasers through the injection-locking technique, two objectives are individually addressed. One laser, which can also be an OPSL, serves as the master laser equipped with frequency selective elements such as a birefringent filter and/or an etalon in order to provide stable and single-frequency signal with the ability of wavelength tuning to the desired wavelength. The other OPSL is the slave laser that generates high power in its free-running mode with no need of inserting mode selection elements, but with the ability to adjust the cavity length to change its resonant frequency. As the light from the master laser is injected into the slave laser, the lasing frequency of the slave laser is forced to that of the injected signal, by matching the resonant

frequency of the slave laser cavity to the injected signal using an electronic feedback loop and an actuator.

In this research, an injection-locked OPSL is demonstrated for the first time to our knowledge, and the key factors to operate an injection-locked OPSL are discussed. The output performance of the injection-locked laser is investigated by varying some important parameters such as output coupling, injection wavelengths with respect to the gain peak of the slave laser and injection power. Also, the relative phase noise between the master laser and slave laser is analyzed to verify the stability of the injection-locked laser system. This study involves work in multiple disciplines; laser physics, optics, electronics, mechanical engineering as well as control theory.

1.1 Evolution of semiconductor lasers: from laser diodes to OPSLs

Semiconductor lasers emerged in 1962 [15]–[18]. Several groups developed the earliest laser diodes nearly simultaneously with the active region in the form of simple p-n homojunction structures. In 1970s, double heterostructure lasers were developed that lowered the threshold current density and operate continuously at room temperature [19]. To fabricate these devices, liquid phase epitaxy (LPE) was widely used. The LPE process has a high deposition rate that is suitable for mass production. However, nonuniformity of the layer thickness and roughness of the device surface were some of the

problems which limited the output performance of the laser [20], [21]. Later, the introduction of metalorganic chemical vapor deposition (MOCVD) and molecular beam epitaxy (MBE) growth processes enabled the scientists to accurately control the thickness of the atomic layers well below 10 nm, which enable the growth of the quantum well structure [22]. The advent of the quantum well lasers [23] was a breakthrough. With narrow active layers along with waveguide structure, quantum well lasers require fewer injected carriers compared to the lasers with bulk active layers, and therefore the internal loss is reduced. Lower internal losses result in lower threshold current density and much better output efficiency. Furthermore, the lasing wavelength of quantum well lasers can be varied by changing the material composition and the thickness of the quantum wells, which becomes advantageous for modern semiconductor laser operation [24].

Conventional semiconductor lasers have two main schemes: edge-emitting lasers and surface-emitting lasers. The edge-emitting lasers, or edge-emitters, emit light from the edge of the semiconductor chip. The laser oscillates in the resonator formed by the two end-facets of the semiconductor material and is confined along the growth direction by a waveguide structure. Due to the asymmetric geometry, the output beam is elliptical with a large angle of divergence parallel to the growth direction. For single-transverse-mode operation, the dimension of waveguide structure is restricted to a few microns. Furthermore, edge emitters tend to suffer from catastrophic optical damage (COD) [25], which

causes the device surface to be thermally damaged by the laser light, and therefore limits the operating power. To avoid COD and to scale the output power, broad area laser diodes were built. The power scaling concept can be expanded to single-stripe edge-emitters. Further, multiples of stripe edge-emitters can be bundled to form multiple-stripe laser bars with output power up to several hundred watts [26]. However, the output is the incoherent sum of emission of multiple emitters, so the output beam quality is poor, the brightness (intensity per unit solid angle) is not high, and they have a relatively wide spectrum. These multi-mode lasers are suitable for optical pumping of other solid-state lasers where a diffraction-limited beam is not needed or the combined spectrum does not need to be narrow. For the pumping of industrial lasers, these diode bars and modules have been driven to lower the cost and improve their reliability. Pump diodes used in this study are of this kind.

Vertical-cavity surface-emitting lasers (VCSEL) emit light perpendicularly to the grown surfaces of the semiconductor structure. The laser cavity is formed between a pair of epitaxially grown distributed Bragg reflectors (DBR). With this geometry, a circular output beam can be demonstrated with a lower divergence angle compared to edge-emitters. In order to operate in a single transverse mode, the output beam diameter of the VCSEL is limited to several tens microns, and thereby the output power is at the level of several milliwatts. To solve this, a group in Novalux, Inc. [27] developed electrically-pumped surface emitting lasers where the laser transverse mode is controlled by an extended cavity. This kind of

laser now is often referred to as a Novalux Extended-Cavity Surface-Emitting Laser (NECSEL). The beam diameter of NECSELs can be scaled as large as hundreds of microns and generate 500 mW of CW power in a TEM_{00} mode. Even with the extended cavity, there is still a limitation to push the output power to higher power levels. Since VCSELs and NECSELs are driven by current across the wafer, the main problem in power scalability is the electrical pumping over a large area.

OPSLs, or VECSELs were developed in the 1990s [28]–[30] to realize high power with single transverse mode operation. Similar to NECSELs, OPSLs have an extended cavity to manipulate the cavity mode. Also, OPSLs adopt the feature of thin-disk lasers [31] in which a thin, disc-shaped gain medium is mounted on a heat sink, minimizing the temperature gradient in the direction perpendicular to optical axis and the phase distortion along the beam propagation direction [32], [33]. In addition, OPSLs are optically-pumped by high-power laser diodes. There are two main advantages of optical-pumping. Firstly, the devices can be grown with undoped semiconductor materials. There is no need of p-n junctions or electric contacts, which not only simplifies the growth process compared to the electrically-pumped devices, but also reduces the optical loss caused by the free carrier absorption. Secondly, the pump spot can be easily scaled to large sizes with uniform carrier density distribution, as opposed to the electrically-pumped lasers. Combined with the external cavity, high power output in a near diffraction limited beam is realized. Even though the OPSL is still a fairly new type of laser

source given its short history, it has been extensively studied in various applications including high power CW generation [11], ultrashort pulse generation [34], intracavity frequency conversion [8], [35], [36] and the single-frequency [37], [38]. With versatile properties, we can expect that OPSLs become more and more attractive in different fields.

1.2 OPSLs applications on atomic spectroscopy

Atomic spectroscopy is the subject of studying the interaction between light and matter by characteristic spectra. OPSLs have been previously utilized in different applications related to atomic spectroscopy [39]–[43]. For instance, intracavity laser absorption spectroscopy (ICLAS) is a highly sensitive technique for studying the absorption spectrum of different materials [39], [40]. OPSLs are particularly suitable for ICLAS because of their low intracavity loss and wide gain bandwidth. Detection sensitivities as low as 10^{-9} to 10^{-10} cm^{-1} were achieved. In Ref. [41], a single-frequency OPSL emitting near 852 nm is used for cesium atomic clock experiments. The laser source has a tuning range of 9 nm by tilting an etalon. Furthermore, fine tuning is obtained by tuning the cavity length with a piezoelectric ceramic. With over 10GHz of continuous tunability, the laser can resolve the hyperfine level of the cesium D_2 line.

For atomic transitions in the UV region, OPSLs are favorable laser sources for atomic cooling and trapping. For example, the 6^1S_0-6^3P_1 transition of mercury

(Hg) is at 253.7 nm. To form a magneto-optical trap (MOT) [44] or optical molasses[45], a single-frequency coherent light source is needed. In ref [42], [43], an OPSL is frequency quadrupled to 253.7 nm, and three pairs of counter-propagating laser beams are incident along 3 Cartesian axes to form optical molasses that cool the neutral Hg atoms. Doppler-free spectroscopy of the Hg ground state has been successfully demonstrated.

A group in the University of Tokyo proposed an optical lattice clock based on neutral atoms that can reach accuracy better than 10^{-18} [46], [47]. Hg is so far the heaviest nonradiative atom to be trapped. An atom with high atomic number reduces susceptibility to the blackbody radiation field. The energy level diagram of Hg is shown in Figure 1.1. As it was mentioned above, the spin-forbidden transition at 253.7 nm provides a suitable cooling transition with a natural linewidth of 1.3 MHz. The optical lattice clock is created by the interference pattern of lasers at 360 nm, the “magic wavelength” that a dipole field does not disturb the eigen frequency of atoms.

One purpose in this research is to investigate the potential of OPSLs for the applications such as an atomic trapping laser source for optical lattice clocks, which requires high power, near diffraction limited output at a tailored wavelength with the possibility of frequency stabilization. For this application to be realized, a few hundred mW of power at 253.7 nm is required. Therefore, several watts of

single-frequency power at a fundamental wavelength of 1014.9 nm would be sufficient for this application.

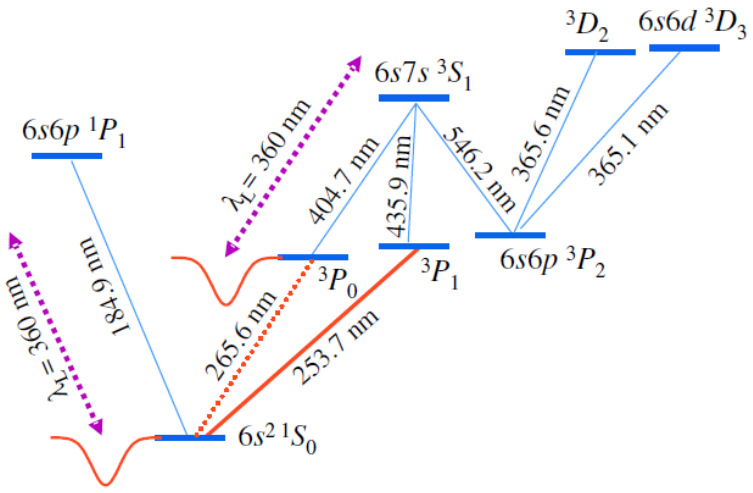

Figure 1.1. Energy-level diagram for Hg[47].

CHAPTER 2 BACKGROUND STUDY

2.1 Basic operating principles of OPSLs

2.1.1 OPSL Structure and operating principles

A typical OPSL wafer consists of functional layers of a resonant periodic gain (RPG) [48] structure and a distributed Bragg reflector (DBR). The basic structure is illustrated in Figure 2.1. The RPG structure is the active region of the laser, with periodic layers of quantum wells and barriers. The DBR serves as one of the high reflectance mirrors of the laser cavity. The DBR consists of dielectric materials with alternating high and low refractive index layers with thicknesses that are one quarter of the design wavelength.

In RPG layers, the quantum wells (QWs) with smaller bandgap energy are embedded in the larger bandgap layers that are called barrier layers. The spacing between each QW is made such that the optical thickness between the wells equals the quarter wave to align with the antinode of the electronic field standing wave of the desired wavelength in the gain medium. On top of the RPG structure is a surface barrier, or a window layer, with higher bandgap to avoid carriers diffusing to the air-semiconductor interface and to protect the semiconductor surface from oxidation.

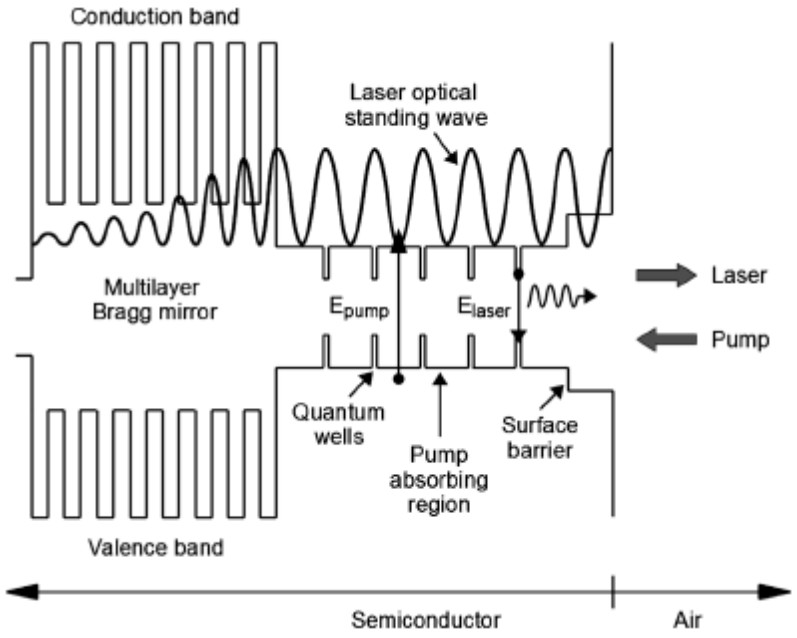

Figure 2.1 The basic structure of OPSLs [49]

There are two approaches in terms of pumping path: in-well pumping and barrier-pumping. For in-well pumping, the pump wavelength can be chosen to be very close to the laser wavelength. The pump absorption and the electron-hole pair recombination both take place in the quantum wells. The quantum defect, i.e. the energy difference between the pump and the laser photons, is very small. Thus, the efficiency can be higher than a barrier-pumped device. The effect of quantum defect is more significant in laser sources with long wavelengths, since the wavelength of the available diode pump sources are mostly shorter (0.8 μm to 1 μm). In ref [50], a 2.3-μm laser achieved 25% optical efficiency using a pump wavelength of 1.96 μm.

A main drawback of in-well pumping is low pump absorption. Since QWs are only several nm thick, the absorption of the pump is low. Typically, less than 20% of the pump power is absorbed in a single pass for an InGaAs based structure. To address this, one method is to place the QWs at the common antinodes of both the pump field and the laser field or where the antinodes of both fields at different wavelengths are close to each other. This requires delicate design and growth control of the active region. Another method is the use of multi-pass pump to recycle the unabsorbed pump as is done with Yb:YAG thin-disk lasers [51]. For this, the DBR needs to have high reflectivity region that covers both the pump and the laser wavelengths. By applying the above strategies [52], the pump absorption can be improved to 80%. Slope efficiency of 67% and optical efficiency of 55% (calculated from absorbed pump power) was achieved by GaAs-AlGaAs OPSLs emitting at 865 nm. The pump wavelength at 833 nm in this case is very close to the QW band edge at 837 nm.

For a barrier-pumped device, the pump is mainly absorbed in the barrier layers. The exited electron-hole pairs diffuse to the QWs. Then, the carriers recombine in the QWs and emit photons. The quantum defect is the main issue in a barrier-pumped device. For a 1-μm laser using 808 nm pump source, the quantum defect is around 20%. Since the pump is absorbed in the barrier layers that are much thicker than the thickness of the QWs, strong pump absorption can be realized. In addition, a barrier pumped device is insensitive to the pump wavelength since majority of the pump is absorbed in the barrier, and hence any

pump light with photon energy larger than the band gap of the barrier can be absorbed, regardless of the standing wave pattern of the pump.

Due to the high refractive index of a semiconductor material, the interface between air and the OPSL chip acts as a partial reflector and a microcavity is formed between the air-semiconductor interface and the DBR. In such a case, the gain spectrum of an OPSL is influenced by both the QW bandgap and the microcavity resonance, which are temperature dependent. The gain peak of the QW shifts at a higher rate than the microcavity to longer wavelengths. Thus, an OPSL is typically designed with the QW gain peak several tens of nm shorter than the microcavity resonant peak at room temperature [2]. For instance, the gain peak of a 1-μm device (InGaAs/GaAs) shifts at a rate that is around 0.3 nm/K and the microcavity resonance shifts at approximately 0.1 nm/K. When the laser is operating, the device temperature typically rises by several tens of degrees C before the thermal rollover, the condition where the QW gain peak becomes spectrally misaligned with the microcavity resonance, and hence, the laser emits at the desired wavelength with sufficient output power. In some circumstances, an anti-reflection (AR) coating can be applied to the OPSL surface, not only to decrease pump reflection loss but also to reduce the microcavity effect for better wavelength manipulation.

2.1.2 OPSL cavity configuration

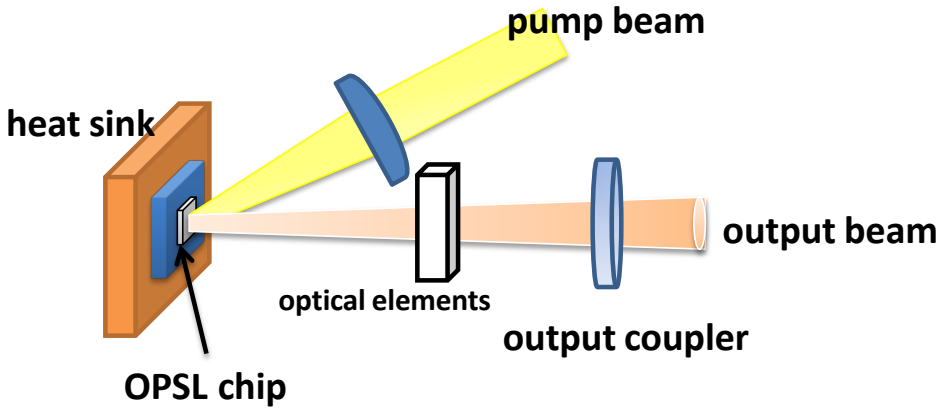

Figure 2.2 The basic laser cavity of OPSLs

Compared to conventional semiconductor lasers, OPSLs are promising for the excellent beam quality because of the external cavity geometry. The configurations of OPSL cavities are versatile. Figure 2.2 shows a simple two-mirror cavity formed by DBR of the OPSL chip and a concave mirror. The mode waist of the plane-concave optical cavity is at the OPSL chip. The fundamental TEM_{00} mode diameter with absence of thermal focusing is given by:

$$w^2 = \frac{4\lambda L}{\pi}\sqrt{(R-L)/L} \qquad (2.1)$$

where L is the cavity length and R is radius of the curved mirror. The cavity mode can be scaled by adjusting the cavity length and the curvature of the mirror. Power scaling is accomplished by enlarging the pump spot to some extent [53].

In some applications, there are also three-mirror V-shaped cavities [8], [54], four-mirror Z-shaped cavities [55] and ring cavities (which is adopted in this study as the slave laser) for more flexibility in manipulation of the cavity transverse mode or insertion of intracavity elements.

The external cavity geometry enables the OPSL to be operated similarly as conventional solid-state lasers for different applications. One can simply insert optical elements inside the laser cavity, such as an etalon or a birefringent filter for single-frequency operation or wavelength tuning, nonlinear crystals for frequency conversion [8], [35] and semiconductor saturable absorber mirrors (SESAMs) for mode-locking to generate ultra-short pulses [34].

Fiber-coupled laser diodes are commonly used as the pump source since the emission pattern of diodes is asymmetric with large angle of divergence along one direction. Through fiber coupling, the output becomes symmetric and easier to utilize on the laser chip. The pump profile at the output of the fiber is imaged onto the OPSL surface by coupling lenses and overlapped with the cavity mode to yield high efficiencies. For single transverse mode operation, the pump spot size at the OPSL chip approximately matches the size of cavity mode [56].

Wafer growth of OPSLs is mostly realized with molecular beam epitaxy (MBE) [57], [58] or metal-organic vapor-phase epitaxy (MOVPE) [56], [59]. A common method of growth is to deposit the semiconductor material in reverse order on the substrate by depositing first the window layer, then the RPG

structure, and the DBR. The epitaxial growth requires very delicate control of the material composition, thickness and strains. After completing the growth, the wafer is cleaved into chips with size of several square millimeters. A heat spreader with high thermal conductivity such as diamond or silicon carbide (SiC) is soldered on the DBR side. After bonding, the substrate is removed by a chemical wet-etching process. Figure 2.3 shows a device, consisting of the semiconductor structure bonded to a diamond heat spreader and mounted on a water-cooled copper heat sink with a piece of Indium foil in between to ensure a good thermal contact.

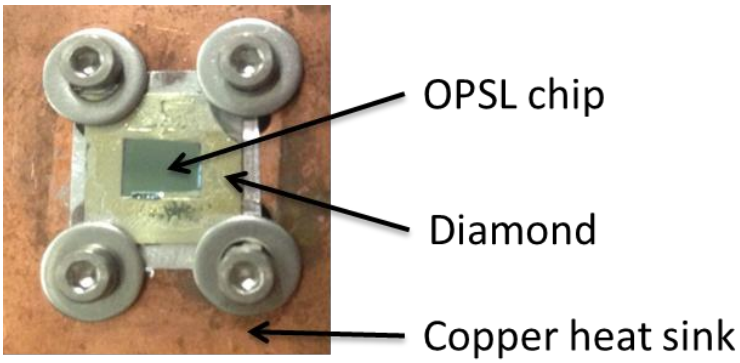

Figure 2.3 An OPSL device on a copper heat sink. The dimension of the diamond is 10 mm x 10 mm x 0.5 mm.

Some OPSL wafers are grown with the DBR layers next to the substrate, followed by the RPG and window layer. For this case, a highly transparent, single

crystalline heat spreader is directly contacted to the top surface of the OPSL through capillary bonding [60] for thermal management. The thermal path of the direct contact bonding is shorter, and the output efficiency is in principle better due to the heat transfer efficiency. However, the intracavity heat spreader needs to have excellent transparency and low scattering loss in order to minimize cavity loss. In addition, the polarization state of the laser cavity is affected by the residual birefringence of the intracavity heat spreader, so that extra loss could be introduced when a Brewster plate or a birefringent filter is inserted inside the cavity [61]. In practice, capillary bonding requires the wafer surface to be smooth without defects. Even a thin air gap between the heat spreader and the chip will introduce high temperature rise and reduce the heat removal efficiency, as well as the optical loss that influences the laser performance [62].

The selection between the two thermal management approaches usually depends on the material systems. The power scalability of OPSLs is limited by the temperature rise in the active region. The heat flow to the bottom heat-spreader passes through the DBR of laser device. Therefore, thermal effect is more significant for the material with high thermal impedance. Ref. [63] compares the two thermal management approaches between a GaSb-based device for 2.3 μm and an InGaAs-based device for 1 μm [64]. For the 1-μm wavelength emitting device, the temperature rise at the center of the device of the two approaches has little difference (2 K). By contrast, the temperature rise of the bottom heat-spreader becomes significant (more than 200 K) for the 2.3-μm

device. This is not only due to the quantum defect, but also the high thermal impedance of the DBR, which is caused by both the thermal conductivity and the thickness of the DBR. The thermal conductivity of DBR of the 2.3-μm device and 1-μm device are 0.01 W/mm·K and 0.06 W/mm·K, respectively. In addition, the total thickness of the DBR of the 2.3-μm device is about 1.4 times higher than that of 1-μm device. As a result, the thermal impedance of the DBR for the long wavelength device is higher and thereby the top heat-spreader configuration is more favorable for the 2.3-μm device.

2.1.3 Wavelength versatility through semiconductor materials and nonlinear optical conversions

Based on the compound semiconductor material system, the wavelengths of OPSLs are versatile through bandgap engineering and temperature control. Unlike the growth of the epitaxial layer of single compound on crystalline substrates, the growths of alloys by mixing two or more compounds allow semiconductor lasers to emit at wavelengths over continuous spectrum regions. Figure 2.4 shows the bandgap energy as a function of the lattice constant of the possible alloys composed of III-V compounds that are most commonly used. By selecting the material composition, the available wavelength ranges cover from several hundred nm to several microns. Using alloys composed of GaAs, AlAs, InAs and InP that are grown on a GaAs substrate, the demonstrated fundamental

wavelengths of OPSLs range from 674 nm to 1300 nm [5]. The InP-based OPSLs based on InGaAsP or AlGaInAs can generate light at 1.5 μm that is suitable for optical communication [54], [65]. GaSb-based systems with alloys such as GaInSb, AlAsSb, GaInAsSb and others emit wavelengths around 2 to 2.3 μm [66]–[68]. The Sb-based heterostructure can also be grown on a GaAs substrate using interfacial misfit (IMF) dislocation arrays to compensate the lattice mismatch [69], [70]. In the mid-infrared region, the emission wavelength of 5 μm has been demonstrated with narrow bandgap IV-VI materials (PbTe/PbEuTe) [6].

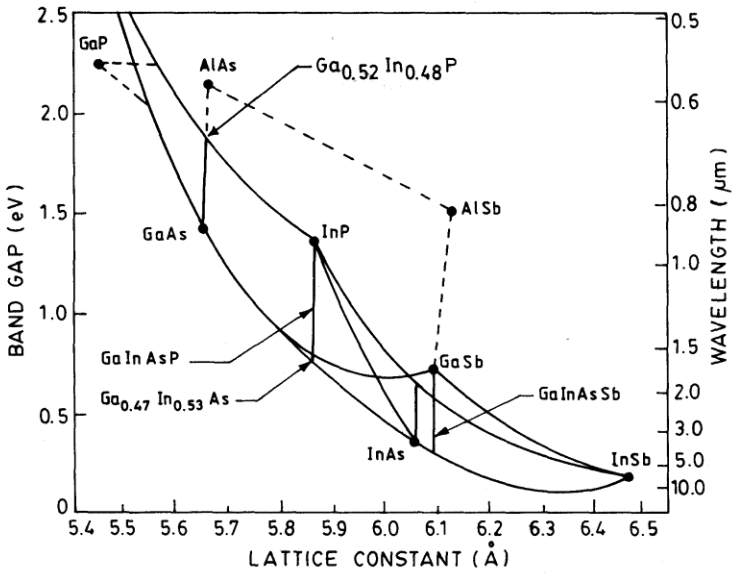

Figure 2.4 Bandgap energy vs. lattice constant for III-V compound semiconductors [71]

In addition to the selection of material, the accessible wavelengths of OPSLs are extended to even broader ranges through nonlinear optical conversion. Using nonlinear optical crystals, the light is converted to various harmonic frequencies, and also by the sum or the difference frequency generation to produce yet other frequencies. The most common nonlinear optical conversion is second harmonic generation (SHG). Various light sources from the ultraviolet (UV) to the visible region [35], [72]–[74] have been developed by intracavity SHG of the near infrared OPSL. Blue light of 488 nm is generated from intracavity frequency-doubling of a 976 nm laser as a replacement of Argon ion lasers for some applications [75]. Deep UV light at 244 nm is further generated through another SHG of the 488 nm OPSL with an external resonator [8]. On the other hand, a long-wavelength light source can be realized by difference frequency generation (DFG). A continuous wave terahertz source has been demonstrated by DFG in a dual wavelength OPSL [36].

Compared to conventional solid-state lasers, OPSLs are suitable for intracavity nonlinear optical conversion because of the absence of the “green problem” [76], [77]. The “green problem” or the “green noise” is the intensity noise that arises from frequency doubling in a multimode diode-pumped solid-state (DPSS) laser [78]. When a nonlinear crystal is inserted in the laser cavity for second harmonic generation, different longitudinal modes affect each other through sum frequency generation between different longitudinal modes. Each mode acts as a loss to other modes through the sum-frequency mixing process,

so the loss of one mode depends on the other modes. Moreover, cross-saturation of the gain affects the gain for the other modes with the changing intensity of a mode, and thus the output intensity of each longitudinal mode exhibits rapid fluctuation. In a DPSS, the upper state life time is around μs (Ti:Sapphire lasers) to ms (Yb-doped lasers), whereas the upper state lifetime (i.e. carrier lifetime) of OPSLs is in the regime of ns. As a result, the cross-saturation effect mentioned by Baer [37] is less significant, so that OPSLs do not suffer from the “green problem”.

2.2 Device characterization

OPSL devices are characterized by temperature dependent reflectivity (TDR) spectra and surface photoluminescence (PL) measurements. These non-destructive analyses are useful for diagnosing OPSL devices before they are used for laser operation. The TDR is the device reflectivity that is measured close to the surface normal at different temperatures. TDR spectra can tell us how well an OPSL is designed, or whether the wafer growth follows to the intended design. The absorption center of the quantum well and the refractive index of semiconductor materials are temperature dependent. As shown in Figure 2.5 and Figure 2.6, when the temperature increases, the band gap of the quantum wells shrinks causing the absorption/emission spectrum to redshift, and the microcavity resonant peak also shifts to longer wavelengths as well (but with a lower shift

rate) due to the change of the optical thickness, mostly due to the refractive index change rather than the thermal expansion of the material. The dips in the TDR spectra show the quantum well absorption enhanced by the microcavity resonance at the specific temperature. The deepest dip occurs at the temperature that the absorption and the microcavity resonance align spectrally. Figure 2.5 shows the TDR spectra of the device used in this study prior to coating. At first, the reflectivity dips become deeper and move toward longer wavelengths when the temperature gets higher. At 90^{o}C, the reflectivity dip reaches the lowest point around 65% and then becomes shallower at higher temperature. The shift rate of the reflectivity dip is ~0.1 nm/K dominated by the microcavity resonant effect. Figure 2.6 plots the TDR spectra of the same device with an anti-reflective (AR) layer for better wavelength tunability. Because of the AR coating, the microcavity resonant effect is reduced. Therefore, even though the dips are getting deeper at higher temperature, the dips are wider and shallower compared to a typical uncoated OPSL chip. The DBR stop band covers the range from 970 nm to 1070 nm. The TDR dips are from 996 nm at 30^{o}C to 1025 nm at 110^{o}C with a shift rate of ~0.37 nm/K.

The TDR is measured under low degree of carrier excitation, so this absorption spectrum is different from the gain spectrum of the laser when the carrier density is much higher at a given temperature. Moreover, we cannot predict the laser performance of a wafer from TDR spectra directly. TDR reveals the spectral characteristics of OPSL structures, but other factors such as the

strength of the optical gain in quantum wells and the scattering loss, need to be taken into account as well.

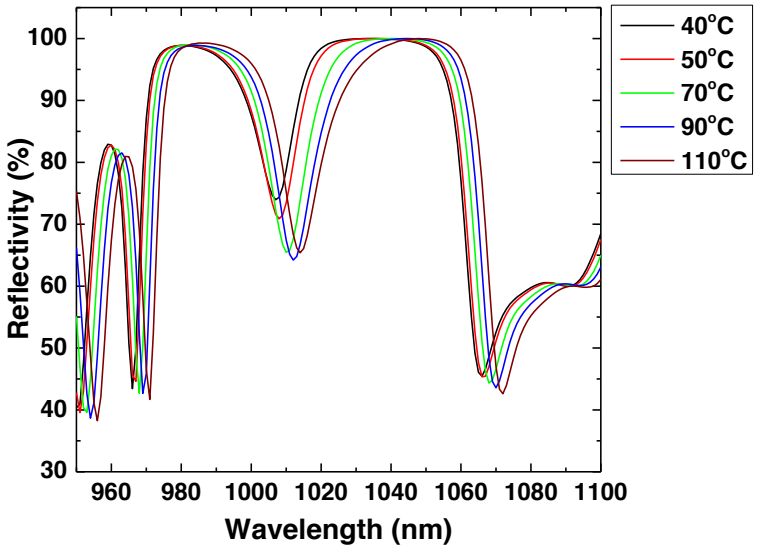

Figure 2.5 Temperature dependent reflectivity (TDR) spectrum of an uncoated device

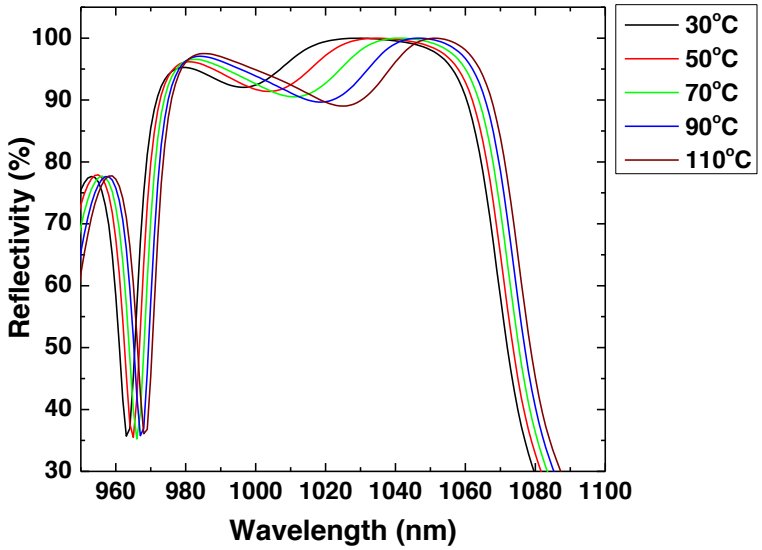

Figure 2.6 TDR spectrum of the AR-coated device

Surface PL is collected perpendicularly to the surface of an OPSL device with a spectral analyzer under low optical excitation. The QW emission spectrum is modulated by the interference within the dielectric layers, which is called the filter function. Theoretically, the surface PL can be estimated by the quantum well emission spectrum multiplying the direction- and dielectric-structure dependent filter function [79]. The quantum well emission spectrum is calculated by microscopic modeling based on semiconductor Bloch equations [80]–[82]. By comparing the spectral behavior between the theory and experimental results, the laser structure can be refined in several iterations of growth.

The surface PL spectra of the AR-coated device at different temperature are plotted in Figure 2.7. The spectral peaks shift from 997 nm to 1023 nm at temperature from 10^{o}C to 110^{o}C. The peak around 970 nm corresponds to a side-lobe of the DBR spectrum, as also shown in the TDR measurement in Figure 2.6. The shift rate of the surface PL peak is 0.25 nm/K. With AR-coating, the microcavity effect is weakened. We find a similar shift rate of 0.23 nm/K when the device is used for laser operation. Figure 2.8 shows the surface PL recorded at different pump powers at a given coolant temperature of 15^{o}C. With raising pump power, the carrier density increases, strengthening the PL amplitude, and the spectral width is widened by band-filling. When the pump power is further increased, the spectra shift to longer wavelengths due to the thermal and many-body Coulomb effect [2], [83]. The intrinsic gain spectrum of the quantum well

can be obtained by edge photoluminescence which is acquired from the edge of the sample to avoid modulation from the multilayer interference.

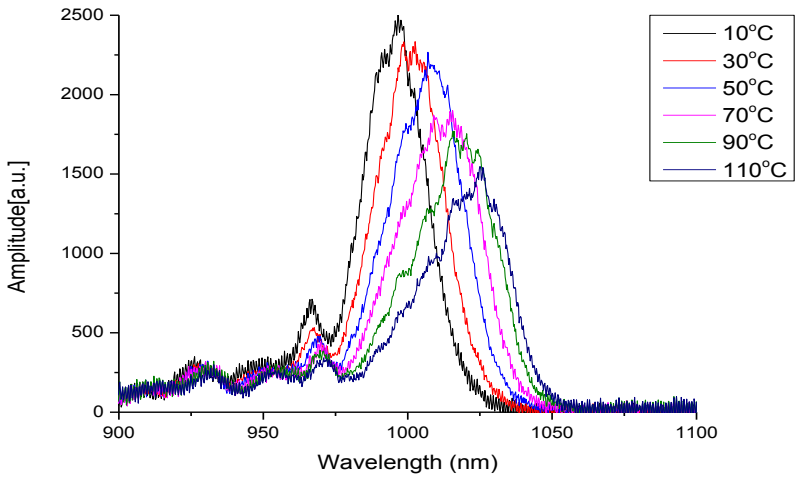

Figure 2.7 Temperature dependent surface photoluminescence (PL) spectrum with 200 mW of pump power

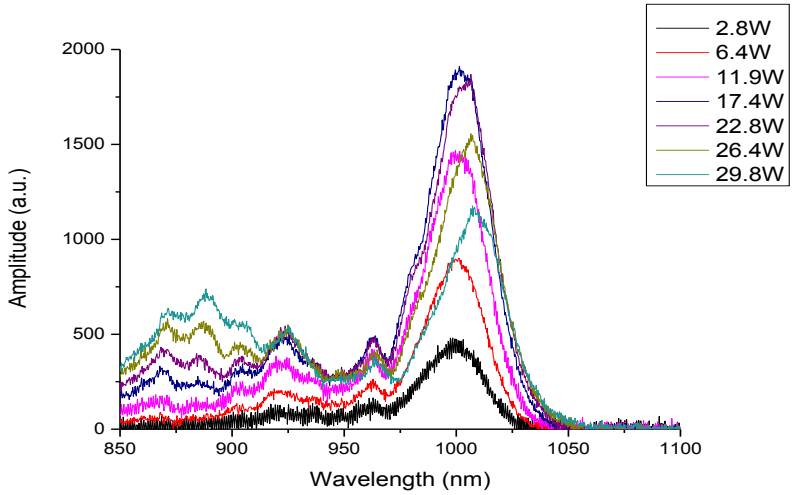

Figure 2.8 Surface photoluminescence (PL) spectrum using different pump power at 15°C

2.3 Principle of injection-locking

2.3.1 Injection-locking of laser oscillators

The concept of the Injection-locking system can be traced back to the 17th Century. A Dutch Physicist, Christiaan Huygens, observed that the pendulums of two clocks spontaneously synchronized when the clocks were hung close to each other [84]. Since then, theories related to injection-locked oscillators were developed in different studies by Adler [85], Kurorawa [86] and others [87]–[89]. Siegman provided a comprehensive introduction of laser injection locking in a chapter of his book “Lasers” [90]. In addition, some basic principles are described in [91].

Suppose a weak monochromatic signal with frequency ω_1 and output power I_1 is injected into a self-sustained laser oscillator with a free-running frequency of ω_0 and output power I_0. The laser oscillator provides gain to the signal at ω_1 even with a strong oscillation at ω_0. In the beginning, the laser oscillator acts like a regenerative amplifier for the signal at ω_1 since it is too weak to reach the threshold. The regenerative gain inside the cavity can be written as [90]:

$$g(\omega) = \frac{1-R}{1-G_{rt}(\omega)} \tag{2.1}$$

where R is the reflectivity of the input/output coupler. $G_{rt}(\omega)$ is the complex round-trip gain.

$$\begin{aligned} G_{rt}(\omega) &= r_m(\omega) \times \exp\left[-i(\omega_1 - \omega_0)L/c\right] \\ &= r_m(\omega) \times \left\{\cos\left[(\omega_1 - \omega_0)L/c\right] - i\sin\left[(\omega_1 - \omega_0)L/c\right]\right\} \end{aligned} \tag{2.2}$$

where r_m represents the magnitude of the round-trip gain including the intracavity gain, loss inside the laser cavity and the reflectivity of mirrors other than the output coupler. c is the speed of light and L is the total cavity length. In the steady state, the regenerative gain is clamped at the loss. Thus, the magnitude of $G_{rt}(\omega)$ must be equal to 1. Assuming $\omega_1 \sim \omega_0$, the round-trip gain can be approximated by

$$G_{rt}(\omega) \approx 1 - i\left[(\omega_1 - \omega_0)L/c\right] \tag{2.3}$$

By substituting equation (2.3) into (2.1), the power amplification is:

$$\left|g(\omega)\right|^2 \approx \frac{\gamma_e^2}{(\omega_1 - \omega_0)^2} \tag{2.4}$$

where $\gamma_e = (1-R)c/L$ is the cold-cavity decay rate. The signal at ω_1 is amplified when the frequency is tuned close to ω_0. When the amplified intensity $\left|g(\omega)\right|^2 I_1$ starts to compete with the free-running intensity I_0, the oscillating frequency at ω_0 is suppressed and eventually switched to ω_1. We can define the frequency range by applying $\left|g(\omega)\right|^2 I_1 = I_0$ in equation (2.4), and therefore

$$\Delta\omega = 2\gamma_e\sqrt{\frac{I_1}{I_0}} \tag{2.5}$$

2.3.2 Error signal generation

The injection-locked laser system is accomplished by providing a feedback mechanism to the slave laser so that the resonant frequency of the slave laser resonator is sufficiently close to the injected frequency. For the purpose of feedback, one needs to provide an error signal. One method of doing this is so-called the Pound-Drever-Hall (PDH) technique. The Pound-Drever-Hall (PDH) technique is widely used in frequency-stabilized lasers. The general idea is to stabilize the frequency of a laser by locking to the reference Fabry-Perot cavity. An error signal is fed back to the laser cavity through a servo loop. This is a useful technique to detect and suppress the frequency fluctuation between two laser cavities. In our laser system, we use a similar strategy to generate error signal. For laser frequency stabilization, a piezo-transducer (PZT) is attached to one mirror of the laser cavity that needs to be stabilized, but for our injection-locked system, the PZT is attached to a mirror of the slave laser cavity. The frequency of the slave laser is tuned by the PZT in that the longitudinal mode of the slave laser is varied by the cavity length. The spacing between each longitudinal mode is called the free spectral range, which is defined as:

$$\Delta\upsilon_{FSR} = \frac{c}{L} \tag{2.6}$$

where c is the speed of light and L is the total cavity length of the ring cavity. L will be substituted to 2L if it is a stand-wave resonator. The details of the system design will be discussed in the next chapter. The derivation of the error signal

generation is shown as follows. The sign convention is used according to ref. [92].

Assume there is an incident beam from the master laser, where the electric field with amplitude E_0 and angular frequency ω is written as:

$$E_{inc} = E_0 e^{i\omega t} \tag{2.7}$$

After passing through a phase modulator, an electro-optic modulator (EOM), the phase of the electric field is modulated. Assuming that the modulation depth β is fairly small, the incident field can be approximated by Bessel functions:

$$E_{inc} = E_0 e^{i(\omega t + \beta \sin \Omega t)} \simeq E_0 \left[J_0(\beta) e^{i\omega t} + J_1(\beta) e^{i(\omega+\Omega)t} - J_1(\beta) e^{i(\omega-\Omega)t} \right] \tag{2.8}$$

where Ω is the modulation frequency and β is the modulation depth. The beam reflected by the output coupler of the slave laser is given by:

$$E_{ref} = E_0 \left[F(\omega) J_0(\beta) e^{i\omega t} + F(\omega+\Omega) J_1(\beta) e^{i(\omega+\Omega)t} - F(\omega-\Omega) J_1(\beta) e^{i(\omega-\Omega)t} \right] \tag{2.9}$$

where the reflection coefficient $F(\omega)$ is the ratio between the reflected and the incident beam. For a passive cavity with no gain, $F(\omega)$ can be deduced from summing up the complex amplitude of a Fabry-Perot interferometer [93] and can be expressed as:

$$F(\omega)=\frac{E_{ref}}{E_{inc}}=\frac{r\left[\exp\left(i\frac{\omega}{\Delta\upsilon_{FSR}}\right)-1\right]}{1-r^2\exp\left(i\frac{\omega}{\Delta\upsilon_{FSR}}\right)} \tag{2.10}$$

where r is the reflection coefficient of the output coupler. $\Delta\upsilon_{FSR}$ is the free spectral range of the slave laser cavity. When the pump of the injection-locked laser turns on, the optical gain from the gain medium is added to the circulating electric field. As shown in Figure 2.9, an electric field E_{inc} is injected into a ring cavity through an input/output coupler with reflection coefficient r and transmission coefficient t. Assume the coupler is non-absorptive, energy conservation leads to $r^2+t^2=1$. r_m is equal to one minus the intracavity loss, which is a ratio of the remaining E-field amplitude after a single round trip in a passive cavity. g is the round trip gain of the gain medium

.

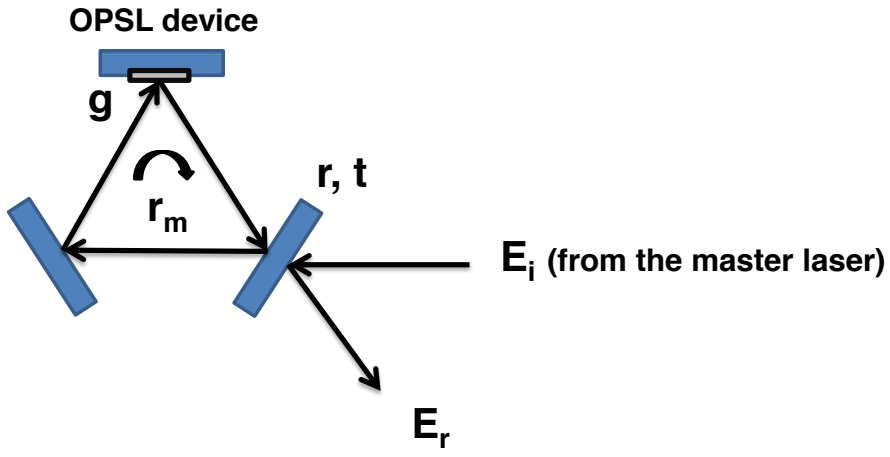

Figure 2.9 The incident, reflected and circulating electric field in a ring cavity

Assuming the laser light is emitted after q times of round trips, the reflected electric field $E_{ref}(q)$ can written as:

1: $E_{ref}(1) = rE_{inc}$

2: $E_{ref}(2) = (it)^2 r_m g e^{j\phi} E_{inc}$

3: $E_{ref}(3) = (it)^2 r r_m^2 g^2 e^{j2\phi} E_{inc}$

….

q: $E_{ref}(q) = (it)^2 r^{q-2} r_m^{q-1} g^{q-1} e^{j(q-1)\phi} E_{inc}$

The total reflected electric field is the sum of round trips:

$$\begin{aligned} E_{ref} &= rE_{inc} + (it)^2 \sum_{q=2}^{\infty} \left(r^{q-2} r_m^{q-1} g^{q-1} e^{j(q-1)\phi} \right) E_{inc} \\ &= rE_{inc} + (it)^2 r_m g e^{j\phi} \sum_{q=2}^{\infty} \left(r r_m g e^{j\phi} \right)^{q-2} E_{inc} \\ &= rE_{inc} - \frac{\left(1 - r^2\right) r_m g e^{j\phi}}{1 - r r_m g e^{j\phi}} E_{inc} \\ &= \frac{r - r_m g e^{j\phi}}{1 - r r_m g e^{j\phi}} E_{inc} \end{aligned}$$

Where the Identity is applied:

$$\sum_{q=0}^{\infty} r^q = \frac{1}{1-r} \quad \text{if } |r| < 1,$$

So, the reflection coefficient equals:

$$F(\omega) = \frac{E_r}{E_i} = \frac{r - r_m g e^{j\phi}}{1 - r r_m g e^{j\phi}} \tag{2.11}$$

When there is no gain (g = 1) and the impedance match condition is fulfilled ($r = r_m$), the equation of $F(\omega)$ becomes the same as the condition of a Fabry-Perot interferometer in equation (2.10).

The power of the reflected beam received by the photodetector is proportional to the square magnitude of the electric field, $P_{ref} = |E_{ref}|^2$. Substituting E_{ref} with the equation (2.9), P_{ref} can be expanded as:

$$\begin{aligned} P_{ref} = {} & P_c |F(\omega)|^2 + P_s \left[|F(\omega+\Omega)|^2 + |F(\omega-\Omega)|^2 \right] \\ & + 2\sqrt{P_c P_s} \left\{ \mathrm{Re}\left[F(\omega) F^*(\omega+\Omega) - F^*(\omega) F(\omega-\Omega) \right] \cos\Omega t \right. \\ & \left. + \mathrm{Im}\left[F(\omega) F^*(\omega+\Omega) - F^*(\omega) F(\omega-\Omega) \right] \sin\Omega t \right\} \\ & + (2\Omega \text{ terms}) \end{aligned} \tag{2.12}$$

The Ω terms come from the interference between the carrier and the sidebands, and the 2Ω terms are from the beat note between the two sidebands on both sides of the carrier. When the frequency of the two lasers are close to each other, and the modulation frequency Ω is high enough, the sidebands are mostly reflected, $F(\omega \pm \Omega) \approx -1$. The cosine term becomes zero and only the sine term remains. By mixing the signal from detector with the local oscillator signal, the error signal is demodulated to DC from the sine term:

$$\varepsilon = -2\sqrt{P_c P_s}\,\mathrm{Im}\left\{F(\omega)F^*(\omega+\Omega) - F^*(\omega)F(\omega-\Omega)\right\} \tag{2.13}$$

The information of the frequency offset is therefore extracted from the reflected light signal. Figure 2.10 illustrates an example of the error signal amplitude. Note that the error signal is anti-symmetric across the resonance. When the frequency error is detected, the servo adjusts the cavity length of the slave laser to the opposite direction, locking the frequency of slave laser to that of the master. In a closed feedback loop, the system is operated in the linear region at the center frequency with a steep slope.

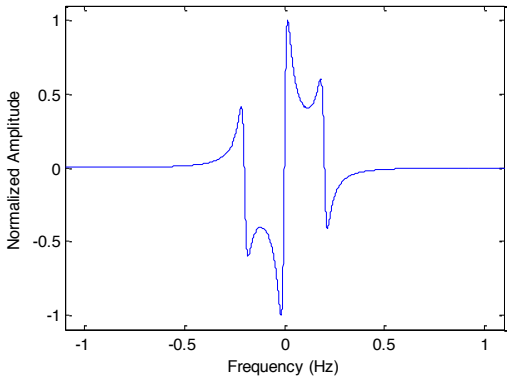

Figure 2.10 Pound-Drever-Hall Error signal

2.4 Comparison to prior art: Injection-locking applications

The goal of this study is to realize a single frequency laser with stable output that generates several watts of power at a specific wavelength (for example, 1014.9 nm as performed in this work) based on the injection-locking technique. An injection-locked laser system consists of two parts: a master laser and a slave laser. The master laser is a relatively low power but narrow linewidth laser. The frequency of the master laser can be independently stabilized to an external reference such as a high finesse Fabry-Perot cavity. In some cases, wavelength flexibility is necessary to tune the master laser to the required wavelength for specific application. The slave laser functions as an amplifier whose free-running wavelength is close to the master laser. Injection-locking has previously been demonstrated on various laser systems, including argon ion [94], dye [95], diode [96]–[98], Nd:YAG [99]–[101] and Ti:Sapphire [91], [102]–[104] lasers to achieve high output power while maintaining single frequency operation. In this section, we will discuss how injection-locking technique is applied in different types of lasers and why the OPSL is the best choice of our application by comparing with other lasers.

Diode lasers are well-developed in industries and have been massively produced over many years [21]. In what is conventionally called “edge emitters”, the laser cavity is simply formed by the two facets of the semiconductor material. They typically operate multiple longitudinal modes. By injecting single-mode laser

light into a diode laser array or broad-area lasers (BALs), the spectral characteristics and the far-field pattern can be controlled by adjusting the injection beam relative to the array position and the frequency of the master laser [96]. Single lobe emission was achieved for output power up to 1 W by injecting 12 mW of the master laser at 830 nm into a broad stripe laser diode [98]. The output beams of edge emitters are highly asymmetric and astigmatic due to the asymmetric confinement structure, so that extra optical elements are required to correct the beams. This is done by anamorphic prism pairs or coupling beam into fibers. A significant part of output power of the laser is wasted after fiber coupling, degrading the overall power efficiency.

Nd:YAG lasers are one of the most widely used solid state lasers for numerous applications. A number of demonstrations have been done with Nd:YAG lasers using the injection-locking technique. A lamp-pumped, 13 W Nd:YAG ring laser was injection-locked using a 40 mW single-frequency, diode-pumped, monolithic, nonplanar ring oscillator (NPRO) as the master laser in 1989 [99]. By combining two laser modules (four Nd:YAG rods in total), 101 W of output power was produced using 2 W of injection power from a master laser in 2005 [101]. Although Nd:YAG lasers can provide high output power, the emission wavelengths of Nd:YAG laser are mostly limited to the transitions at 1064 nm with narrow gain bandwidth of 0.6 nm. There are also other transitions near 946 nm, 1319 nm, 1339 nm and etc. [105], but the wavelength selections are still limited and not necessarily available for specific spectroscopic applications.

Titanium-doped sapphire (Ti:sapphire or Ti:Al_2O_3) lasers have a large gain bandwidth. The emission spectrum covers from 650 nm – 1100 nm making Ti:Sapphire lasers suitable for a tunable light source and ultra-short pulse generation. Cummings et al. demonstrated a 1 W injection-locked CW Ti:Sapphire laser at 846 nm using 15 mW of injection power from an external cavity diode laser [91] in 2002. The injection-locked output power was further improved to 5 W at 846 nm with 70 mW of injection power in 2008. 1.1 W was generated by frequency-doubling to 378 nm [102]. Chiow et al. confirmed that 6 W of combined power from the master and slave lasers at 850 nm with up to 800 mW from the Ti:sapphire master laser [103]. Even with such a wide gain bandwidth, the Ti:sapphire laser may not be suitable for our application since the gain is significantly lower for wavelengths above 1000 nm compared to those at previously demonstrated wavelengths. Another drawback of the Ti:sapphire laser is the limitation of pump sources. Although the Ti:sapphire laser has wide range of absorption from 400 nm to 600 nm, the absorption peak around 500 nm is not reachable by powerful laser diodes. In the early days, Argon-ion lasers at 514 nm mainly served as the pump source. Recently, frequency-doubled Nd:YAG or Nd:YVO_4 lasers at 532 nm have become available and are now widely used. Those pump sources are relatively expensive compared to a diode pump system.

The lasers mentioned above have some good characteristics that are suitable for different applications. However, none of them possess all the requirements to provide sufficient power at an unconventional wavelength (e.g.

1014.9 nm). On the other hand, the wavelength of OPSLs can continuously be tuned around 1 μm using the InGaAs/GaAs system as discussed in above sections, which is the essential element of the master laser. As for the slave laser, OPSLs have been demonstrated generating at least 23 watts in single frequency [13], providing sufficient optical gain for the laser system as well as maintaining the beam quality. Combining the required factors, with suitable wavelength coverage, wavelength tunability, high output power and good beam quality, the OPSL is one of the best choices for this application. Table 2.1 compares some of the important parameters that affect the operation of the injection-locked laser system.

Table 2.1 Laser material comparison

	Nd:YAG	Ti:Sapphire	OPSL
beam quality	good	good	good
absorption wavelengths	808 nm	400 nm ~ 600 nm	flexible (> bandgap energy)
emission wavelengths	946 nm, 1064 nm, 1319 nm, 1339 nm, and etc.	660 nm ~ 1180 nm	390 nm ~ 5 μm
wavelength tunability	Narrow (0.6nm@1064 nm)	wide (450nm)	~20 nm
upper state lifetime	230 μs	3.2 μs	ns

CHAPTER 3 SYSTEM DESIGN

The objective of this study is the investigation of stable, single-frequency lasers that produce high output power at a tailored wavelength. The laser system is realized by injection-locking an optically-pumped semiconductor laser (OPSL), taking advantage of its flexibility of its operating wavelength. Figure 3.1 illustrates the configuration of the laser system.

The injection-locked laser system consists of a master laser and a slave laser. The main function of the master laser is to provide a stable, single frequency laser output with wavelength tunability. The slave laser plays the role of amplifying the laser power while maintaining the frequency stability of the master laser. The laser devices used in our system are both from the same InGaAs-based OPSL wafer. The wafer was grown in reverse order; the active region is grown first on the GaAs substrate followed by the distributed Bragg reflector (DBR). Each of the OPSL chip is bonded with the epitaxial side down to a 500-μm thick CVD diamond heat spreader with thermal conductivity of 2000 W/K·m, and then the substrate is removed by a chemical wet-etching process. The device is antireflection (AR)-coated for 1015 nm with λ/4-thick hafnium oxide (HfO_2, n ~ 1.97). The finished OPSL device is mounted on a water-cooled copper heat sink. A 50-μm thick indium foil is sandwiched in between for better thermal contact

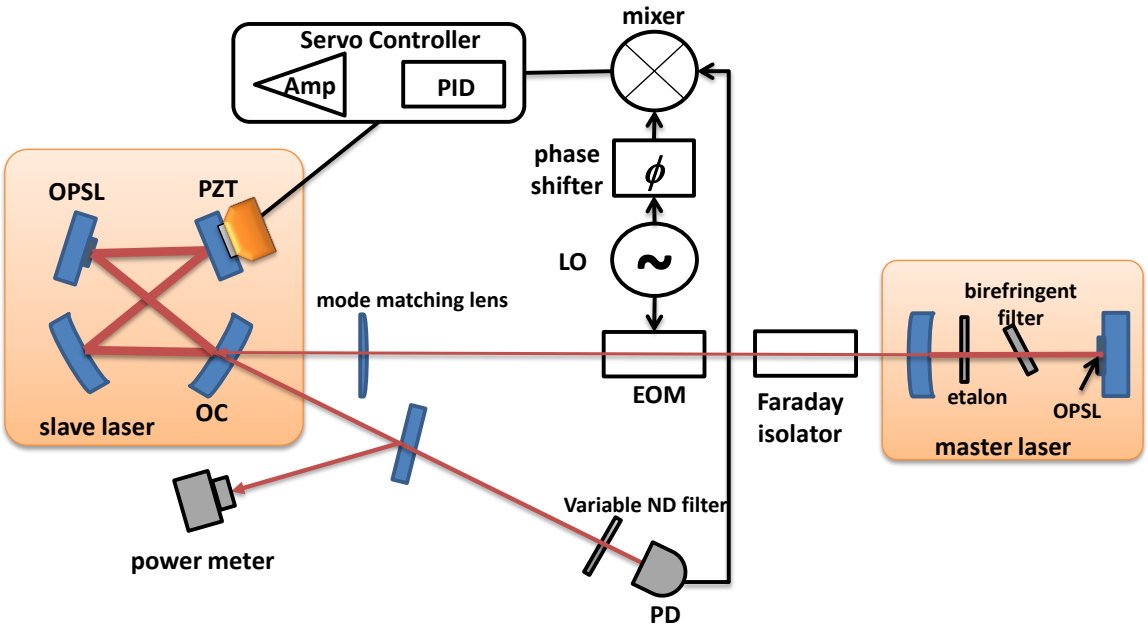

Figure 3.1 Schematic of injection-locked OPSL. LO: local oscillator, EOM: electro-optic modulator, PD: photodiode, OC: output coupler

The master laser is a linear-cavity OPSL providing a maximum power of 1.5 W at 1015 nm. The single frequency operation is enforced by a birefringent filter and an etalon. The emission wavelength of the master laser can be tuned from 1008 nm to 1022 nm. The injection-locking is maintained using the so-called Pound-Drever-Hall technique [92], [106]. The injecting beam from the master laser passes through a Faraday isolator to avoid optical feedback. A 20 MHz RF signal from the local oscillator is fed into the electro-optic phase modulator (EOM). The signal modulates the phase of the master laser to generate sidebands. The injecting beam is mode-matched to the slave laser. The slave

laser operates in single transverse mode with M^2 = 1.08 along the horizontal axis and M^2 = 1.04 along the vertical axis (Figure 3.2). The optical length of the slave laser cavity is controlled by a piezoelectric transducer (PZT) that is attached on one mirror of the laser. The slave laser is a ring-cavity OPSL so that the optical feedback into the master laser can be minimized. A small portion of the output beam from the slave laser is separated and incident on a high-speed photodetector. The signal received by the photodetector contains information of frequency detuning between two lasers and is then mixed with the RF signal from the local oscillator to generate the error signal. The low-frequency component of the error signal is extracted and amplified by a servo controller and is fed back to the PZT to maintain locking. The details of the cavity designs, electronic circuits and their output performance are discussed in the following section.

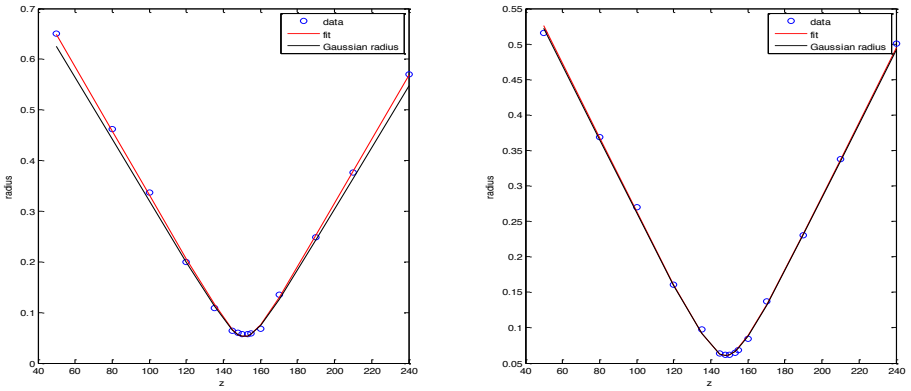

$M_x^2 = 1.075$ $M_y^2 = 1.042$

Figure 3.2 M^2 measurement of the free-running slave laser

3.1 Laser Cavity Design and Performance

3.1.1 The master laser

The 60-mm long linear cavity of the master laser is formed by the DBR of the OPSL chip and the output coupler with 200mm radius of curvature which results in a fundamental mode size that is 344 μm in diameter. The pump is imaged onto the OPSL chip and overlaps with the cavity mode. For single transverse mode operation, the pump spot diameter is about the same size as the cavity mode in this case.

The master laser provides up to 1.5 W of output power at 1015nm in a single frequency, enforced by a birefringent filter and an etalon. The birefringent filter is a 3-mm thick uncoated quartz plate (n_o ~ 1.535, n_e ~ 1.546) inserted in the master laser at the Brewster's angle of 57^o to minimize the cavity loss and polarize the laser. By rotating the optical axis of the birefringent filter [107], [108], the emission wavelength of the master laser can be tuned from 1008 nm to 1022 nm, with somewhat lower output power toward the ends of the tuning range. An uncoated fused silica etalon is inserted in order to ensure single frequency operation.

The mounts of the birefringent filter and the etalon are attached to thermoelectric modules, so that the temperature can be accurately controlled for the operation at the desired wavelength. The transmission spectra of the mode

selection elements can be fine-tuned by varying the temperature with a rate of -0.12 nm/K for the birefringent filter and +7 pm/K for the etalon.

3.1.2 The slave laser

The slave laser is a four-mirrored bow-tie resonator that consists of two flat mirrors, one from the DBR structure of the OPSL and one from the HR mirror bonded to the PZT actuator, and two curved mirrors, whose radii of curvature are 100 mm. In order to maximize the output power at the available pump brightness, the output power of an OPSL is scaled by enlarging the pump size at the gain chip. The pump size is scaled by the combination of the collimating lens and the imaging lens with different focal lengths. The magnification of the pump spot is the ratio between the focal lengths of the two lenses. Meanwhile, the pump-to-mode ratio is fixed when power-scaling in order to maintain single-transverse mode operation. With the larger pump spot size and the larger mode size, the laser threshold is higher, but the thermal rollover is reached at a higher pump power, and therefore higher output power can be obtained.

The cavity transverse mode is calculated by ABCD matrix analysis for a Gaussian beam [109]. The cavity configuration is schematically shown in Figure 3.3, and the parameters are listed in Table 3.1. The total cavity length is 438 mm and the angle of incidence is 10^{o}. Due to the geometry of the ring cavity, the beam size is asymmetric with the sagittal (vertical) radius 1.1 times of that of the

tangential (horizontal) radius at the OPSL. The calculated mode radii (Figure 3.4) are 242 μm in the tangential plane and 266 μm in the sagittal plane at the OPSL device. The waist of the cavity mode with radii of 56 μm (same size at the waist for tangential and saggital direction) is located between the two curved mirrors. For mode-matching to be fulfilled, we can manipulate the beam waist of the incoming beam to match the size and the location to that of the slave laser beam.

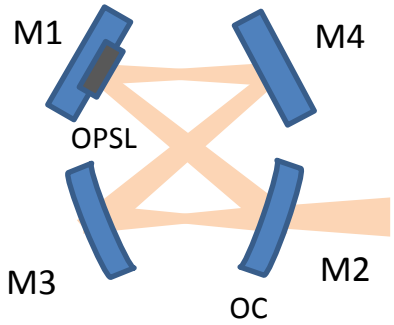

Figure 3.3 Slave laser cavity configuration

Table 3.1 The parameters of slave laser configuration

Surface	ROC (mm)	Distance (mm)
M1	∞	114
M2	100	112
M3	100	112
M4	∞	100

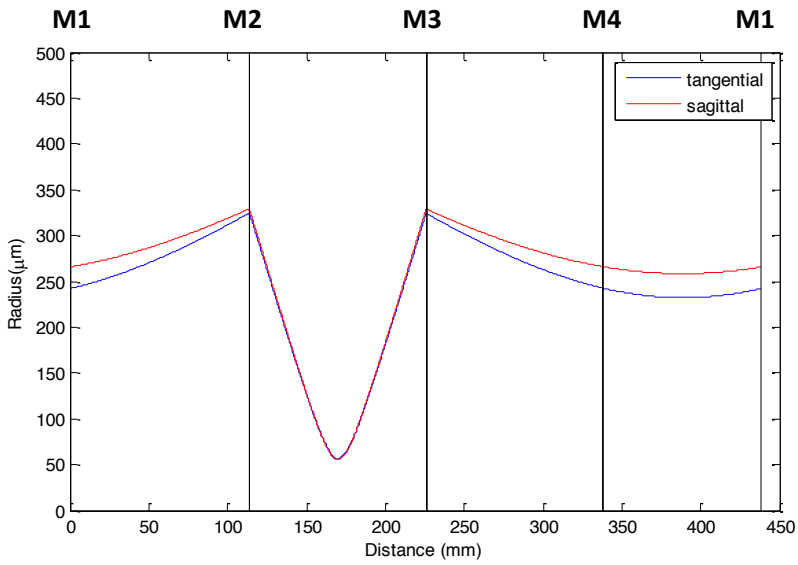

Figure 3.4 Cavity mode calculation of the slave laser cavity

The pump source is a fiber-coupled diode pump providing up to 34 W of power with a fiber diameter of 105 μm (DILAS, M1F1S22-808.3-35C-SS2.1). With the numerical aperature (NA) of 0.22, the brightness is 2600 kW/sr/cm^2 at the rated output power. The focal lengths of the collimating lens and the imaging lens are 36.01 mm and 126.1 mm respectively, giving the magnification of 3.5. As shown in Figure 3.5, the beam profile is symmetric and has nearly the same width along the two orthogonal axes. The pump radius of the second-moment width at the focus is ~182 μm measured perpendicularly to the beam by a beam profiler. The transverse distribution of the pump is near a top-hat beam. For high power operation, a pump profile with top-hat transverse distribution is beneficial to

spread the excess heat, and the temperature rise is lower than a device pumped by a Gaussian beam [110].

Unlike the condition in Ref. [56], we found that if the pump size is the same or slightly larger than the mode size, higher order transverse modes start to oscillate at pump power above 20 W even though the laser emits only fundamental transverse mode at lower power. The pump to mode ratio of the slave laser is chosen to be 0.76. In this condition, the slave laser can remain in single transverse mode at the maximum available pump power. The pump beam is incident with an angle of 25^{o} within the vertical plane that is perpendicular to the plane of the bow-tie resonator so that the ratio between sagittal radius and the tangential radius is 1.1, which matches the cavity mode.

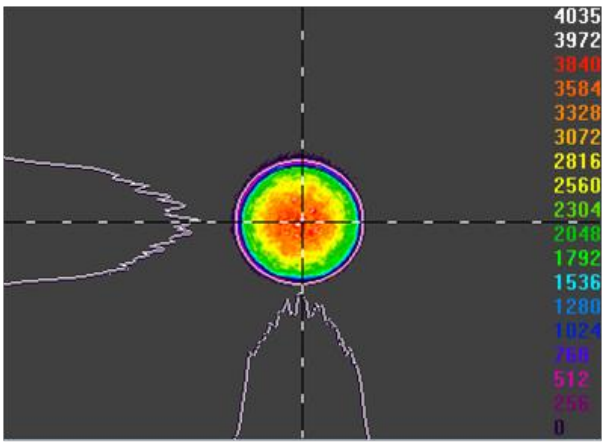

Figure 3.5 Pump profile at focus

Figure 3.6 shows the output power of the slave laser as a function of total pump power at water temperature of 15^{o}C. In order to determine the best output coupling for the slave laser, three different output couplers were used with the transmission of 1%, 3% and 4% respectively. The laser emits bidirectionally from the ring cavity, so the total output power is the sum of two outputs. With AR coating on the OPSL device, the measured pump reflectivity is 4%. The threshold power for T = 1% output coupler is 3.5 W, and the slope efficiency is 18%. Although the threshold power increases to 10.4 W when switching to the T = 3% output coupler, the slope efficiency is improved to 38%, giving higher output powers with pump powers above 25 W. The slave laser did not reach the lasing threshold with T = 4% output coupler, indicating relatively low optical gain of OPSL devices. In ref [111], the small signal gain of an AR-coated OPSL is estimated to be 4% ~ 5% based on the reflectivity measurement. For a laser to reach threshold, the unsaturated gain needs to exceed the overall loss including the output coupling loss and the passive loss inside the laser cavity.

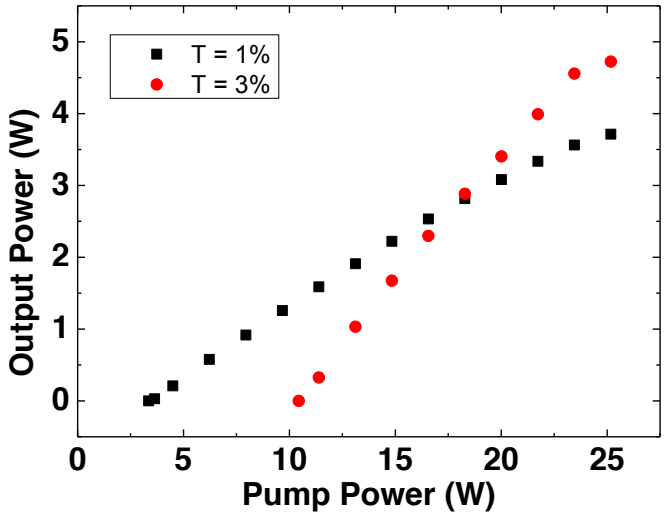

Figure 3.6 The experimental data of the free-running slave laser output with T = 1% and T = 3% output couplers

In ref [112], a 1-μm emitting device with similar design to our OPSL chip is used, but the device has no AR-coating. It is shown that the optimum output coupling is 5% for the uncoated device, whereas the T = 3% output coupler performs the best in our experiment. With a proper thickness of the structure, the effective gain of an uncoated device is enhanced by the microcavity resonance that is formed by the DBR and the semiconductor-air interface. With higher effective gain, the optimum output coupling for maximum output power becomes higher.

The emission wavelengths of the slave laser using the T = 1% and T= 3% output couplers are plotted in Figure 3.7. The emission wavelengths range from

1014 nm to 1020 nm. As the pump power increase, the emission wavelengths shift to the longer wavelengths by approximately 0.28 nm/W (with respect to the incident pump power). By changing the heatsink temperature from 5°C to 25°C, the emission wavelengths shift by ~0.23 nm/K. By combining these two results, the thermal impedance of the OPSL device is estimated to be 1.2 K/W with respect to the incident pump power. The thermal impedance with respect to the dissipated heat is determined to be 3.1 K/W, as it will be analyzed in the next chapter.

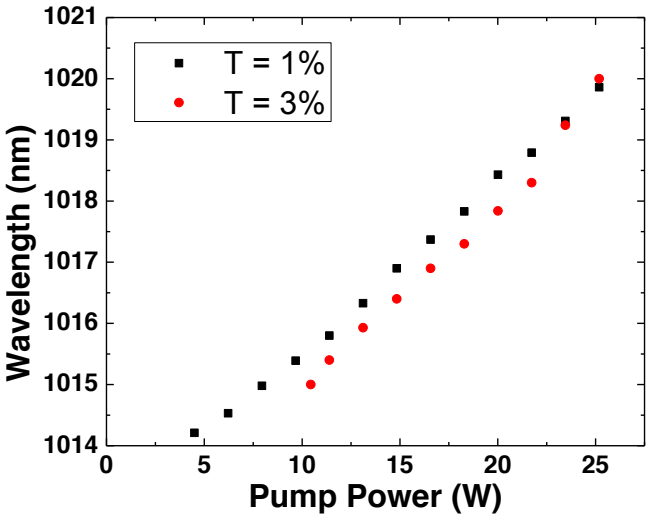

Figure 3.7 The emission wavelength of the free-running slave laser with T = 1% and T = 3% output couplers

3.2 Electronic circuits

In the injection-locked laser system, the slave laser cavity is locked to the master laser via the electronic feedback loop. The error signal is generated from the interference between the sidebands and carrier signal. To generate the sidebands (Figure 3.8), the 20 MHz RF signal from a local oscillator (POS-25+, Mini-Circuits) is amplified and split into two paths by a power splitter (MSC-2-1+, Mini-circuits). In one path, two phase shifters (JSPHS-26, Mini-Circuits) are inserted to compensate the unequal delay of the phase between the two paths. The two phase shifters are cascaded in order to tune the phase over 180^{o}. Along the other path, the signal is amplified to 36 V_{p-p} and fed into an EOM.

After the light from the master laser passes through the EOM, the modulated signal is mode-matched to the TEM_{00} mode of the slave laser. A portion of the reflected beam is collected by a silicon amplified photodetector (PDA10A, Thorlabs) with 150 MHz bandwidth, well beyond the bandwidth needed for error signal generation. A variable ND filter is placed in front of the photodiode to attenuate the signal so that the photodiode is not saturated. Also, the filter is adjusted for different output power in order to maintain the error signal at a constant magnitude.

For the discrimination of the frequency, the signal from the photodetector is demodulated by mixing with the phase-shifted signal from the local oscillator in a mixer (SBL-2LH+, Mini-Circuits). Thus, the error signal is generated and fed

into the servo controller (PID110, TOPTICA). Further analysis of operating the EOM and the servo controller are discussed as follows.

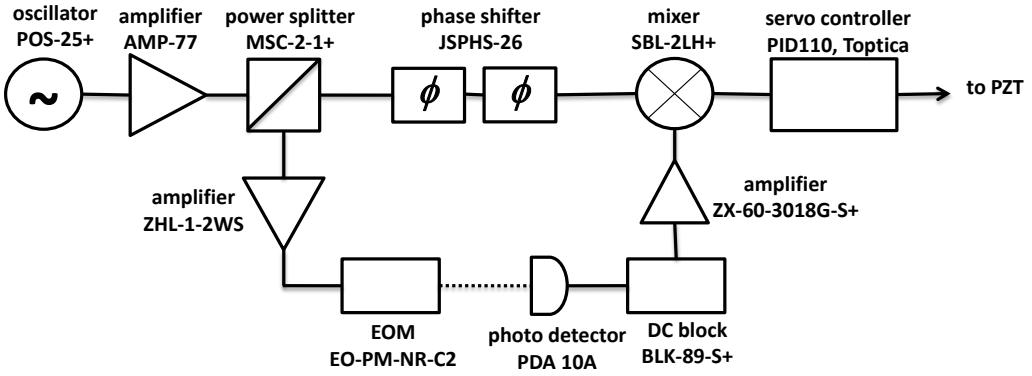

Figure 3.8 Servo loop block diagram

3.2.1 Electro-optic phase modulator (EOM)

When monochromatic light is incident into the EOM, the phase (or frequency) component of the electric field is modulated, which creates the sidebands. The introduction of the sidebands is to provide a reference to measure the frequency offset between the master laser and the slave laser. The amplitudes of the sidebands are controlled by the voltage applied across the EOM. The depth of modulation is described by the following:

$$\beta = \pi \frac{V_m}{V_\pi} \tag{3.1}$$

where

$$V_\pi = \frac{d}{L}\frac{\lambda_0}{n_e^3 r_{33} - n_0^3 r_{13}} \tag{3.2}$$

is the half-wave voltage, the voltage required to induce a phase change of π. V_m is the modulation voltage. n is the refractive index of modulator crystal. r_n denotes the electro-optic constant. The EOM used in the experiment is produced by Thorlabs (EO-PM-NR-C2). The modulator crystal is a MgO doped lithium niobate ($LiNbO_3$) with 2 mm diameter of clear aperture. The RF voltage is applied along the vertical direction (z-axis) of the crystal to induce a phase change of the extraordinary ray. Figure 3.9(a) illustrates the half wave voltage as a function of different incident wavelengths of the EOM. It shows $V_\pi \sim 230$ V for the wavelength at 1020 nm. As a consequence of varying the modulation voltage V_m, the modulation depth changes linearly. Thus, part of the power is transferred to the sidebands with a frequency shift of Ω. The relative sideband power with different phase shift is plotted in Figure 3.9(b). In the experiment, the modulation voltage is $\pm$18 V with corresponding phase shift of 0.25 rad. Therefore, the relative power of the carrier and the first-order sidebands are 97% and 1.5%. When the pump power of the injection-locked laser increases, the carrier and the sidebands experience different gain due to the gain saturation, which will cause the deformation of the error signal. Therefore, we only need a small portion of the power converting to the sideband to form the error signal in the experiment. More details will be discussed in section 4.8.

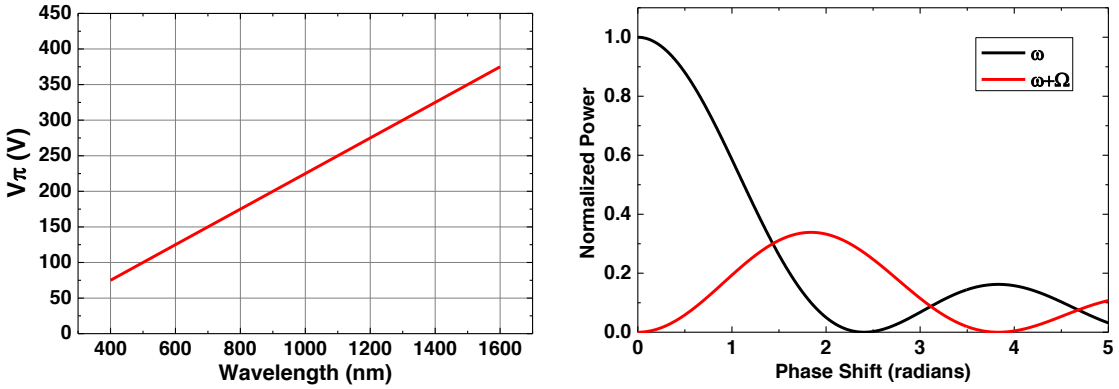

(a) (b)

Figure 3.9 (a) The half-wave voltage versus wavelength (b) Sideband power versus phase shift of the EOM from Thorlabs

3.2.2 PID controller

A PID controller receives the information of the frequency offset from the error signal and adjusts the output until the error is zero. If u(t) is the controller output and e is the error, a general form of the PID is written as:

$$u(t) = k_p e(t) + k_i \int_0^t e(\tau)d\tau + k_d \frac{de(t)}{dt} \tag{3.3}$$

The three terms above represent the proportional term, the integral term and the derivative term respectively. The proportional term depends on the present error, the integral term is the average of past errors and the derivative term predicts the

future error by means of linear extrapolation. The adjustable parameters are the proportional gain k_p, the integral gain k_i and the derivative gain k_d.

The Laplace transform of the PID controller is:

$$G(s) = K_p + \frac{K_i}{s} + K_d s = \frac{K_d s^2 + K_p s + K_i}{s} \tag{3.4}$$

The PID controller used in our experiment is manufactured by TOPTICA Photonics (PID110). After the signal is sent to the PID controller, firstly, the set point is adjusted at a reference point close to the center frequency of the master laser. The error signal as a function of the detuning can be observed on an oscilloscope by simply scanning the PZT. The cavity length of the slave laser is swept to verify whether the error signal is maintained in an adequate signal-to-noise ratio. As seen in Figure 3.10, the space between the sidebands and the carrier frequency at the center corresponds to the detuning of the modulation frequency (20 MHz). With this information, we can estimate the linear operating range of the system. In Figure 3.10(b), with the assumption that the PZT moves at the constant rate, the horizontal axis is linearly converted into a frequency unit. The linear operating range in frequency is approximately ± 280 kHz. The PID controller acts as a low-pass filter to suppress the high-frequency component of the laser noise. In practice, the derivative term D is more sensitive to high-frequency components in the input signals. In general, only “P” and “I” are used for laser stabilization. The total gain is increased to extend the frequency bandwidth to be wider than the noise spectrum of the laser. However, if the gain

is too high, the output of loop will oscillate at the frequency where the phase shift becomes 180^{o}. This will cause a positive feedback to the system making the laser signal unstable. Therefore, one needs to make sure that the unity gain is within the frequency range where the phase shift of the servo loop is 180^{o} [113]. As the pump power increases, the amplitude of the error signal increases accordingly. Therefore, we adjust the variable ND filter so that the amplitude of the error signal is around several hundred mV and the PID controller setting remains unchanged. At the final stage, the signal is amplified with an amplifier to provide sufficient DC voltage to drive the PZT actuator.

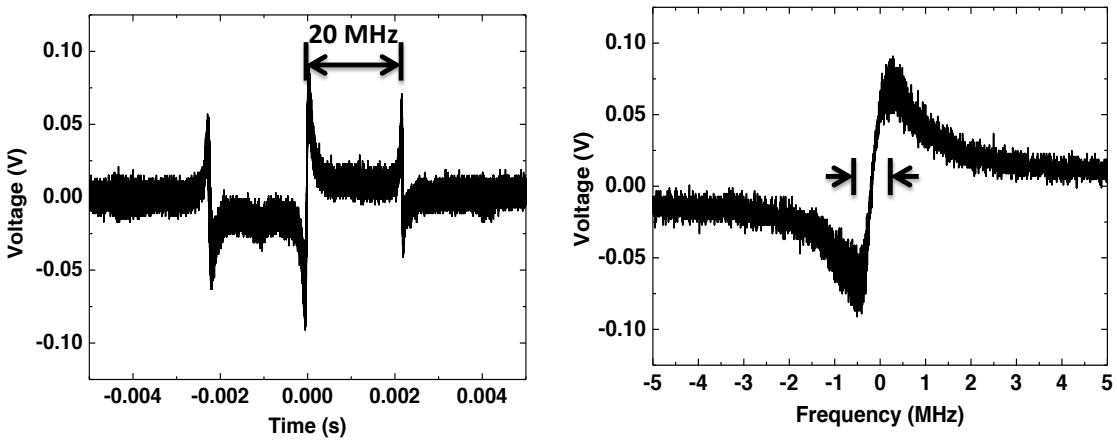

Figure 3.10 (a) The error signal in the unit of time (b) The error signal near resonance in the unit of frequency

3.3 Control of the mechanical resonance

3.3.1 Environmental stabilization

It is common that the injection-locked lasers or anything that involves locking the frequency of a resonator to another reference are subject to environmental noises such as acoustic, seismic, or any vibration of surrounding structure including the floor of the lab. In order to maintain the stable locking, any mechanical resonance of the laser system should be removed or suppressed. To reduce the environmental noise, the experimental setup must be carefully handled. The entire laser system is placed on an air-floated optical table in order to isolate from the vibration of the floor. The master laser is packaged in a robust aluminum shielding box with the optical components screwed tightly inside the box. The etalon and the birefringent filter in the master laser are attached on thermoelectric coolers (TEC) in order to stabilize the temperature and to reduce temperature fluctuations. Thus, the emission signal of the master laser can maintain single-frequency operation. The frequency of the master laser can be further stabilized by active stabilization to a reference cavity or spectroscopic reference, but is not applied in this study. The slave laser is set up on an optical breadboard and is acoustically insulated in a plastic box. A pad made of viscoelastic polymeric material [114] is placed underneath the breadboard to damp and absorb any vibration.

In the servo loop, the frequency deviation between the slave laser and the master laser is adjusted by translating the PZT. For better laser frequency stabilization, the servo bandwidth needs to be greater than the frequency range of the environmental fluctuation. In the injection-locked laser system, the mechanical resonance of the PZT mounting structure would be one of the limitations.

3.3.2 Piezo-electric transducer (PZT) mounting structure

An injection-locking laser system requires mechanisms to actively compensate the detuning between the master laser and the slave laser. The feedback loop can be formed by an electronic servo circuit and a PZT actuator. The PZT used in the laser system is a square piezo-chip with the dimension of 5 mm x 5mm x 2mm. The PZT is bonded to a mirror of the slave laser cavity to tune the cavity length in order to scan the frequency of the slave laser. The other side of the PZT is mounted on a metal block to reduce mechanical perturbation. To obtain a flat frequency response, the material and the shape of the mounting structure need to be carefully selected.

In Ref. [115], several metals were tested: aluminum, copper, copper filled with lead, and M2052 [116], [117]. M2052 is a manganese-based alloy containing copper, nickel and iron. It is a high damping material whose damping capacity is near rubber. In addition, M2052 has excellent workability so that it can be easily

shaped into desired shapes. Besides using a cylindrical-shaped metal block with flat head, some of the metal mounting structure is tapered for comparison. The tapered mounting structure is machined following the design principles of reference [118].

The mechanical response of the PZT actuator can be measured by placing the PZT mounting structure at one arm of a Michelson interferometer (Figure 3.11). The interference signal contains information of the longitudinal displacement of the PZT. Then, the amplitude and the phase response can be calculated at one frequency, and repeated at different frequencies to obtain the frequency response spectrum. In Figure 3.12, the amplitude responses for different conditions are plotted. There are different resonant peaks for different materials and different shapes; among them, M2052 has flat response up to 140 kHz. There is no significant difference between the tapered and the flat mounting structures.

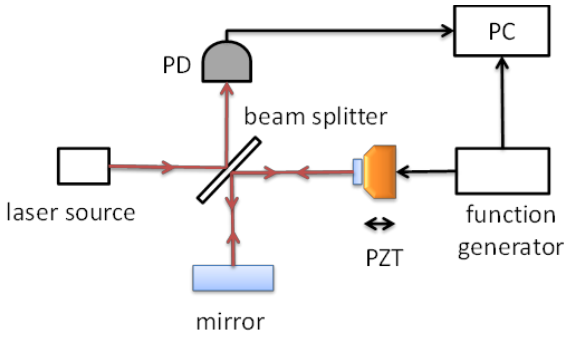

Figure 3.11 Schematic of the Michelson interferometer

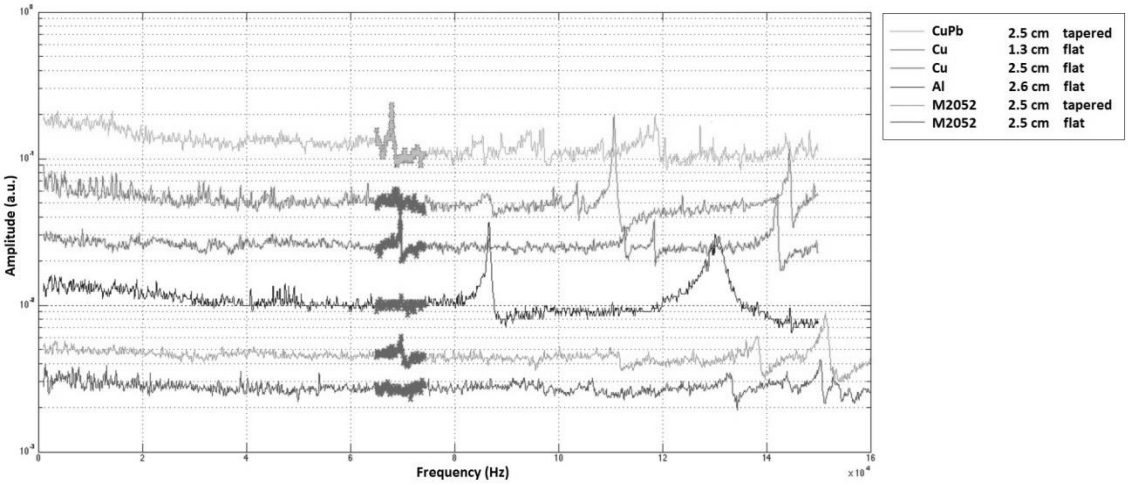

Figure 3.12 Amplitude response of the PZT actuator made of different materials and different designs. The traces from top to bottom corresponding to the list at the right hand side in the same order.

CHAPTER 4 INJECTION-LOCKED LASER OUTPUT PERFORMANCE AND CHARACTERISTICS

In this chapter, the key results of the injection-locked operation of the OPSLs are shown and the key factors to operate an injection-locked laser are discussed. The output performance of the injection-locked laser is investigated by varying some critical parameters such as output coupling, injection wavelengths and injection power. In addition, the output power is further improved by operating at a lower temperature owing to higher semiconductor material gain. We also estimate the saturation intensity of the OPSL by surface photoluminescence (PL) measurement. The output power and the gain saturation behavior of OPSLs are deduced. Since the injection-locked laser is operated by synchronizing the resonant frequency of the slave laser cavity with the master laser through the electronic feedback loop, the frequency of the output of the slave laser follows that of the master laser. In order to assess the added frequency noise by the slave laser, the relative phase noise from beat note between the injection-locked laser and the master laser is measured.

4.1 Laser-locking observation

In order to verify whether the injection-locking takes effect, we can monitor some characteristics in the laser system (Figure 4.1). The top row in Figure 4.2 shows the error signal (measured after the mixer), the slave laser output (PD2) and the Fabry-Perot scanning recorded from the oscilloscope. The bottom row shows the spectrum of the laser measured by an optical spectrum analyzer (OSA, HP 86140A). When sweeping the PZT actuator in the slave laser cavity, the master laser and the slave laser operate independently. We can see two distinct peaks on the OSA. The FWHM of the free-running slave laser ranges from 2- to 3-nm wide depending on the pump power. When the servo loop is closed, the frequency of the slave laser is locked to that of the master laser as shown in the right column. There is only one narrow peak at the master laser wavelength shown on the OSA. All the power is contained in the spectral component of the master laser, and the components of the free-running signal vanish. The actual spectral bandwidth is less than the resolution bandwidth of the optical spectrum analyzer, 0.07nm. The scanning Fabry-Perot signal shows a single frequency component with no parasitic mode oscillating. When the servo gain is too high, the servo loop starts to oscillate. When it happens, the frequency excursion goes beyond the range needed to force single frequency operation at that of the injected light. The remaining free running signal on the OSA is another indication of imperfect locking.

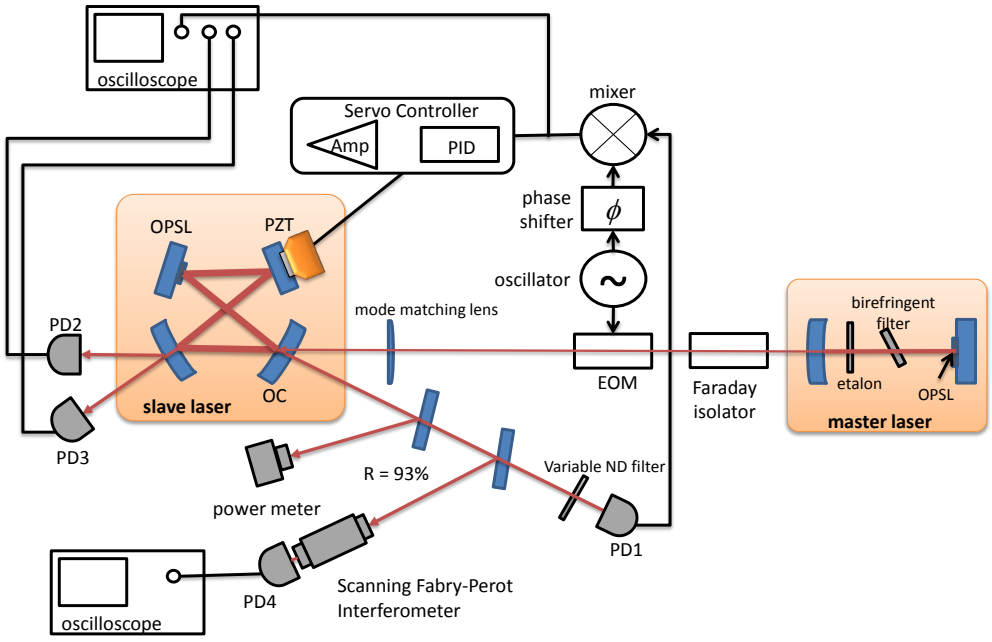

Figure 4.1 Schematic of injection-locked OPSL.

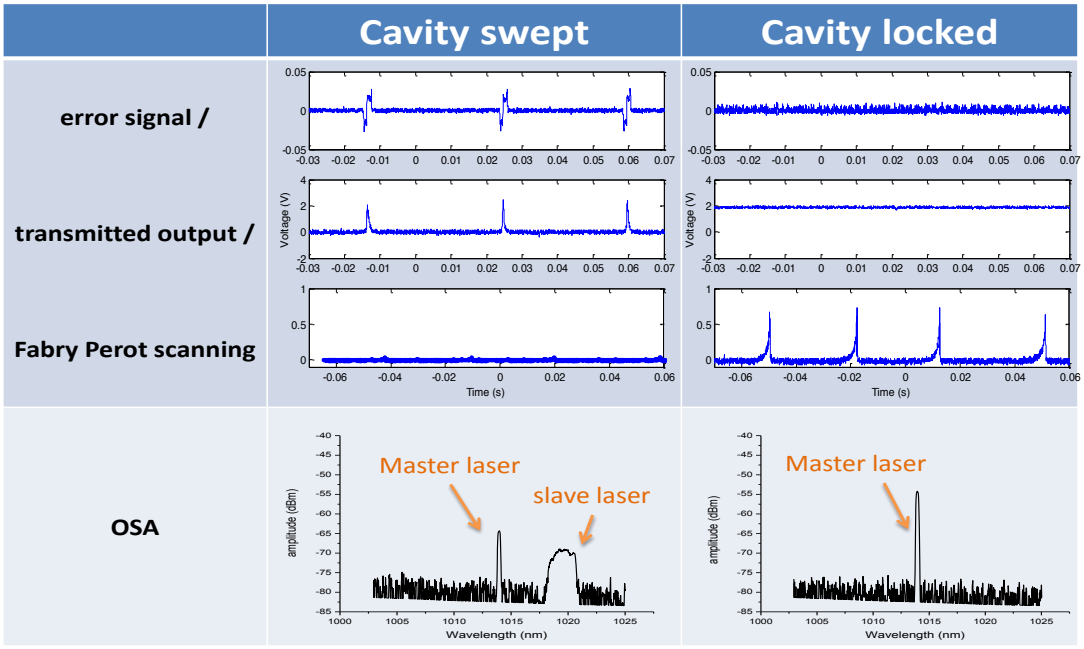

Figure 4.2 Laser-locking observations. Top row: screenshots from the oscilloscope.

Bottom row: laser spectra from the OSA

4.2 Output performance with different output couplers

The output powers of the injection-locked laser are compared by varying the transmission of the output couplers. Three output couplers with the transmission of 1%, 3% and 4% are used. By injecting 500 mW at 1016 nm from the master laser, the output powers of the free-running and injection-locked operation are shown in Figure 4.3. The slave ring laser operates bidirectionally under free-running condition. Therefore, the total power of the free-running laser is the sum of the two outputs that are measured right after the output coupler. When operating the injection-locked laser, a partial mirror with a reflectivity of 93% is used to pick off some of the laser signal for generating the error signal (as shown in Figure 4.1). In order to fairly compare the output power of the injection-locked laser and the free-running laser, the total power of the free-running laser is multiplied by 93% in Figure 4.3. The partial mirror with R = 93% is chosen so that the pick off ratio of the output power is constant from the low to high pump power. A higher output power could be demonstrated if a mirror with higher reflectivity was used. In injection-locked operation, the laser is forced to emit unidirectionally in the same direction as the injecting laser beam because the entire parasitic signal, including the backward propagating mode, are suppressed. The slave laser acts as an amplifier and the output power of the injection-locked laser grows with the pump power. The measurement was stopped at the onset of parasitic oscillation, which can be observed on the optical spectrum analyzer.

The parasitic oscillation can be also observed along the counter propagation direction at PD3 in Figure 4.1, where the beam leaks out from the HR mirror.

Among the three output couplers in Figure 4.3, parasitic oscillation occurs at low pump powers when using T = 1% output coupler. With larger output couplers, T = 3% and 4%, the laser could be injection-locked without the onset of parasitic oscillation beyond 20 W of the pump power. For the T = 3% condition, the injection-locked laser has the best output efficiency with its output power in injection-locking mode higher than in free-running mode, by more than what is injected. With 20 W of pump power, the output power of the injection-locked laser is 4.9 W, which is 1.5 W higher than the output of the free-running laser. The difference is greater than the amount of power (500mW) that is injected. The slave laser does not reach threshold with T = 4% output coupler in free-running operation, indicating relatively low unsaturated optical gain of the semiconductor material. Upon external signal injection, additional power builds up in the laser cavity. The circulating power inside the resonator initiated by the externally injected signal can give rise to the extraction of an appreciable amount of power. When the laser is injection-locked, the output power grows with increasing pump power, operating as an amplifier.

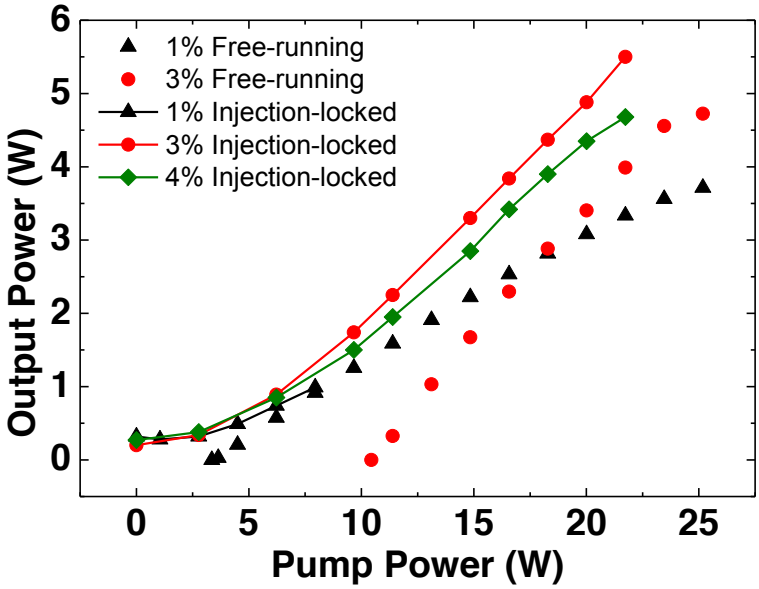

Figure 4.3 The output power of the injection-locked laser and the free-running slave laser using different output couplers. The injection-locked laser is injected by 500 mW of the master laser power at 1016 nm

4.3 Gain Saturation analysis

In a laser system, a signal is amplified after passing through a gain medium. For the semiconductor laser, the optical gain is associated with carrier recombination. As the pump intensity increases, the optical gain increases with the carrier density and becomes saturated. Although the gain from an OPSL device is lower than many of the bulk-crystal solid-state laser media, the saturation intensity could be higher. The saturation intensity is defined as the

value of signal intensity that saturates the gain down to half of its small signal or unsaturated value, and it is given by:

$$g = \frac{g_0}{1 + I/I_{sat}} \tag{4.1}$$

where g and g_0 represent the optical gain in saturated and unsaturated condition respectively. I is the intracavity intensity of the signal, and I_{sat} is the saturation intensity. When the laser is in the steady state, the gain is clamped at the value that is equal to the total loss of the cavity, which means $g = g_0$ at the lasing threshold. With higher saturation intensity, more intracavity power can build up before the gain is saturated. By studying the saturation intensity of an OPSL, we are able to assess how much power can be extracted from a laser cavity.

The saturation intensity can be estimated by the surface photoluminescence (PL) measurement. The overall gain spectrum of an OPSL is determined by the combination of the quantum well gain and the microcavity resonance formed between the top surface and the DBR. The device has an anti-reflection (AR) coating at the signal wavelength, so the microcavity effect is weakened. With a quarter-wave thick layer of HfO_2 (n = 1.97@ 1015 nm) coating on the InGaP (n = 3.22) window layer, the residual reflectivity is estimated to be 0.9%, substantially lower than 28% for the uncoated surface. Figure 4.4 shows the surface PL spectra with different injection wavelengths at the same pump power of 15 W. The mode radius is ~ 250 μm. The surface PL was collected slightly off the beam propagation direction at an angle of 10^o. We assume the distribution of

the emitted photons is uniform within a small angle. The observed spectra contain the surface PL as well as strong scattered laser signal which is neglected in the analysis. The signal amplitude of PL indicates the amount of photons generated by radiative recombination of carriers. The optical gain can be approximated to be linear with the carrier density. The dependency of the gain g and the carrier density N can be written by [119]:

$$g \approx a\left(N - N_{tr}\right) \tag{4.2}$$

where a is the differential gain and N_{tr} is the transparency carrier density.

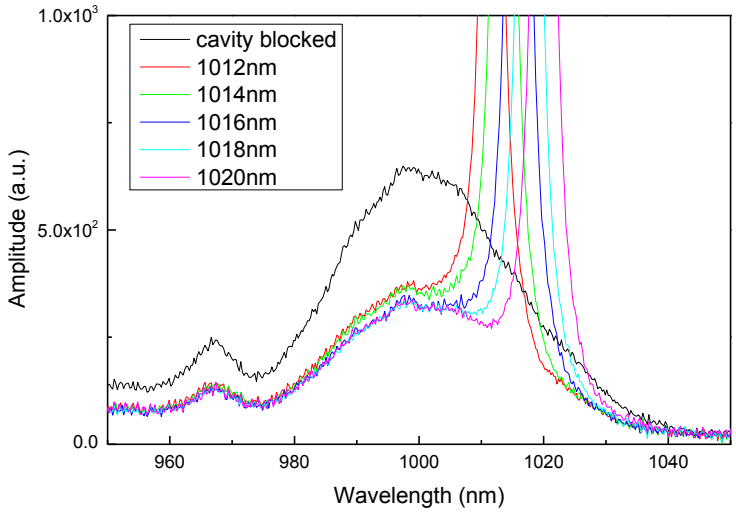

Figure 4.4 Surface PL spectra with non-lasing condition (cavity blocked) and injection-locked operation

When the slave laser starts to oscillate, the optical gain becomes saturated, and thus the PL intensity is reduced. When the laser cavity is blocked, we assume the carrier density is at a low degree of saturation since there is no circulating power inside the laser cavity to saturate the gain. By comparing the PL intensity with lasing and non-lasing condition, the saturation intensity can be estimated. The ratio g_0 / g obtained from equation (4.1) can be directly related to the ratio of signal amplitude from the PL measurement with and without the cavity-blocked. The reduction of the PL of the injection-locked laser has nearly homogenous response. This indicates that the quantum well gain broadening is fairly homogenous in the measured spectral range. The ratio g_0/g is averaged from 990 nm to 1000 nm to avoid the influence of the laser signal and to be in the high reflectivity range of the DBR, which is from 980 nm to 1060 nm according to the TDR measurement (Figure 2.6) of the device used in the slave laser. The estimated values of saturation intensity of different injection wavelengths are listed in

Table 4.1. The gain saturation has a similar response at the wavelength around 1016 nm to 1020 nm with saturation intensity of ~100 kW/cm^2. The saturation intensity is higher when using a shorter injection wavelength. This may be because when the injection wavelength is away from the spectral peak of the laser gain, the intracavity intensity is less effective in causing saturation. The effective saturation intensity is frequency dependent, and it can be described by [120]:

$$I_{sat}(\omega) = I_{sat}(\omega_0) \times \left[1 + \left(2\frac{\omega - \omega_0}{\Delta\omega}\right)\right] \simeq I_{sat}(\lambda_0) \times \left[1 + \left(2\frac{\lambda - \lambda_0}{\Delta\lambda}\right)\right] \quad (4.3)$$

where ω_0 is the center frequency and $\Delta\omega$ is the linewidth of the laser. It can also approximate to the wavelength dependent form with the center wavelength λ_0 and the gain bandwidth $\Delta\lambda$. From the equation, the effective saturation intensity becomes larger when the detuning is larger, and it changes more rapidly when the laser linewidth is narrower. The experimental data is fitted with equation (4.3) in Figure 4.5. The fitting curve assumes $\lambda_0 = 1018$ nm, $\Delta\lambda = 23$ nm and $I_{sat} = 98.5$ kW/cm^2, showing good agreement with the experimental results. The free running wavelength emits at 1017.9 nm in the same pumping condition. The analysis of the surface PL could be used for the estimation of the center frequency and the linewidth of the gain, which provides another way to characterize an OPSL device.

Table 4.1 The saturation intensity with different injection wavelength

Wavelength (nm)	Output Power (W)	Intracavity Intensity (kW/cm^2)	N_{sat}/N_0	Saturation Intensity (kW/cm^2)
1012	2.76	93.3	0.576	126
1014	2.75	93.0	0.562	119
1016	2.80	94.7	0.517	101
1018	2.79	94.4	0.513	99
1020	2.82	95.4	0.511	100

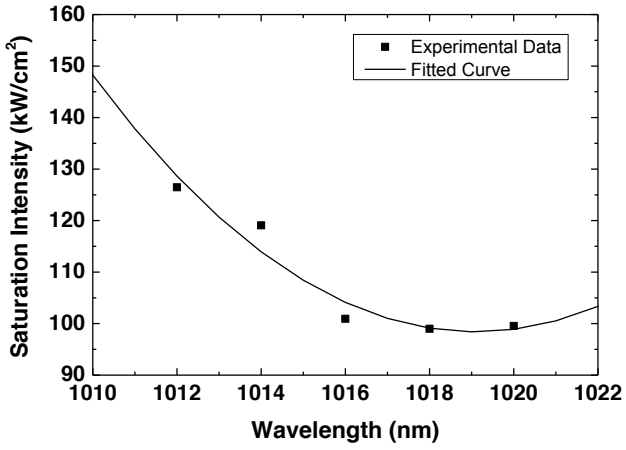

Figure 4.5 Wavelength dependence of the saturation intensity

4.4 Output power simulation with gain analysis

In the previous section, the saturation intensity of the OPSL was assessed based on the surface PL analysis. By knowing the saturation intensity, we can further simulate the gain behavior of OPSLs. The threshold condition of the laser can be expressed as:

$$R_{oc}R_m \exp[gL] = 1 \tag{4.4}$$

where R_{oc} is the reflectivity of the output coupler. R_m is the amount of light remaining in the cavity after one round-trip, accounting for the passive loss of the cavity including the imperfect coatings of HR mirrors and the surface scattering of the OPSL device. If the passive loss in each roundtrip is δ, $R_m = 1 - \delta$. g is the unsaturated gain at the lasing threshold. L is the effective length of the gain

medium, which is a product of parameters that are the thickness of each quantum well, the number of quantum wells, the longitudinal confinement factor and factor of 2 for double pass [30]. L is given to be 200 nm in the following calculation.

When above the lasing threshold, the saturated gain is clamped at a constant value that is equal to the total intracavity loss, which is the sum of the passive loss and the transmission of the output coupler. In the steady state, the relation between the small signal gain g_0 and the saturated gain g can be written as:

$$g = \frac{g_0}{\left(1 + P_{\text{intra}} / P_{sat}\right)} \tag{4.5}$$

where P_{intra} is the intracavity power. P_{sat} is the saturation power, which is given by:

$$P_{sat} = I_{sat} \times A \tag{4.6}$$

where I_{sat} is the saturation intensity, and A is the effective mode area at the gain chip. The output power of the laser is given by the intracavity power multiplied by the transmission of the output coupler (T_{oc}). Hence, the calculated output power is:

$$P_{out} = T_{oc} P_{\text{intra}} = T_{oc} P_{sat} \left(\frac{g_0}{g} - 1 \right) \tag{4.7}$$

The saturation power (or the saturation intensity) is defined as the power (or the intensity) at which the gain is reduced to one-half of the unsaturated value

(the small signal gain). It is a key factor that contributes to the output power and determines how the circulating power saturates the laser gain medium. On the other hand, the small signal gain g_0 is a property of the gain medium and is a function of pump intensity, i.e. the pump power divided by the effective pump area. When the saturation intensity is constant, the higher the pump power, the higher the small signal gain, and hence the more the resonant power. Due to the spectral shift of the gain, the transmission of the output couplers (T_{oc}) is slightly different when the emission wavelength changes (Figure 4.6). Therefore, when calculating the output power, we have taken the output coupling transmission for the actual operating wavelength into account.

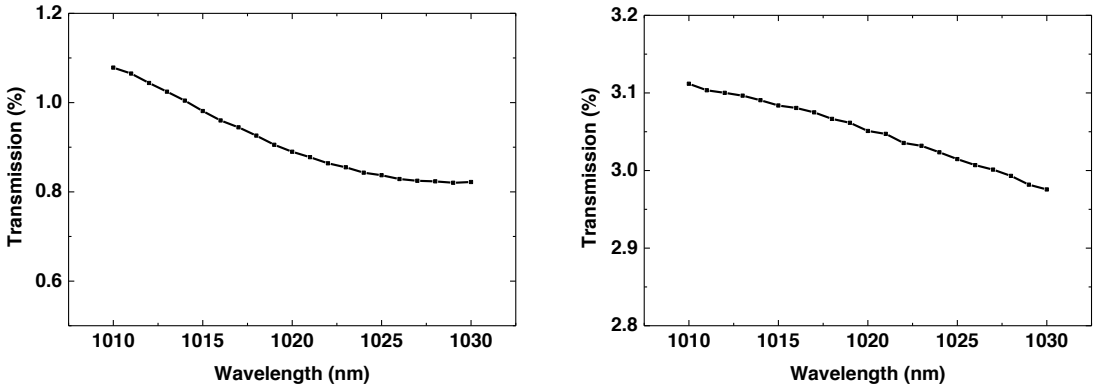

(a) T = 1%

(b) T = 3%

Figure 4.6 Output coupler transmission at the laser emission wavelengths

In order to express the small signal gain g_0 as a function of pump power, we approximate g_0 by:

$$g_0 = g_{th} + c_1\left(P_p - P_{th}\right) + c_2\left(P_p - P_{th}\right)^2 \quad \left(unit: cm^{-1}\right) \tag{4.8}$$

where g_{th} is the saturated gain at threshold pump power, and c_1 and c_2 are fitting coefficients. The passive loss is assumed to be 1.4% while the saturation intensity is assumed to be 100 kW/cm^2 as we previously estimated. In some literature, the quantum well gain is expressed as a natural logarithm function of current density [30], [119]. However, the logarithm function does not apply to our experimental data since we were not able to use the same set of parameters to express both conditions when the output couplings are 1% and 3% respectively. The polynomial equation is adopted since it can fit well within the pump operation range of our experiment. Figure 4.7 shows the small signal gain that is calculated from equation (4.8) with $c_1 = 160$ and $c_2 = -2$. The linear gain G_0 is calculated by the relation:

$$G_0 = \exp\left(g_0 L\right) \tag{4.9}$$

We note that the gain expression may only apply to the condition when the laser is above threshold since the OPSL does not lase when a T = 4% output coupler is used. From the equation (4.4), the OPSL could have reached the lasing threshold when the pump power is above 14 W. However, the OPSL did not lase, perhaps because the absorbed pump power would convert to heat that

increases the quantum well temperature, which would reduce the optical gain. Also, the accumulated carriers result in more complicated carrier recombination such as Auger recombination. This will reduce the overall radiative efficiency. Therefore, the gain calculation cannot be used in the non-lasing condition. In Figure 4.8, the fitted curve based on the equation (4.7) and (4.8) can fit very well with the experimental results. For this calculation, we assume that the heat generated in the OPSL devices are about the same when using two different output couplers. The emission wavelength is about 1 nm longer with the 1% output coupling than with the 3% output coupling at the same pump power (Figure 3.7). Given the thermal shifting rate of 0.23 nm/K, it is equivalent to a temperature difference of 4^{o}C. In this case, the difference in the small signal gain is ignored.

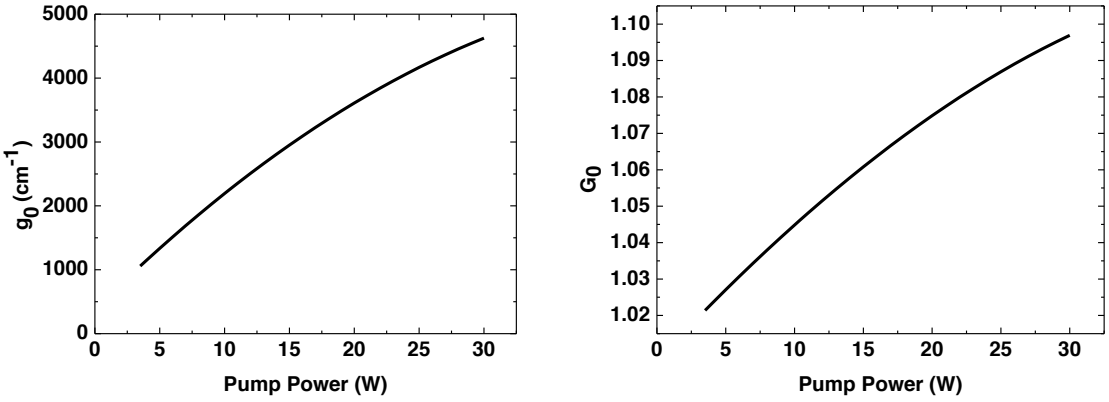

Figure 4.7 The small signal gain as a function of pump power

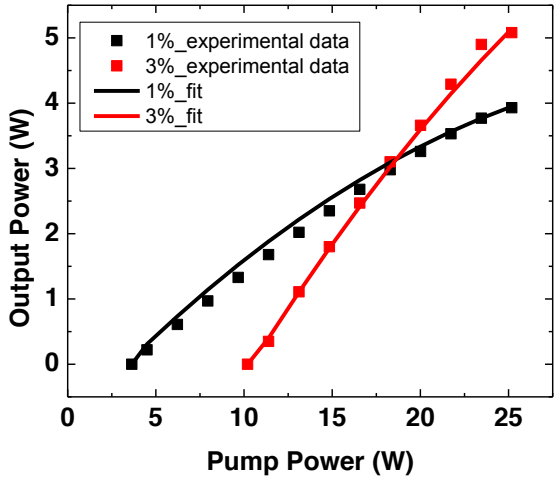

Figure 4.8 Output power fitting curve

From the free-running laser experiment, the small signal gain and the saturation intensity of the OPSL have been deduced. To simulate the output power of the injection-locked laser, we assume that a single-frequency signal with field amplitude E_{inc} is incident into the slave laser cavity. We define E_1 as the incident field to the gain medium and E_2 as the output field from the gain medium. E_{ref} is the reflected field from the output coupler and represents the output signal of the injection-locked laser. We can write the equations to describe the relation of these fields as follows on the condition that the slave laser cavity is locked to the master laser input:

$$E_1 = itE_{inc} + rr_m E_2 \tag{4.10}$$

$$E_{ref} = rE_{inc} + itr_m E_2 \tag{4.11}$$

where r and t are the reflection coefficient and the transmission coefficient of the output coupler, and $r^2 + t^2 = 1$. r_m relates to the passive loss of the cavity, which is equal to $\sqrt{1-loss}$. As the pump power increases, the fields start to build up in the slave laser cavity. The degree of saturation is governed by the ratio of the circulating power and the saturation power. The saturated gain is the ratio between the extracted output power from the device and the incident power to the device,

$$G = \frac{|E_2|^2}{|E_1|^2} = G_0 \exp\left[-\frac{|E_2|^2 - |E_1|^2}{P_{sat}}\right] \tag{4.12}$$

where $G_0 = \exp(g_0 L)$ is the unsaturated gain and is a function of pump power in equation (4.8). To simplify the calculation, we define the quantity of power as the square of the electric field amplitude, $P = |E|^2$. Assume there is no phase difference between E_1 and E_2, the relation can be expressed as:

$$E_2 = \sqrt{G}E_1 \tag{4.13}$$

Substituting equation (4.13) into equation (4.10) and rearranging the equation, we arrive at:

$$P_1 = |E_1|^2 = \left(\frac{it}{1 - rr_m\sqrt{G}} \right)^2 P_{inc} \tag{4.14}$$

The output power of the injection-locked laser is calculated by substituting equation (4.13) and (4.14) into equation (4.11) and taking the square of the whole equation.

$$P_{out} = P_{ref} = |E_{ref}|^2 = \left(\frac{r - r_m\sqrt{G}}{1 - rr_m\sqrt{G}} \right)^2 P_{inc} \tag{4.15}$$

The parameters are assumed based on the calculation of the free-running laser in the previous chapter with the passive loss of 1.4% and the saturation intensity of 100 kW/cm^2. The injection beam is assumed to be perfectly mode matched. The simulated injection-locked output power with two different output coupling conditions are plotted along with the experimental data in Figure 4.9, which agrees well with experimental results.

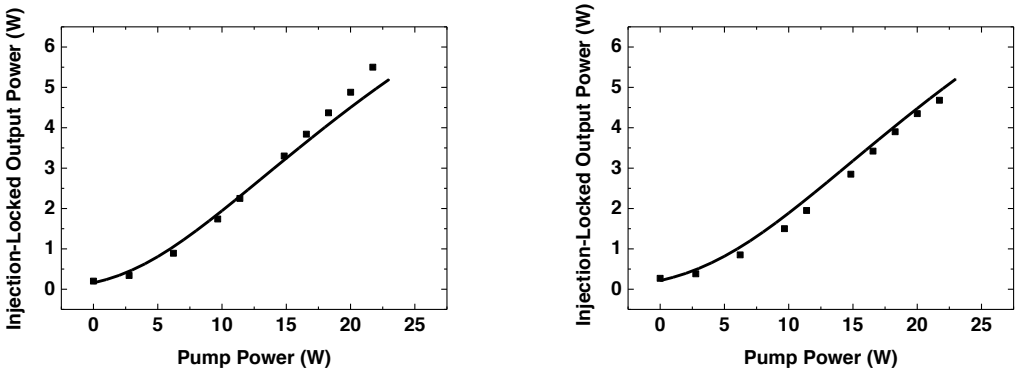

(a) T = 3% (b) T = 4%

Figure 4.9 The simulated output power (line) and the experimental data (dot) of the injection-locked laser with 500 mW of injection power from the master laser.

4.5 Comparison of saturation behavior of the optical gain in different materials

From the experimental results of our injection-locked OPSL, we found that more power from the master laser is required compared to other solid-state lasers in order to maintain the injection-locking operation. A Nd:YAG laser can be injection-locked with 40 mW of master laser power [99], but an injection-locked OPSL requires several hundreds of mW to several watts. This can result from the higher saturation intensity of OPSL, which we have estimated it to be 100 kW/cm^2. This value is about 30 times higher than the saturation intensity of Nd:YAG laser (2.9 kW/cm^2) [105]. With higher saturation intensity, we can expect higher injection intensity is required for injection-locked operation of OPSLs. A Nd:YAG laser only requires several tens mW to maintain a stable output power of 10 W level [99], whereas the injection-locked OPSL requires more than several hundred milliwatts of injection power. An injection-locked Ti:Sapphire laser requires only tens of mW of injection power to keep watts level of output power locked [91], [103]. The saturation intensity of Ti:Sapphire is 260 kW/cm^2 [121], which is even higher than our estimated value of saturation intensity of OPSLs. However, in order to generate watts level of output power from the Ti:Sapphire laser, the mode size is usually controlled at several tens μm inside the gain medium, hence requiring near-diffraction-limited pump lasers, which are expensive and complex, and limited in their output powers. On the other hand, the mode sizes of OPSLs are typically several hundred microns. Therefore, even

though the saturation intensity of OPSL device is about two times less than the Ti:Sapphire, the required injection power of OPSLs is still higher.

We investigated how the saturated gain and the intracavity power behave for the two different laser materials by considering the electric field and the gain saturation inside the injection-locked laser. In the previous section, the small signal gain of OPSL has been calculated by fitting with the experimental data, and the fitting equation is written as:

$$g_0 = g_{th} + 160\left(P_p - P_{th}\right) - 2\left(P_p - P_{th}\right)^2 \quad \left(unit: cm^{-1}\right) \tag{4.16}$$

where $g_{th} =$ 2257.6 cm^{-1}, $P_{th} =$ 10.4 W are given for the T = 3%.

The small signal gain coefficient of the Nd:YAG laser is given by the following equation [105]:

$$g_0 = \frac{\sigma_s \tau_f \eta}{h\nu V} P_p = \frac{\eta}{I_{sat} V} P_p \quad \left(unit: cm^{-1}\right) \tag{4.17}$$

where the saturation intensity I_{sat} is the product of the stimulated emission cross section σ_s and the upper state lifetime τ_f divided by the photon energy $h\nu$. The overall efficiency η is the combination of all the efficiency factors, which are the quantum efficiency, the pump absorption efficiency and the mode overlapping efficiency. The value of η is assumed to be 0.6 with the quantum efficiency to be 0.76, pump absorption efficiency to be 0.81 and the mode overlapping efficiency to be 0.97. V is the volume of the gain medium. We assume a spot diameter of

500 μm and a gain medium length of 0.6 cm. The equation shows that the small signal gain coefficient is proportional to the pump power. The small signal gain coefficients of OPSL and Nd:YAG are converted to the linear gain via the relation: $G = \exp[g_0 L]$ and are plotted in Figure 4.10. It is shown that OPSL has a much lower small signal gain compared to the Nd:YAG laser.

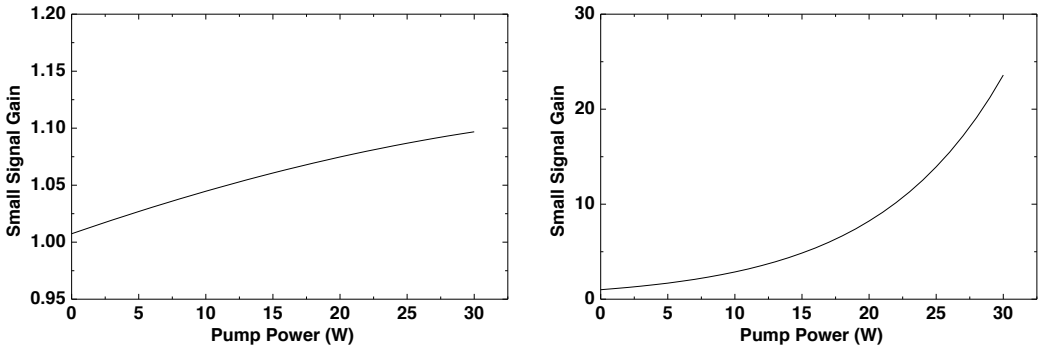

(a) OPSL (b) Nd:YAG

Figure 4.10 Comparison of small signal gain

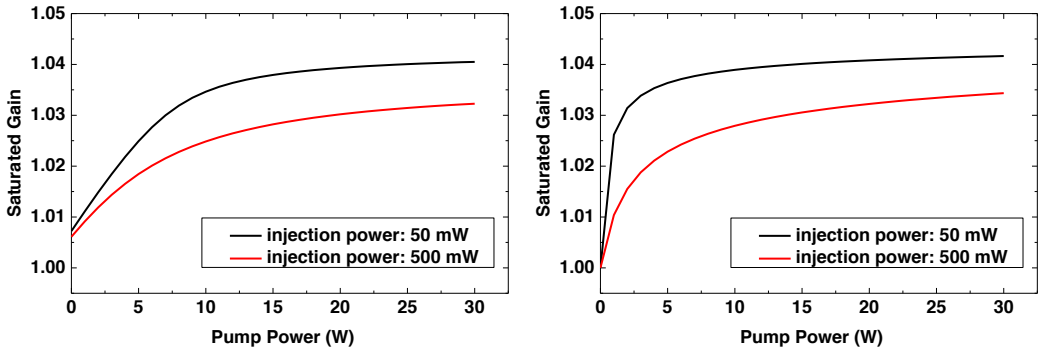

(a) OPSL (b) Nd:YAG

Figure 4.11 Saturated gain calculation of two gain media with different injection

Following the calculations in the previous section, assuming that the two lasers have the same output coupling (3%) and the same intracavity loss (1.4%), the saturated gain of the injection-locked lasers using two different materials are plotted in Figure 4.11. At a low pump power, the Nd:YAG laser shows a much steeper slope indicating a much higher small signal gain compared to the OPSL. As the pump power increases, the Nd:YAG laser saturates at very low pump power. On the other hand, the OPSL saturates gradually until the pump power reaches lasing threshold. At a higher pump power, the saturated gains of two injection-locked lasers asymptotically approach to the same values. A higher injection power lowers the saturated gain to a smaller value.

In Figure 4.12, the values of the intracavity power are compared between two different materials. The three solid lines represent how the intracavity power varies in free-running and injection-locked condition with different injection power. The dash lines show the saturation power where the small signal gain drops to its half value, and it is an indication of how hard the intracavity power saturates the gain medium. The lower small signal gain of OPSL requires higher pump power to accumulate intracavity power, and more injection power is needed in order to saturate the internal gain further. This can explain why we have to use a higher injection power to operate the injection-locked OPSL.

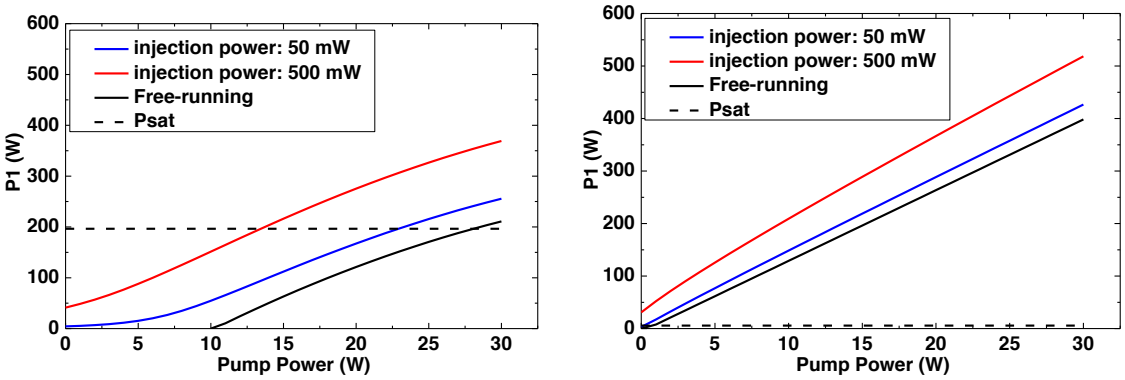

(a) OPSL (b) Nd:YAG

Figure 4.12 Intracavity power calculation of two gain media with different injection power

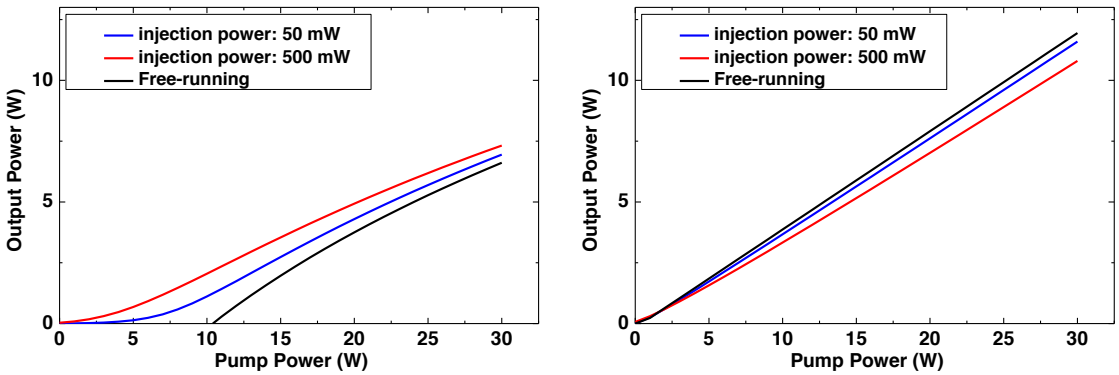

(a) OPSL (b) Nd:YAG

Figure 4.13 The calculated output power using two gain media

The calculated output powers of two lasers are plotted in Figure 4.13. For the injection-locked OPSL, the output power is enhanced with a higher injection power. As for the injection-locked Nd:YAG laser, the output power decreases when the injection power is higher. This is mainly due to the Nd:YAG laser is under coupling (i.e. the transmission of the output coupler is smaller than the optimum value) for this particular case. In the simulation, we applied the same output coupling of 3% and intracavity loss of 1.4% for comparison between two gain media. However, in order to optimize the operation of a Nd:YAG laser, a higher output coupling is usually used to extract more power from the laser cavity since the optical gain of the Nd:YAG laser is much higher. This comparison still indicates how the gain behaves differently when using different gain media with different saturation intensity and small signal gain. With higher saturation intensity and lower small signal gain, more injection power is required for the injection-locked OPSL to saturate the gain medium in order to generate as much power as an injection-locked Nd:YAG laser.

4.6 The optimum injection wavelength

The emission wavelength of a free-running OPSL is determined by the combination of the quantum well gain and the microcavity resonance at a given temperature. When the pump intensity increases, the free-running wavelength shifts to the longer wavelength side since the gain structure is heated up and the

bandgap of the quantum well becomes smaller. At a temperature of 15^{o}C, the free-running slave laser emits from 1014 nm to 1020 nm depending on the pump power as indicated in Figure 3.7. For the injection-locked laser system, we investigated how the output performance is affected by different injection wavelengths and different injection power using the T = 3% output coupler. As shown in Figure 4.14, the best injection wavelength is from 1014 nm to 1016 nm. When the injection wavelength is shorter, the slope efficiency decreases at higher pump powers while it increases when the injection wavelength is longer. Similar to the free-running condition, it is a dynamic effect that the optimum injection wavelength shifts as the gain peak of the injection-locked laser shifts with elevated pump power. However, the optimum injection wavelength is always shorter than the free-running wavelength by about 2 nm. Therefore, the operating temperature of the injection-locked laser should be adjusted so that the free-running wavelength is 2 to 3 nm longer than the targeted wavelength for the optimum output power. With the injection wavelength at 1018 nm and above, the laser remains injection-locked at 25 W of pump power, whereas parasitic oscillation starts to occur at the same pump power with the injection wavelength at 1016 nm.

Higher injection power extends the locking ability to a higher pumping rate. In addition, higher injection power also broadens the locking spectral range. With 1 W of injection power, the output efficiency becomes quite similar from 1014 nm to 1020 nm.

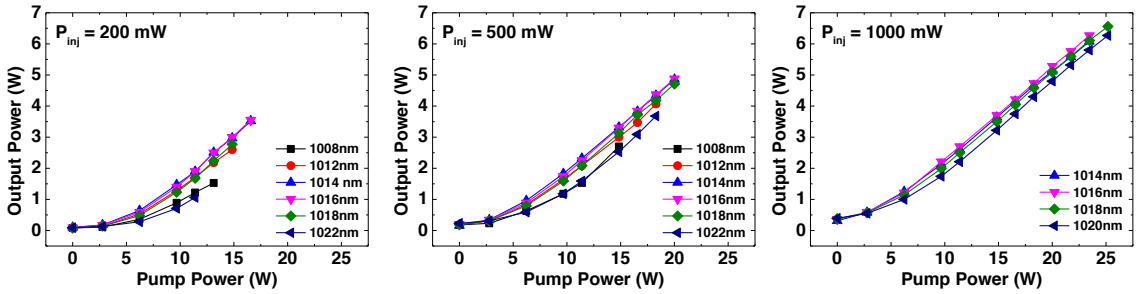

(a) (b) (c)

Figure 4.14 The output power as a function of total pump power for different injection wavelengths from 1008 nm to 1022 nm. Different injection powers are compared: (a) 200 mW (b) 500 mW (c) 1000 mW.

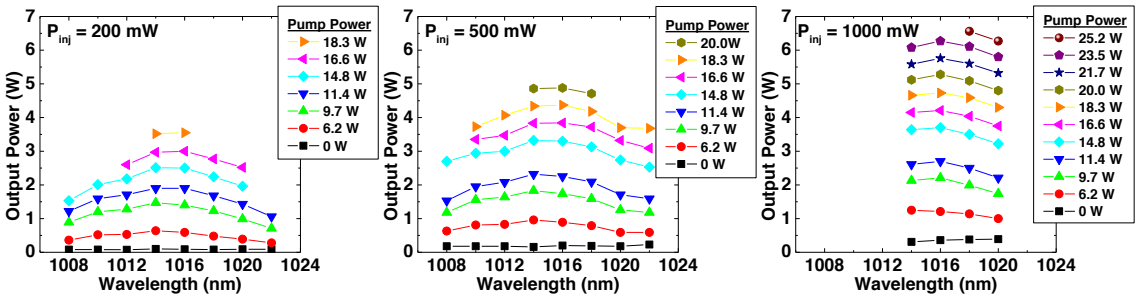

(a) (b) (c)

Figure 4.15 Wavelength dependent output power of the injection-locked OPSL with incremental pump power. Different injecting powers are compared: (a) 200 mW (b) 500 mW (c) 1000 mW.

In the experiment, it is found that the gain peak of the injection-locked laser shifts to longer wavelengths with higher pump powers, but the optimum injection wavelength always remains shorter than the free-running wavelength.

This can be explained by the difference in dissipated power that heats up the chip causing a different wavelength shift. The injection-locked laser starts to emit photons when the pump power of the slave laser increases from zero, as the slave laser acts as an amplifier. The carriers, which could have recombined through other paths such as nonradiative recombination or Auger recombination under the free-running operation, recombine radiatively through stimulated emission. Higher radiative efficiency results in not only more extracted power from the slave laser, but also less dissipated power and hence lower temperature rise in the gain medium. Consequently, the preferable wavelength of injection-locking is shorter compared to the free-running wavelength of the slave laser at the same pump power. Moreover, the output power of a free-running OPSL rolls over when the laser chip heats up, and the quantum well gain and microcavity resonant center misalign spectrally. The optical efficiency of the injection-locked laser is determined by how well the gain peak of the slave laser aligns with the master laser spectrum. The gain peak of the injection-locked laser shifts less than the free-running laser providing higher output efficiency and higher rollover point. The free-running slave laser rolls over at 23 W of pump power with T = 3% output coupler as seen in Figure 4.3. On the other hand, the injection-locked laser grows linearly with no sign of rollover, with its output power limited by the onset of parasitic oscillations.

From the discussion below, the dissipated power and the thermal resistance with respect to the dissipated power are estimated. The difference in the temperature

rise between the injection-locked laser and the free-running laser is deduced. The dissipated power can be written as the sum of the dissipated power in the RPG and the DBR:

$$P_{diss} = P_{RPG} + P_{DBR} \tag{4.18}$$

To calculate the dissipated power in the active region (RPG), we consider conditions at the threshold and above the threshold:

$$P_{RPG} = T \times A \times \left[P_{th} \times \left(\eta_{rad\_th} \frac{\lambda_p}{\lambda_{las}} \right) + \left(P_p - P_{th} \right) \times \left(\eta_{rad\_las} \frac{\lambda_p}{\lambda_{las}} \right) \right] \tag{4.19}$$

where T is the transmission of the pump power at the air-chip interface and A is absorption ratio in the active region. In the calculation, T = 96%, obtained from the surface reflectivity measurement, and A = 80%, estimated from the simulation, are used. P_{th} and P_p are the threshold pump power and the pump power, respectively. η_{rad} represents the radiative quantum efficiency and is the ratio between the number of emitted photons and the absorbed photons per unit time. Below threshold, the carrier number builds up as the pump power is increased, raising the spontaneous emission rate and increasing the radiative quantum efficiency until the lasing threshold is reached. When the pump power goes above the threshold value, stimulated emission dominates the photon generation process and saturates the optical gain, so η_{rad} becomes a larger constant after the onset of lasing.

The radiative quantum efficiency of the laser is estimated from the output performance of the free-running laser,

$$P_{las} = \left(P_p - P_{th}\right)\eta_{diff} \tag{4.20}$$

where the differential efficiency η_{diff} is

$$\eta_{diff} = \eta_{out}\eta_{quant}\eta_{rad}\eta_{abs} \tag{4.21}$$

The calculation details can be found in ref [49]. The differential efficiency of the free-running slave laser is 38%. With a T = 3% output coupler and an estimated 1.4% intracavity loss, the output coupling efficiency η_{out} is 68.8%. The quantum defect η_{quant} is 80% with the pump wavelength at 808 nm. The pump absorption efficiency η_{abs} is 76.8%, which is the product of the pump transmission T and the absorption ratio A that are given in the previously. The radiative quantum efficiency above the threshold is calculated to be around 90%. The radiative quantum efficiency at the threshold η_{rad_th} is chosen to be 47%.

After passing through the active region, the residual part of pump power is mostly absorbed and converted into heat in the DBR region. The dissipated power in the DBR is calculated as:

$$P_{DBR} = T \times (1 - A) \times r_{heat} \times P_p \tag{4.22}$$

where the heat conversion ratio (r_{heat}) is assumed to be 90%. The remaining power becomes the loss of the system due to surface scattering or spontaneous

emission that does not contribute to heat [122]. The dissipated power in the DBR is linearly proportional to the pump power, and is the same for both the free-running mode and the injection-locked mode.

The calculated dissipated power is shown in Figure 4.16(a). The difference in dissipated power is nearly a constant of 2.6 W above threshold. The difference in dissipated power can be translated into the wavelength shift through the thermal impedance of the OPSL device in the slave laser. The dependence of the wavelength shift per watt ($\Delta\lambda/\Delta P$) is obtained by relating the free-running wavelengths to the dissipated power, which is 0.71 nm/W. The temperature dependent wavelength shift ($\Delta\lambda/\Delta T$) is 0.23 nm/K. With an AR-coating on the gain chip, $\Delta\lambda/\Delta T$ is closer to the value of quantum well shift rate (~0.3 nm/K) than that of an uncoated device because its microcavity resonance effect (with a shift rate of ~0.1 nm/K) is much weakened. The thermal impedance with respect to the dissipated power is calculated by the ratio of $\Delta\lambda/\Delta P$ to $\Delta\lambda/\Delta T$, which we estimate to be 3.1 K/W. In Chapter 3, we have estimated the thermal impedance with respect to the dissipated power of 1.2 K/W, showing reasonable agreement with the break-down of the incident pump power as follows: 39% of the pump power converts to heat, and 4% is reflected by the device surface. With 3% output coupling, the slope efficiency of the output power is 38%, meaning that 38% of the incremental pump power converts to the output power. Also, since we assume a passive loss of 1.4%, 18% of the incremental pump power becomes the loss in the cavity.

The optimum injection wavelength is calculated according to the free-running wavelength in Figure 4.16(b). For the injection-locking condition, the temperature of the gain medium is about 8.5°C lower and the wavelength shift is 2 nm shorter, which is consistent with the fact that the best injection-locking is observed with ~2 nm shorter wavelength than in the free running mode. By monitoring the temperature of the copper heat sink, we also observe the temperature rise of the injection-locked laser is lower compared to its free-running mode at a given pump power.

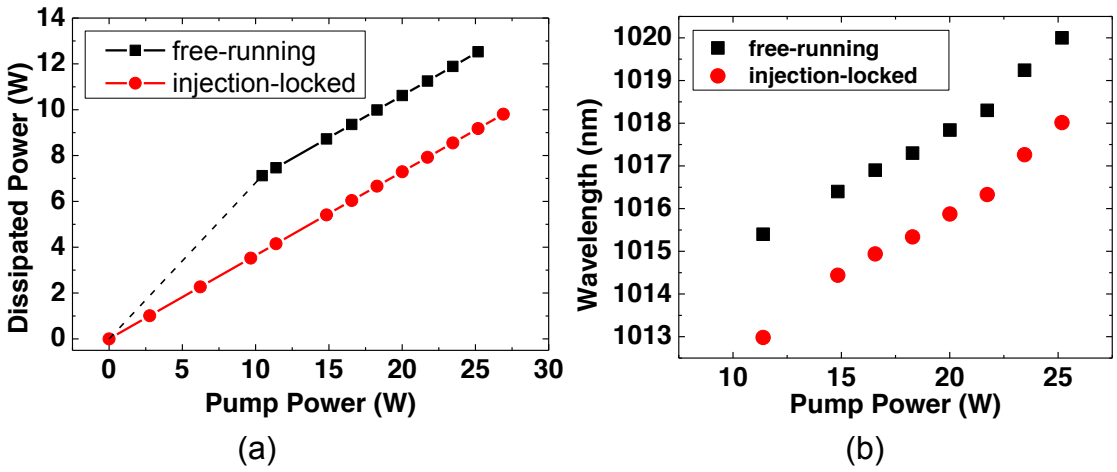

Figure 4.16 (a) Dissipated power calculation (b) The central emission wavelength of the free-running laser and the calculated optimum injection wavelength

4.7 Injection-locked laser operation at lower temperature

In order to extend the output performance of the laser, the output power of the injection-locked laser was recorded by decreasing the water temperature to 5^{o}C. The gain of the semiconductor material is temperature dependent, and it becomes higher at a lower temperature. Consequently, the laser lases at a lower pump threshold and higher output efficiency. In addition, the gain spectrum shifts to the shorter wavelength at lower temperature. Therefore, the thermal rollover is extended to a higher power level since the material gain and the microcavity are farther apart from each other and overlap at a higher pump power due to the difference in the shift rate. The maximum output power is approached using the same strategies as we did at 15^{o}C. By applying different injection wavelength, the optimum injection wavelength at 5^{o}C is found to be at 1015 nm (Figure 4.17), and the output power is enhanced with higher injection power up to 1.5 W (Figure 4.18).

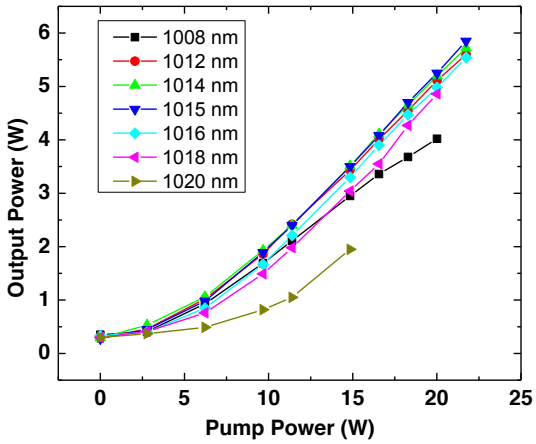

Figure 4.17 The output power as a function of total pump power for different injection wavelengths from 1008 nm to 1020 nm using 500 mW of injection power

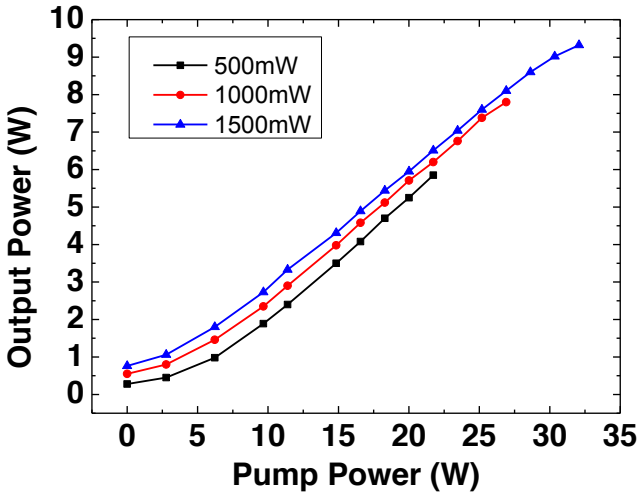

Figure 4.18 Output power enhancement by increasing the injection power to 1.5 W

The output power of the injection-locked laser and the free-running laser are compared in Figure 4.19. With 1.5 W of power from the master laser, the injection-locked laser generates over 9 W at 1015 nm, whereas the free-running laser rolls over with 6 W of output power. The maximum output power of the injection-locked laser is limited by the onset of parasitic oscillation, and it does not roll over. Besides, the spectral gain of the master laser is centered at 1015 nm, and the available output power of the master laser at longer wavelength is limited.

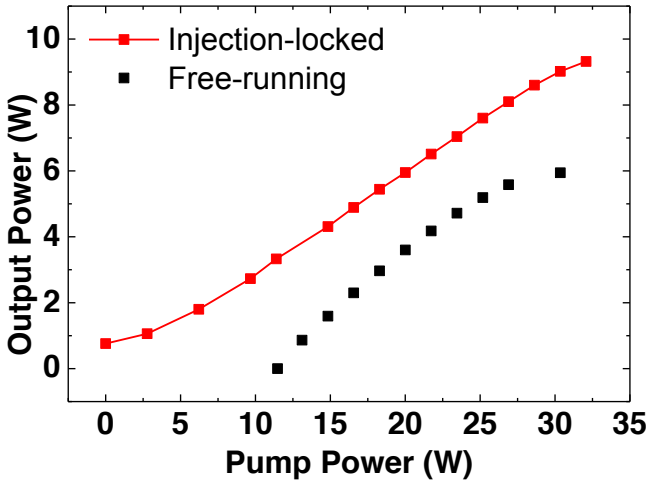

Figure 4.19 The output power comparison between Injection-locked laser and the free-running laser

4.8 Characteristic of the Pound-Drever error signal

When operating an injection-locked laser, it is useful to observe the error signal by sweeping the cavity length of the slave laser to make sure that the magnitude and the sign of the error signal is maintained adequately since the error signal is affected by the laser behavior at different pump levels. Figure 4.20 shows the error signal acquired from the oscilloscope using two output couplers, T = 3% and T = 4%. Both of the measurements were done under the same pump power of 20 W, but the amplitude of the locking signal near the carrier is attenuated by a variable ND filter so that it is always maintained at a fixed peak to peak voltage (~300 mV) for consistent locking. We observed different behaviors of the error signal between the conditions of using two output couplers.

At a low pump power level, the carrier and sideband signals are amplified at about the same rate as the pump power increases. However, with the T = 3% output coupler, if the pump power keeps increasing and internal power in the resonator keeps building up, the amplification of the carrier becomes saturated and the amplitude of sidebands grows more rapidly compared to the carrier signal as they are relatively weak and not saturated as much (Figure 4.20 (a)). This happens when the pump power goes beyond the lasing threshold of the free-running slave laser. On the other hand, we did not find the same effect by using the T = 4% output coupler, and the slave laser does not reach threshold in the free-running (Figure 4.20 (b)).

This difference in the error signal is caused by the gain saturation at the carrier. When the pump power is low, the gain to the carrier and the sidebands is practically the same since the gain bandwidth is much broader than 20 MHz, the frequency difference between the carrier and the sidebands. However, when the pump power is above the lasing threshold, the overall gain is clamped at the loss, which is equal to the output coupling loss plus the intracavity loss. When there is additional signal injected into the slave laser cavity, the cavity becomes resonant with the carrier, and the intracavity power builds up. This can momentarily drive the gain below the steady-state gain because the existence of the injection signal saturates the laser even more. The carrier starts to see the saturation of the gain due to the high circulating power in the cavity. As for the T = 4% case, the relatively low intracavity power leads to a lower degree of saturation even with the injection signal.

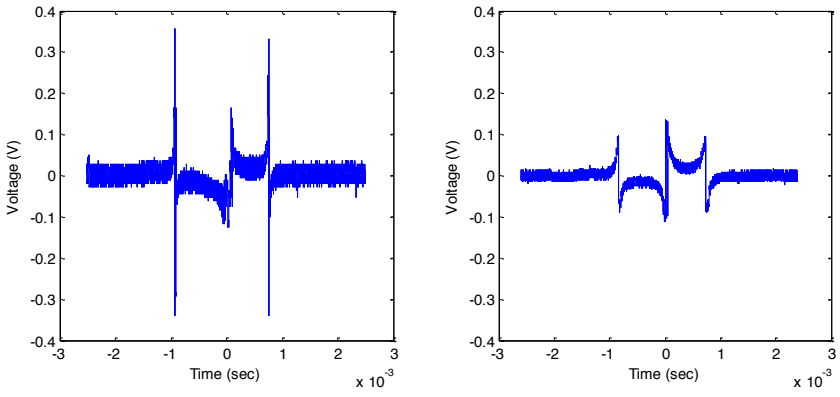

(a) (b)

Figure 4.20 The Error signal acquired from the oscilloscope by sweeping of the slave laser cavity using (a) T = 3% (b) T = 4% output coupler

4.9 M^2 measurement

The M^2 values of the free-running and the injection-locked laser were measured following by the method described in [123]. The output laser beam is focused by an f = 300 mm lens. The beam width is measured by a CCD-type beam profiler (Spiricon SP620U) along the beam propagation direction z. The beam width is defined by the second moment of the beam intensity distribution (D4σ width). The measured data points are fit with the equation:

$$W^2(z) = W_0^2 + M^4\left(\frac{\lambda}{\pi W_0}\right)^2 (z - z_0)^2 \tag{4.23}$$

where *W(z)* is the beam radius at an arbitrary point z, W_0 is the beam radius at the waist, z_o is the location of the beam waist. The M^2 values of the free-running slave laser are 1.08 and 1.04 for horizontal and vertical axes respectively (Figure 4.21). After injection-locking, the M^2 value of the injection-locked laser system are measured when the output power is 4 W in Figure 4.22, which are 1.04 and 1.02 along the horizontal and the vertical axis. The resulting beam profile of the injection locked laser remains nearly the same compared to the original profile of the free-running slave laser.

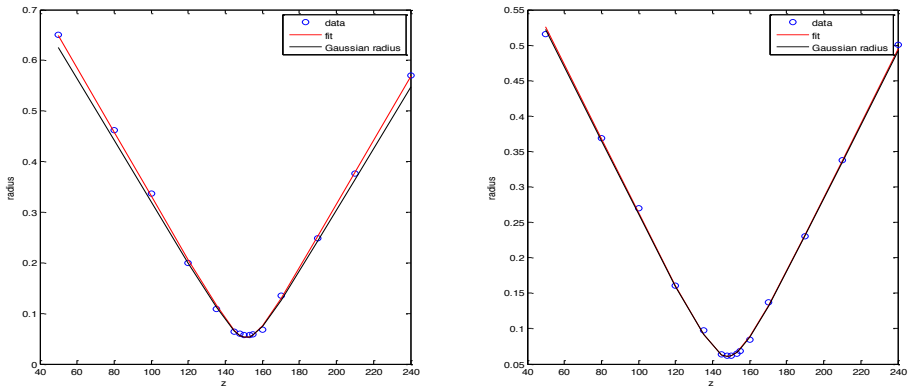

$M_x^2 = 1.075$ $M_y^2 = 1.042$

Figure 4.21 M^2 measurement of the free-running slave laser

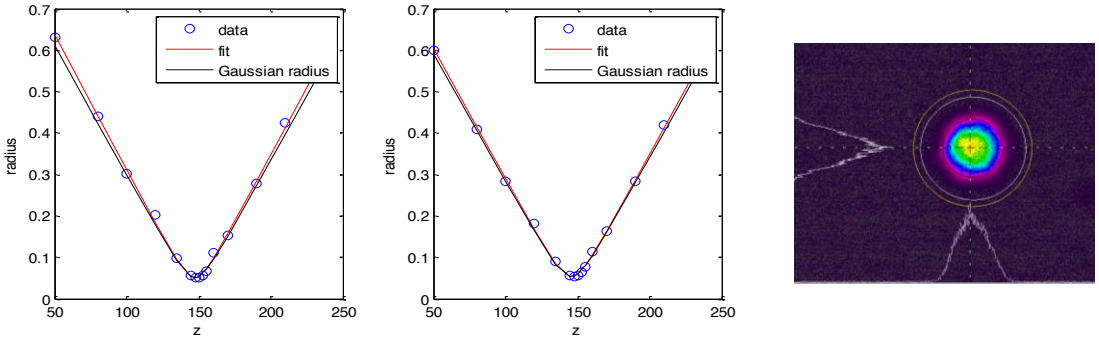

$M_x^2 = 1.04$ $M_y^2 = 1.02$

Figure 4.22 Left: M^2 measurement for the horizontal axis (M_x^2 =1.04) and the vertical axis (M_y^2 =1.02). Right: injection-locked laser output profile measured by a CCD profiler

4.10 Phase noise measurement

In the injection-locked laser system, the frequency stability is transferred from a narrow-linewidth laser (master) to a higher power laser (slave) whose spectral properties in free-running mode are not as good as the injected signal. The frequency and the phase of the two lasers are highly correlated after injection-locking. To assess the stability of a laser system, different methods such as homodyne detection, heterodyne scheme and self-heterodyne method are employed [124]. The homodyne detection is carried out by converting frequency fluctuations of the device under test (DUT) to power fluctuations with a discriminator, which is usually based on a Fabry-Perot interferometer or an absorption line of some molecules. The heterodyne scheme measures the noise via interference with a reference signal such as an auxiliary local oscillator or another similar laser. The self-heterodyne method [125] mixes the optical field with the delayed replica of itself. The delayed path is chosen to be longer than the coherence length of the laser so that the two beams are uncorrelated. All of the methods mention above use a fast photodetector to collect the signal and the noise information is further characterized by a spectral analyzer.

In our experiment, since the master laser is not actively frequency-stabilized, we compared the relative phase noise from the beat note between the master laser and the injection locked laser instead of measuring the absolute value of the phase noise. The purpose of this experiment is to show the injection-locked

laser does not add phase noise to that of the master laser, indicating that such an injection-locked OPSL can indeed be as narrow linewidth as the master laser. Figure 4.23 shows the schematic of the experiment. The beat note is formed between a portion of master laser power that is frequency-shifted by 80 MHz by an acousto-optic modulator (AOM) and the same amount of power of the injection-locked laser beam after attenuation. Two beams are combined and coupled to a single mode fiber that acted as a spatial filter before they are incident on the photodetector. Figure 4.24 shows the beat note measurements acquired by a spectrum analyzer (Signal Hound USB-SA44B) with a resolution bandwidth of 200Hz.

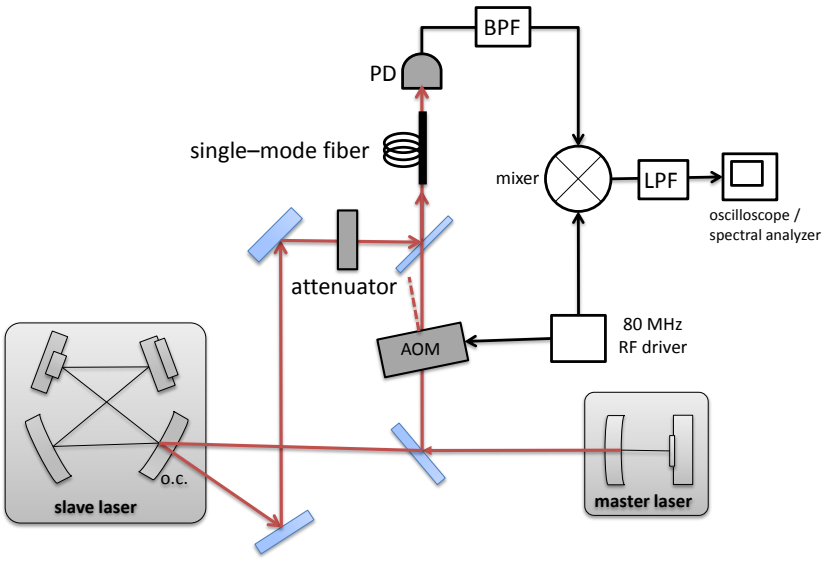

Figure 4.23 Schematic of beat phase noise measuring system

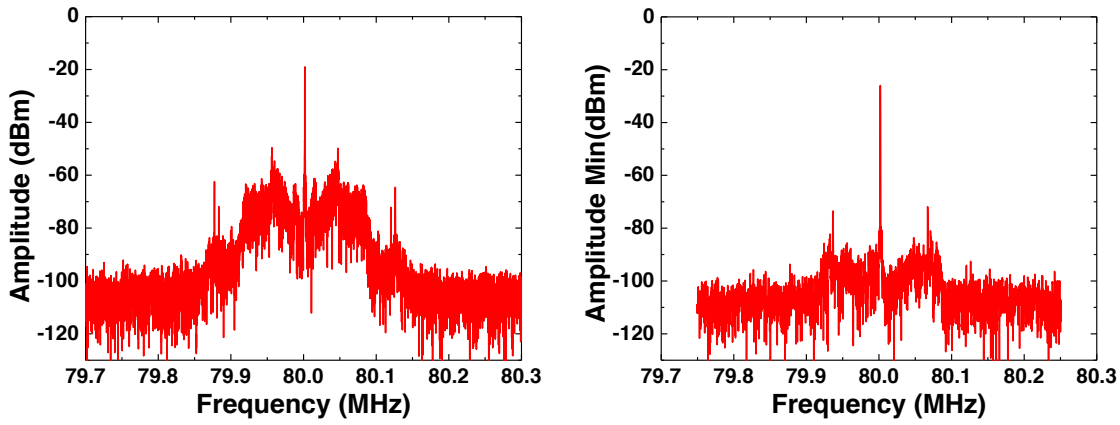

(a) (b)

Figure 4.24 Beat note measurement of the injection-locked laser using (a) T = 3% output coupler and (b) T = 4% output coupler

The beat signal is further demodulated by mixing with the local oscillator (LO, the driving signal for the frequency shifter) signal of the 80 MHz carrier frequency through a mixer to obtain the pure phase noise information. The signal received by the detector can be expressed as:

$$v \propto \left| E_m e^{i\varphi_m} + E_{inj} e^{i\varphi_{inj}} \right|^2 = E_m^2 + E_{inj}^2 + 2E_m E_{inj} \cos\left(\varphi_{inj} - \varphi_m\right) \tag{4.24}$$

where E represents the electric field amplitude and φ represents the phase; the subscripts m and inj denote the master laser and injection-locked laser. The phase difference is given by:

$$\Delta\varphi = \varphi_{inj} - \varphi_m = 2\pi\omega_m t + \phi(t) \tag{4.25}$$

where ω_m is the modulated frequency at 80 MHz. $\phi(t)$ is the phase noise that is added by the slave laser. A band pass filter is used before the mixer to filter out the DC and the high-frequency components. The signal after the mixer becomes:

$$v(t) \propto \mathrm{E}_m E_{inj} \left\{ \cos\left[2\omega_m t + \phi(t) \right] - \sin\left[\phi(t) \right] \right\} \tag{4.26}$$

The high frequency $2\omega_m$ is eliminated by a low pass filter. The resulting phase fluctuation signal is converted into power spectrum through Fourier transform. The phase fluctuation signal is calibrated with the maximum fluctuating range V_π. In practice, V_π can be obtained by tapping on one of the mirror mounts in the path and measuring the peak-to-peak voltage.

$$\phi(f) = \left[\frac{\pi}{V_\pi} \times V_{pp}(f) \right]^2 \quad \left(\text{unit: rad}^2 \right) \tag{4.27}$$

The power spectral density of the phase fluctuation signal is obtained by:

$$S_\phi(f) = \frac{\phi(f)^2}{RBW} \text{ (unit: rad}^2 \text{ / } Hz\text{)} \tag{4.28}$$

where RBW is the resolution bandwidth of the instrument.

The spectral density of the phase fluctuation signal is calculated by the following steps:

1. Acquire the signal with pure phase noise information from the oscilloscope

2. Fourier Transform:
   $v(t) \xrightarrow{F} V(f)$

$$amplitude_{one\text{-}sided} = \begin{cases} \sqrt{2}\dfrac{|V(f_i)|}{N},\ i = 2 \sim \dfrac{N}{2} \\ \dfrac{|V(f_i)|}{N},\ i = 1\ and\ \dfrac{N}{2}+1 \end{cases}$$

$$power_{one-sided} = \left(amplitude_{one-sided}\right)^2$$

3. Perturb the measurement setup to find the maximum fluctuation range V_π.

4. Covert power spectral density to phase spectral density
   $P(f) = \dfrac{V_{rms}(f)^2}{R} = \dfrac{V_{pp}(f)^2}{8R}$, where $R = 50\Omega$ (unit: Hz^2)
   $\phi(f)^2 = \left[\dfrac{\pi}{V_\pi} \times V_{pp}(f)\right]^2 = 8R \times P(f) \times \left(\dfrac{\pi}{V_\pi}\right)^2$ (unit: rad^2)
   $S_\phi(f) = \dfrac{\phi(f)^2}{RBW}$ (unit: rad^2 / *Hz*)

5. Repeat the above steps and average the data in frequency domain

The power spectral density of the phase fluctuation signal with 1 W of injection power from the master laser using T=3% and T= 4% is plotted in Figure 4.25 and Figure 4.26. The measurements were done on a 100 ms time scale with a resolution bandwidth of 7.6 Hz. The black line shows the noise floor of the laser system when the servo loop is open. The noise floor level remains the same whether the slave laser power is on or not, because the free running frequency of the slave laser is too far away from the modulation center to generate the beat signal and to be detectable. The detector is a silicon amplified detector (PDA10A,

Thorlabs) with 180 MHz bandwidth. With the T = 3% output coupler, S_ϕ from the injection-locking system rises from 10^{-10} rad^2/Hz to 10^{-7} rad^2/Hz around 20 kHz. On the other hand, there is very low added noise components with T = 4% output coupler. Given the fact that the slave laser lases in the free-running condition when using T = 3% output coupler, the excessive phase noise may come from the residual parasitic oscillation that is not detectable by either the OSA or the scanning Fabry-Perot interferometer. As for the case of T = 4%, there is no parasitic oscillation modes to bring in the noise. Therefore, the phase noise remains unaffected. The RMS value of the phase noise is obtained by:

$$\Delta\phi_{RMS} = \sqrt{\sum S_\phi(f) \cdot RBW} \quad (unit:\ rad) \tag{4.29}$$

The RMS values are 0.112 rad for T = 3% and 0.081 rad for T = 4%.

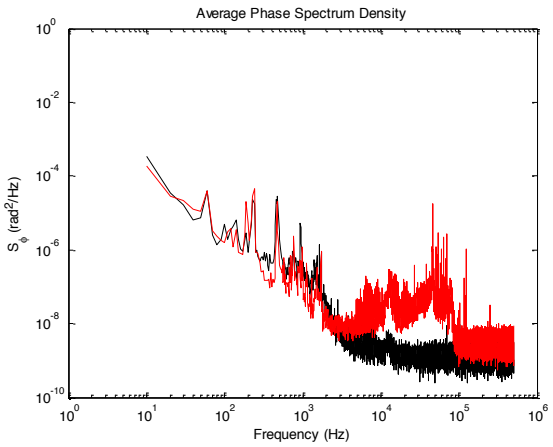

Figure 4.25 Phase noise calculation using T = 3% output coupler (red line). The black line shows the noise floor of the measuring system.

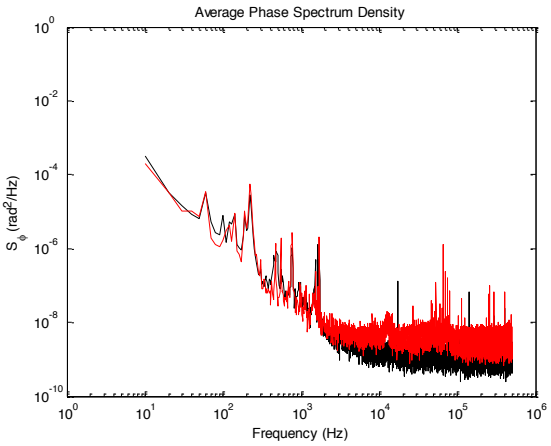

Figure 4.26 Phase noise calculation using T = 4% output coupler (red line). The black line shows the noise floor of the measuring system.

CHAPTER 5 CONCLUSION AND OUTLOOK

In this research, a single-frequency, continuous-wave, tunable wavelength, injecting-locked, optically-pumped semiconductor laser has been demonstrated for applications that require narrow linewidth operation at specific wavelengths such as atomic spectroscopy and laser cooling. The laser source is realized by implementing injection-locking of high power OPSLs to realize output power of several watts and higher with the same frequency stability of the master laser. To the best of our knowledge, the injection-locked operation of OPSL has been demonstrated for the first time.

There are several main contributions in the dissertation: firstly, besides the demonstration of new mode of operation, the optimum operating condition of the injection-locked OPSL has been investigated by varying the transmission of the output coupler, the injection wavelength and the injection power from the master laser. The maximum single-frequency injection-locked output power of 9 W at 1015 nm was experimentally obtained in near-diffraction-limited output beam with $M_x^2 = 1.04$ and $M_y^2 = 1.02$. Secondly, the laser gain properties such as the saturation intensity, the small signal gain and the cavity loss were estimated through the analysis and simulation of the output performance of the injection-locked laser and the surface PL of the OPSL device. The experimental results agree well with the simulation with the equivalent saturation intensity of

100 kW/cm^2 and approximated small signal gain. To the best of our knowledge, the steady-state gain saturation behavior of OPSL has not been reported before. This gives a guideline in laser engineering to allow better designs of laser systems using OPSL devices. Thirdly, the characteristics of the relative phase noise were examined to confirm the feasibility and the stability of the injection-locked OPSL. Some details are expressed in the following paragraphs.

The output characteristics of the laser were investigated using three output couplers with transmissions of 1%, 3% and 4%. The free-running laser reached threshold at lower pump power when the low transmission output coupler (1%) is used. However, under injection locked operation, the parasitic oscillation occurred at relatively low pump powers making injection-locking unstable and ineffective, hence the output did not reach very high power. When using the T = 3% output coupler, the injection-locked laser exhibited the best output efficiency, with its output power exceeding the sum of the injection power and free-running power of the slave laser. The slave laser did not lase with the T = 4% output coupler in the free-running mode; however, the laser acted as a resonant amplifier when injection-locked. This is a distinct feature of injection-locked laser with high saturation parameter, as it was revealed from the simulation.

The optimum wavelength for injection locked operation of the OPSL has been found to be slightly shorter than the free running wavelength of the slave

laser. In our experiment, it is around 2 nm shorter at a given pump power. We presume this is because the slave laser is locked to the master laser while injection-locking, and the injection-locked laser starts the stimulated emission process as soon as it is pumped. The radiative efficiency is higher when stimulated emission dominates in the carrier recombination process. With more extracted power, less heat is dissipated in the gain medium, and consequently the temperature rise becomes smaller compared to free running case. With the experimental parameters, the difference in temperature is estimated to be 8.5^{o}C. Hence, the shift rate of the gain peak is lower at a given pumping rate. The lower temperature shift of the injection-locked laser leads to the lower spectral shift of the gain spectrum and better output efficiency.

To extend the injection-locked output power, a higher injecting power is advantageous. By injecting 200 mW, 500 mW and 1 W from the master laser, the maximum output power was 3.6 W, 4.9 W and 6.5 W at 15^{0}C with the T = 3% output coupler. The output power was limited by the onset of parasitic oscillation. Due to relatively high saturation intensity and the larger mode area at the active region, higher power is needed from the master laser to maintain stable locking in comparison to other types of solid-state lasers. This is a profound difference from common injection-locked lasers like Nd:YAG. The calculated value of the saturation intensity is near 100 kW/cm^{2}, determined by analyzing the saturation behavior of the surface photoluminescence. Through the analysis of the laser

output power, we also obtained a consistent value of the saturation intensity of 100 kW/cm^2. The calculated results fit well with the experimental data.

We also evaluated the beat-note linewidth between the injection-locked laser and the master laser to assess the phase or frequency noise added by the slave laser. The phase spectral density rose from 10^{-10} rad^2/Hz to 10^{-7} rad^2/Hz around the frequency of 20 kHz when the T = 3% output coupler was used, whereas there was very low additional noise when transmission of the output coupler is 4%. The excessive phase noise of the T = 3% case may be caused by the existence of the free-running signal that is not detected by our observation. The RMS values of the phase noise from the beat note are 0.112 rad for T = 3% and 0.081 rad for T = 4%.

The goal of this study is to prove and to investigate the feasibility of applying the injection-locking technique on OPSLs for precision spectroscopy. The laser linewidth can supposedly be further narrowed if the master laser is frequency-stabilized. Besides using an OPSL as the master laser, other kinds of frequency-stabilized laser sources can be used, as long as the emission wavelength overlaps well with the gain bandwidth of the free-running slave laser. The injection-locked OPSL is particularly suitable for the application that requires a specific wavelength, which is not reachable by the conventional solid-state lasers. The emission wavelength of the OPSL can be manipulated through bandgap

engineering, giving accessibility to broad range of wavelengths, and hence opens opportunities for spectroscopic applications.

In this study, the injection-locked OPSL generated close to 10 W of output power at an unconventional wavelength while operating at a single frequency. Based on our experiment, the ratio between the injection power and the maximum output power is approximately 1/6. Depending on the requirement of the application, the output power of the injection-locked laser can be scaled up or down by adjusting the mode size of the slave laser cavity with a fixed pump to mode ratio. In the case where only several hundred mW to a couple watts of power is needed, a compact slave laser cavity with a smaller mode size can be used in combining with a lower injection power of several tens mW to a few hundred mW from the master laser. On the other hand, the injection-locking of OPSLs also provides the potential of developing a narrow-linewidth laser source with high output power. To achieve even higher output power, the first step is to improve the output performance of the slave laser. The improvement of the free-running slave laser includes the refinement of the OPSL chip design (e.g. larger detuning), thermal management and power scaling by the mode size of the slave resonator.

For the injection-locked laser system, there is no need to insert optical elements inside the slave laser cavity to ensure single mode operation, eliminating excess loss in the cavity, which is of critical importance particularly for

OPSLs because of its relatively small gain. Also, one may add nonlinear optical crystals into the slave laser cavity for the Intracavity nonlinear conversion. The cavity design can be straightforward without considering the loss of the mode selection elements.

As indicated above, this study represents significant contribution to the field of laser sources for spectroscopic applications wherein large amount of power in near diffraction-limited beam is needed in single frequency at a tailored wavelength.

APPENDIX A – Continuous-Wave OPSL Generation at 2-μm

The development of a mid-IR laser source around 2~3 μm is particularly important for applications such as free-space communication, remote sensing and gas detection since many gases have specific absorption lines in this wavelength range. The pulse operation of 2-μm emitting OPSL has been reported in ref [69] and [70]. In this report, a continuous-wave (CW) OPSL at 2 μm is demonstrated.

The OPSL device used in the experiment is a so-called the top-emitter. The GaSb/AlGaAsSb distributed Bragg reflector (DBR) is firstly grown on top of the GaSb substrate, followed by the quantum wells consisting of 9 pairs of InGaSb/AlGaSb layers. Figure A.1 shows the reflectivity spectra of the OPSL device at different heat-sink temperature from 40^{o}C to 100^{o}C. The dip is located at the wavelength where the QW absorption is enhanced by the microcavity resonance. As seen in Figure A.1, the QW absorption center aligns well with the microcavity resonance around 2000 nm. The reflection dip is located at the center of the DBR stop band, which ranges from 1850 nm to 2100 nm. The deepest dip occurs when the temperature is 80^{o}C, where the reflectivity is 46% at the wavelength of 2001 nm.

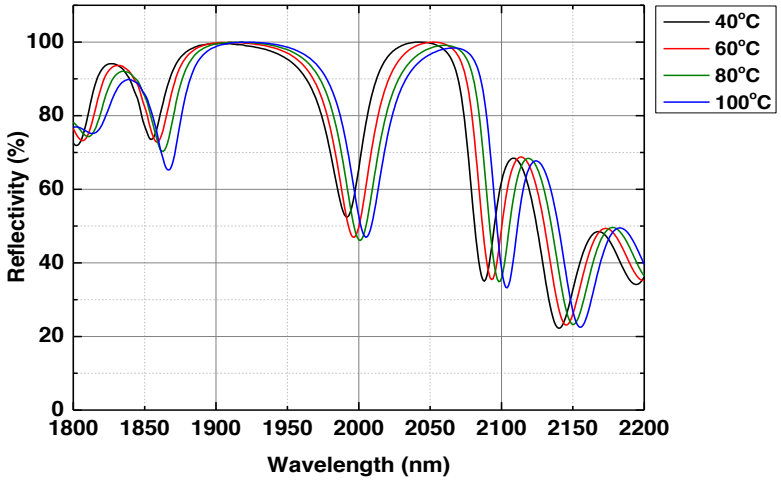

Figure A.1 Temperature dependent reflectivity (TDR) measurement at different temperatures.

The performance of OPSLs is sensitive to the temperature variation because the QW gain decreases as the temperature rises. Also, both the microcavity and the QW gain peaks shift to the red (but at different shift rates) when the temperature increases. The thermal management is crucial to minimize the temperature rise with pump power. Compared to a 1-μm emitting device, using the top heat spreader is preferred for the thermal management of a 2-μm emitting device since the thickness of the DBR of a 2-μm emitting device is larger than a 1-μm emitting device. A thicker DBR results in longer heat dissipation path from the center of the pumped area to the copper heat sink [63]. In addition, the thermal conductivity of GaSb (0.32 W/(m K)) is smaller compared to GaAs

(0.55 W/(m K)). Therefore, a top heat spreader can help removing the dissipated heat from the pumped area and distribute the heat to the surrounding region rapidly.

A disk-shaped, single crystalline CVD diamond manufactured by Element Six is used as the top heat spreader. The diamond disk is 4mm in diameter and 500 microns thick. The parallelism of the diamond was measured with an autocollimator to be 44 arcsec.

The device was lapped from the substrate side to a thickness of ~100 microns. A thinned device is advantageous not only in reducing the heat dissipation path to the copper mount but also in increasing the strength of capillary bonding. The bonding strength depends on the thickness of the wafer, material elasticity and the radius of curvature of the surface [60]. The thinned device was thoroughly cleaned with acetone and isopropyl alcohol (IPA) and was blown to dry with Nitrogen. The heat spreader diamond was also cleaned by the same process. Next, the thinned device was liquid-capillary bonded to the diamond. A drop of deionized water (DI water) was dropped on the diamond disk, and the thinned OPSL device was placed gently with the epi-side facing the diamond disk. The bonded device was placed horizontally and held still for water evaporation from the bonding edge until the interference pattern of the liquid thin film became fringeless (Figure A.2).

After the capillary bonding process is done, the bonded device was flipped and mounted in a copper mounting structure. As shown in Figure A.3, the copper mounting structure has a 3-mm aperture. The OPSL device is placed on a 1-mm thick copper disk, and the circulating water with fixed temperature flows below the copper disk to remove the heat from the water.

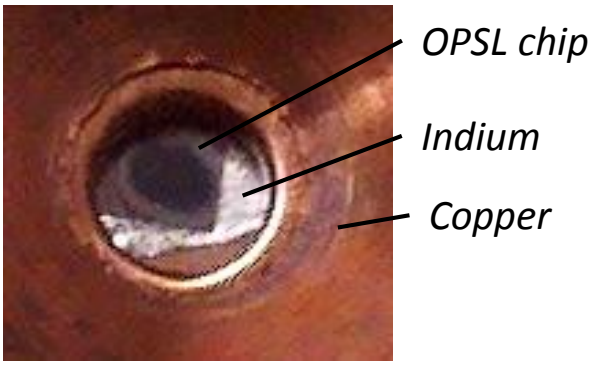

Figure A.2 The OPSL in the copper mount

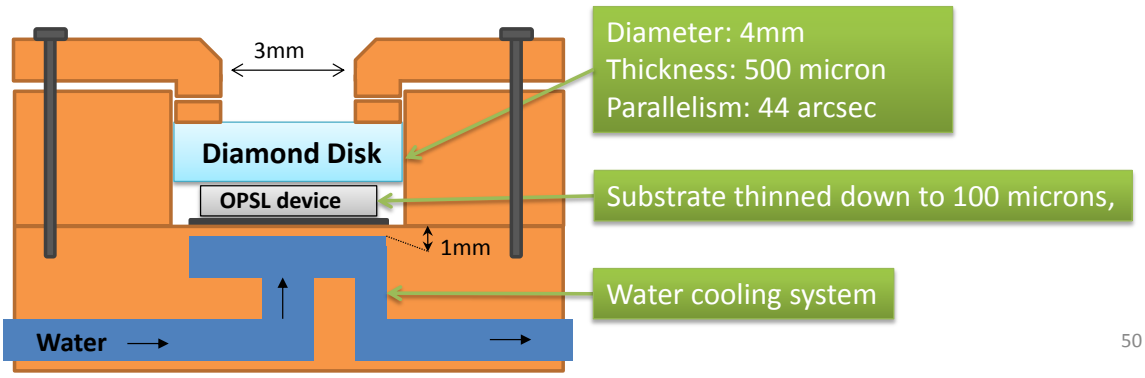

Figure A.3 The side-view of the OPSL in a heat dissipating system

The OPSL device is placed in a linear cavity such that the cavity length is 5 cm. The optical cavity is formed by the DBR of the OPSL device and a concave mirror with a radius of curvature of 100 mm. With this cavity configuration, the mode diameter at the chip surface is 357 microns. The device is pumped by a CW Nd:YAG laser emitting at 1064 nm with the Gaussian-profile pump diameter of 500 microns. The output power is investigated with three different output couplings, 2%, 4% and 6%. As shown in Figure A.4, when the output coupling is 4%, a maximum output of 2.9 watts is achieved at a temperature of 5^{o}C. When the pump diameter is 400 microns, a slightly higher output of 3 watts is obtained with the 4% output coupling. The power scaling is mainly limited by the bonding area of the top heat spreader and the OPSL device. Any local bump or particle on the OPSL device surface can affect the bonding quality, and thus restricts the maximum pump area. The emission wavelength shifts from 1998 nm to 2016 nm with increasing pump power.

The output performance of our OPSL is comparable with the experimental result in ref [66]. When the OPSL in ref [66] operates at a lower temperature of -15^{o}C and the pump power is retroreflected, a higher output power of 5 W was achieved.

In this report, we have demonstrated ~3 W of output power at 2 μm with an III-Sb based OPSL device. The output power may be improved when the thermal management is improved including a larger capillary bonding area for

power scaling and a lower operating temperature. On the other hand, for the applications that the single transverse mode operation is required, we can also redesign the cavity geometry by matching the pump and mode size at the highest available power.

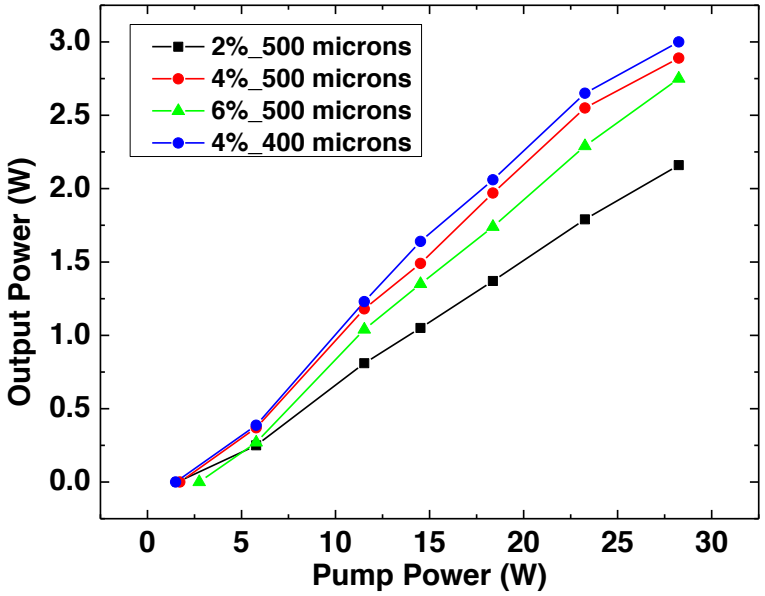

Figure A.4 Output power comparison using different output couplings (2%, 4% and 6%) and pump diameters (400 microns and 500 microns) at 5^{o}C

APPENDIX B – 340-W Peak Power From a GaSb 2-μm Optically Pumped Semiconductor Laser (OPSL) Grown Mismatched on GaAs

340-W Peak Power From a GaSb 2-μm Optically Pumped Semiconductor Laser (OPSL) Grown Mismatched on GaAs

Yi-Ying Lai, J. M. Yarborough, Yushi Kaneda, Jörg Hader, Jerome V. Moloney, T. J. Rotter, G. Balakrishnan, C. Hains, and S. W. Koch

***Abstract*—A GaSb-based vertical external cavity laser at 2 μm was pumped by 100- to 160-ns pulses from a Nd : YAG laser at 1.064 μm operating at 1 kHz. It was shown that the output power scales with the pump spot diameter to the extent of our experiments. A peak output of over 340 W was obtained.**

***Index Terms*—Gallium arsenide, laser cavity resonators, optical pumping, semiconductor lasers.**

I. Introduction

OPTICALLY pumped semiconductor disc lasers (OPSL), also known as vertical-external-cavity surface-emitting lasers (VECSELs), are promising devices for high output power generation in frequency ranges where other laser systems are relatively inefficient. Of particular interest is the emission in the wavelength range around 2 μm and longer since no high power sources are currently available in this regime. In this letter, we report record high output power near 2 μm using pulsed optical pumping in the 100-nanosecond (ns) range.

We used NLCSTR's SimuLase program [1] to design a suitable heterostructure which we then realized using molecular beam epitaxy (MBE) growth. The structure is nominally the same as the one investigated in [2]. It consists of a commercial $Al_{0.95}Ga_{0.05}As$–GaAs distributed Bragg reflector (DBR) with 25 repeats and an antimonide-based resonant periodic gain (RPG) region that is monolithically grown on the DBR via an interfacial misfit (IMF) dislocation array [3]. The IMF relaxes the strain due to the lattice mismatch at the GaSb–GaAs interface and eliminates the need for a thick metamorphic buffer to bridge the lattice mismatch between GaAs and GaSb. The resonant periodic gain (RPG) region consists of nine 13-nm-wide $In_{0.20}Ga_{0.80}Sb$ wells that are separated by pump absorbing $Al_{0.25}Ga_{0.75}Sb$ barriers. The device was designed to be operated in the continuous-wave (CW)-excitation mode [4], where the maximum output power is achieved at elevated device temperatures. Using the microscopic many-body calculations [1], the layer thicknesses and well compositions were chosen such that the gain maximum and cavity resonance should be aligned at the desired lasing wavelength of 2.0 μm at about 350 K.

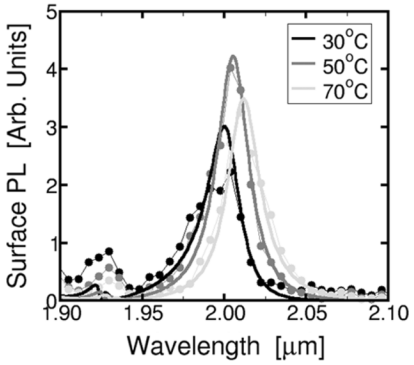

Fig. 1. Experimentally measured (thin lines, circles) and microscopically calculated (bold lines) surface-PL spectra at a fixed, low pump power for three temperatures.

II. Experiment

To characterize the actually grown structure and to check for possible deviations from the design, surface photoluminescence (PL) and reflectivity spectra were measured for various device temperatures. Fig. 1 shows a comparison between the measured PL and microscopically calculated spectra (see [5] for details about the analysis). Theory and experiment agree very well within the scattering of the experimental data. Both show the same temperature-dependent line-shapes, spectral shifts, and amplitudes. The maximum amplitude is found for about 50 °C. This indicates that for this temperature cavity resonance and quantum-well PL are in resonance.

In order to obtain the agreement between theory and experiment as shown in Fig. 1, we have to account for some minor deviations or the actually grown structure from the design. Most importantly, at 300 K the DBR stopband is centered around 2.05 μm instead of 2 μm indicating that the DBR layers are about 2.5% too thick. Overall, the deviations lead to a smaller detuning between cavity resonance and quantum-well absorption in the experimentally realized system. Thus, spectral alignment is achieved already at 323 K instead of the 350 K aimed for in the design.

Manuscript received March 29, 2010; revised May 22, 2010; accepted May 29, 2010. Date of current version July 23, 2010. This work was supported by a U.S. Joint Technology Office Multidisciplinary Research Initiative Program Grant AFOSR FA9550-07-1-0573.

Y.-Y. Lai, J. M. Yarborough, Y. Kaneda, and J. V. Moloney are with the College of Optical Sciences, University of Arizona, Tucson, AZ 85721 USA.

J. Hader is with Nonlinear Control Strategies Inc., Tucson, AZ 85705 USA.

T. J. Rotter, G. Balakrishnan, and C. Hains are with the Center for High Technology Materials, University of New Mexico, Albuquerque, NM 87106 USA.

S. W. Koch is with Material Science Center and Department of Physics, Philips Universität Marburg, 35032 Marburg, Germany.

Digital Object Identifier 10.1109/LPT.2010.2052596

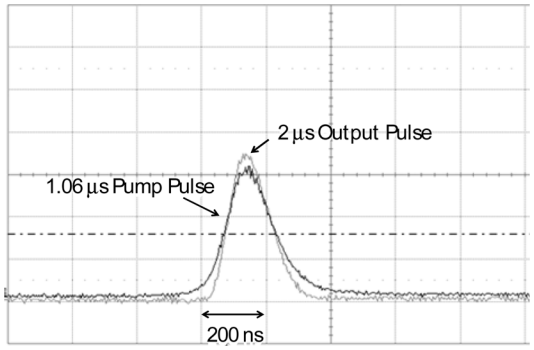

Fig. 2. Time resolved pump and 2-μm OPSL pulse shapes.

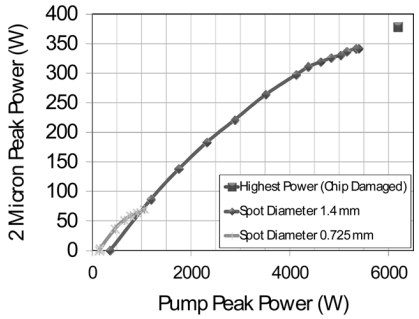

Fig. 3. Total incident versus output power characteristic for three different pump spot diameters.

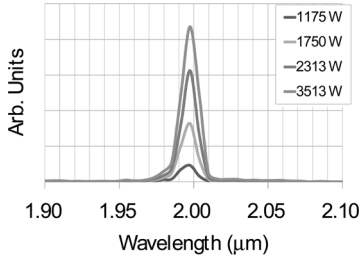

Fig. 4. Lasing spectra at various pump powers.

Since we study the device performance under pulsed pumping conditions, the small deviations between design and realized structure are of minor importance. The OPSL laser resonator is linear [2], consisting of the semiconductor chip and a 6%, 10-cm radius of curvature output coupler. The pump source is a diode-pumped Nd : YAG Q-switched laser cascaded with optical amplifiers. The repetition rate was fixed at 1 kHz. The pulsewidth and the power of the pump can be adjusted independently. The pulsewidth can be varied from several microseconds to 100 ns by changing the pump power for the oscillator. A positive lens with the focal length 12.5 cm was used to focus the 1.064-μm beam on the OPSL chip and to adjust the beam size with varied distance. The pump was incident at a small angle of incidence; 34.2% of the incident pump was lost by Fresnel reflection of the GaSb.

Since laser emission starts only after sufficiently high carrier density and thus optical round-trip gain is achieved during the pump pulse, we adjusted the cavity length to optimize the output peak power. When the cavity is shorter, the buildup time of the laser is shorter accordingly, and more of the pump pulse is converted to the 2-μm signal. This effect has been observed with cavity lengths varied from 7 to 2.5 cm. When the resonator length is changed, the resonator mode size also changes, but the change is negligible for the spacing we used. The 2-μm pulses appear earlier with a shorter cavity as observed on an oscilloscope. Fig. 2 shows the pulse shapes when the cavity length is 4.4 cm. It is clear that the 2-μm laser reached threshold very early in the pump pulse. There is no obvious improvement when the cavity is even shorter, but the 2-μm power was reduced as expected with longer cavity lengths.

Besides using a short cavity, a large beam diameter was used in order to operate at higher power without damaging the OPSL chip. Previously, we have demonstrated that the 2-μm output power saturated later with a larger pump beam size though the threshold was higher [2]. As shown in Fig. 3, the maximum OPSL power was observed when the beam diameter is 1.4 mm. Since the beam size is much larger than the fundamental cavity mode size, the 2-μm beam is highly multimode. We calculated the peak power by measuring the average power and dividing by the repetition rate and the pulsewidth at half maximum. The maximum peak power was 342 W with a 143-ns pulsewidth when the peak pump power was 5.5 kW with 160-ns pulsewidth. When the pump power was further increased, a maximum output peak power of 378 W was observed with approximately 6-kW pump power, where damage on the OPSL chip occurred. Compared to the previous result of 70-W OPSL peak power with 725-μm beam diameter, the power is improved by a factor of 5 while the area of the pump spot is about 5 times larger. To this extent, the results agree well with the power scaling law.

The time averaged emission spectra (Fig. 4) were measured using an infrared spectrometer having a spectral resolution of 15 nm (AvaSpec-NIR256-2.5, by Avantes Inc.). We observed a central wavelength around 1.998 μm that appears to be independent of the pump power. A similar experiment has been reported recently using also 100-ns-timescale pulsed excitation on a similar 2-μm OPSL [6]. In that experiment, a shift of the lasing wavelength during the pulse of about 16 nm has been observed. We estimate that the part of the pump-induced energy that is converted to heat between the maximum and the minimum powers in Fig. 4 would lead to a maximal temperature difference of about 37 K. This would be the case if all heating energy is distributed exclusively and homogeneously over the RPG region. From the surface-PL measurement (Fig. 1), we derive a wavelength shift of about 0.30 nm/K leading to a maximal shift of the lasing wavelength of about 11 nm. The shift of the average lasing wavelength measured here in the time-integrated setup should be somewhat less than that. We, therefore, assume that the lasing wavelength is not pump-power-independent, but merely below the resolution of our spectrometer.

III. Conclusion

In summary, we obtained a peak output power over 340 W under $\sim$100-ns pulsed pumping conditions, observing almost perfect power scaling for pump diameters up to 1.4 mm.

REFERENCES

[1] SimuLase software. Nonlinear Control Strategies Inc., Tucson, AZ.

[2] J. M. Yarborough, Y.-Y. Lai, Y. Kaneda, J. Hader, J. V. Moloney, T. J. Rotter, G. Balakrishnan, C. Hains, D. Huffaker, and S. W. Koch, "Record pulsed power demonstration of a 2 μm GaSb-based optically pumped semiconductor laser grown lattice-mismatched on an AlAs/GaAs Bragg mirror and substrate," *Appl. Phys. Lett.*, vol. 95, p. 081112, 2009.

[3] S. H. Huang, G. Balakrishnan, A. Khoshakhlagh, A. Jallipalli, L. R. Dawson, and D. L. Huffaker, "Strain relief by periodic misfit arrays for low defect density GaSb on GaAs," *Appl. Phys. Lett.*, vol. 88, p. 131911, 2006.

[4] T. J. Rotter, J. Tatebayashi, P. Senanayake, G. Balakrishnan, M. Rattunde, J. Wagner, J. Hader, J. V. Moloney, S. W. Koch, L. R. Dawson, and D. L. Huffaker, "Continuous-wave, room-temperature operation of 2-μm Sb-based optically-pumped vertical-external-cavity surface-emitting laser monolithically grown on GaAs substrates," *Appl. Phys. Express*, vol. 2, p. 112102, 2009.

[5] J. Hader, G. Hardesty, T.-L. Wang, M. J. Yarborough, Y. Kaneda, J. V. Moloney, B. Kunert, W. Stolz, and S. W. Koch, "Predictive microscopic modeling of VECSELs," *IEEE J. Quantum Electron.*, vol. 46, no. 5, pp. 810–817, May 2010.

[6] N. Hempler, J. M. Hopkins, A. J. Kemp, M. Schulz, M. Rattunde, J. Wagner, M. D. Dawson, and D. Burns, "Pulsed pumping of semiconductor disk lasers," *Opt. Express*, vol. 15, p. 3247, 2007.

APPENDIX C – Record pulsed power demonstration of a 2-μm GaSb-based optically pumped semiconductor laser grown lattice-mismatched on an AlAs/GaAs Bragg mirror and substrate

Record pulsed power demonstration of a 2 μm GaSb-based optically pumped semiconductor laser grown lattice-mismatched on an AlAs/GaAs Bragg mirror and substrate

J. M. Yarborough,[1,a)] Yi-Ying Lai (賴奕穎),[1] Yushi Kaneda (金田有史),[1] Jörg Hader,[1,2] Jerome V. Moloney,[1,2] T. J. Rotter,[3] G. Balakrishnan,[3] C. Hains,[3] D. Huffaker,[4] S. W. Koch,[5] and R. Bedford[6]

[1]*College of Optical Sciences, University of Arizona, Tucson, Arizona 85721, USA*
[2]*Nonlinear Control Strategies Inc, 3542 N Geronimo Ave., Tucson, Arizona 85704, USA*
[3]*Center for High Technology Materials, University of New Mexico, Albuquerque, New Mexico 87106, USA*
[4]*Department of Electrical and Computer Engineering, University of California, Los Angeles, California 90095, USA*
[5]*Department of Physics, University of Marburg, Renthof 5, 35032 Marburg, Germany*
[6]*Air Force Research Laboratory, Sensors Directorate, Wright Patterson AFB, Ohio 45433, USA*

(Received 9 July 2009; accepted 5 August 2009; published online 27 August 2009)

An optically pumped semiconductor laser resonant periodic gain structure, grown lattice-mismatched on an AlAs/GaAs Bragg mirror, exhibits a peak pulsed power of 70 W when pumped with a pulsed 1064 nm neodymium doped yttrium aluminum garnet laser. © *2009 American Institute of Physics*. [DOI: 10.1063/1.3212891]

Optically pumped semiconductor disk lasers (OPSL) or, equivalently, vertical external cavity surface emitting semiconductor lasers (VECSEL), are emerging as novel sources of high-power, high brightness IR, mid-IR, visible, and UV light. Record powers up to 30 W in an essentially TEM_{00} have been demonstrated in the IR band by Coherent.[1] Using intracavity second harmonic generation, spectrally narrow multiwatt outputs have been demonstrated at green[2] and yellow-orange[3] wavelengths in TEM_{00} beams. Direct generation of red light at 670 nm with powers close to 0.5 W has also been demonstrated.[4] These VECSEL structures were grown using InGaAs or InGaPAs quantum well (QW) stacks grown on AlGaAs/AlAs Bragg mirrors. Extension of these structures to the mid-IR, requires growth of InGaSb QW stacks on AlGaSb/GaSb Bragg mirrors. The latter have been employed to demonstrate 3–5 W VECSEL lasing between 2 and 2.3 μm.[5] Two fundamentally different wafer growth modes have been employed in all cases. The most common approach is to grow the distributed Bragg reflector (DBR) stack directly on the substrate (GaAs or GaSb) followed by growth of the resonant periodic gain (RPG) QW stack.[6] Thermal management of these devices requires that a transparent SiC or single crystal diamond intracavity heat spreader be bonded directly to the top epitaxial surface. An alternative approach that has demonstrated the highest powers to date is to grow the RPG multi-QW stack directly on a GaAs substrate, followed by the DBR.[7] This approach requires that the GaAs substrate be completely etched away after mounting on a chemical vapor deposition (CVD) diamond heat spreader. The resulting semiconductor microcavity consisting of RPG gain section and DBR is extremely thin and can be cooled directly from the bottom of the chip.

In this letter, we introduce a growth method not previously used and demonstrate a peak pulsed power of 70 W at 2 μm. Our goal is to retain the AlGaAs/GaAs DBR and GaAs substrate but to grow an antimonide RPG stack consisting of InGaSb quantum wells embedded in AlGaSb barriers on the latter structure. The AlGaAs/GaAs DBR is grown independently on a GaAs substrate using a metal oxide CVD reactor. This mirror structure is loaded in a molecular beam epitaxy (MBE) reactor and the final RPG gain section is grown next using an interfacial misfit array (IMF) technique[8] to offset the lattice mismatch. Details of the growth and wafer characterization will be published elsewhere. We chose this route because of the lower thermal impedance of the AlGaAs/GaAs mirror relative to an AlGaSb/GaSb mirror and our recent observation from spectroscopic studies show that bulk GaSb exhibits evidence for deep-level defects, that can act as significant loss sites around 2–2.5 μm. The entire VECSEL subcavity was designed using a rigorous microscopic physics model for the active RPG structure and growths were validated against a software tool based on the latter model.[9]

This OPSL/VECSEL structure, with a III-Sb active region grown on AlGaAs/GaAs DBRs without the use of thick metamorphic buffers, is a different design than any previous structures. The effective lattice mismatch of 7.78% between the DBR and the active region is accommodated by the IMF growth mode. The complexities involved in the growth of such a structure are significant and hence we have chosen to pump the laser at subthermal levels using pulsed pumping instead of continuous pumping which would require additional processing for thermal management schemes. We carried out full spectroscopic analysis of the grown structure and compared measured room temperature OPSL chip reflectance, edge and surface photoluminescence (PL) spectra against the microscopically calculated designs. (PL peak location and intensity were sensitive to growth temperature and Sb flux in the MBE reactor.) The measured data showed good agreement with the designs but the chips were expected to lase under subthermal pulsed conditions, so we used a pulsed neodymium doped yttrium aluminum garnet (Nd:YAG) laser at 1064 nm for the pump source. The pulse lengths were typically 300 ns, and the duty cycle was kept very low to avoid heating as much as possible. (Since the

a)Electronic mail: myarborough@optics.arizona.edu.

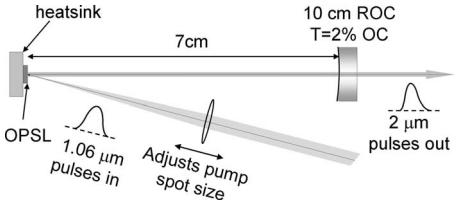

FIG. 1. OPSL schematic layout.

OPSL's active quantum wells were on top of the substrate, which is a poor heat conductor.)

Figure 1 shows the experimental arrangement. The pump laser is a diode-pumped Nd:YAG laser that is continuously pumped and repetitively Q-switched by an acousto-optic Q-switch. The repetition rate of the laser is 1 kHz, and typical pulse lengths are 300 ns, with peak power variable between 0 and 1.2 kW. Pulse energies varied between 0 and 0.4 mJ, and typical average pump power was 200 mW. The laser beam was focused by means of a 12.5 cm focal length lens onto the OPSL chip under test. The pump beam was nominally TEM_{00}. A linear cavity was used for the OPSL laser. Two different OPSL chips from the same wafer were evaluated. One chip was antireflection (AR) coated at the lasing wavelength of 2 μm, and the other was uncoated. A 2% transmitting, 10 cm radius of curvature output mirror was used for the AR coated chip, and a 4% transmitting, 10 cm radius mirror was used for the uncoated chip. In both cases, the output mirror was spaced 7 cm from the OPSL chip, giving a fundamental mode radius of 178 μm at the lasing wavelength of 2 μm. The diameter of the pump spot was varied by varying the spacing between the lens and the OPSL chip. For the highest power experiments, the pump spot size was much larger than the OPSL fundamental mode size, and the output was thus highly multimode.

Figure 2 shows the peak output power at 2 μm for the two OPSL chips. The AR coated chip was operated with the pump spot size matched to the resonator mode and also with a much larger pump spot size. For the smaller spot size of approximately 350 μm, which was approximately matched to the resonator mode, the threshold was lowest, at about 19 W. The initial slope efficiency is around 15%, but the output power saturates at 8 W due to lack of cooling. The other curve for the AR coated chip is for a pump spot size of 725 μm, which is about twice as large, hence the pump area is four times as large. The measured threshold for the smaller

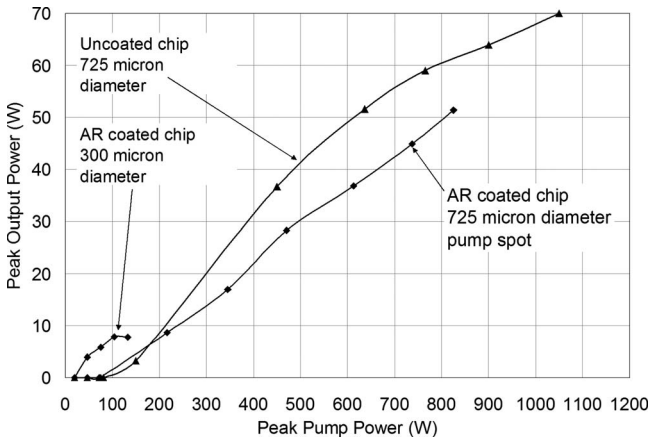

FIG. 2. 2 μm OPSL peak output power.

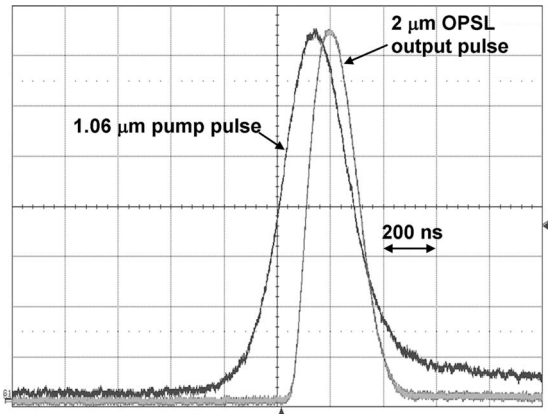

FIG. 3. Pump and OPSL pulse shapes.

pump spot size is 19.5 W, while the measured threshold for the larger pump spot is 72 W due to the larger pump spot size. The ratio of thresholds is approximately the ratio of the pump spot areas. We observed some damage at the highest pump power for this chip. Due to the larger pump spot area in the second case the OPSL runs on multiple lateral modes. The third curve is for the uncoated chip. In this case, the microcavity resonance between the DBR and the uncoated chip surface forms a resonant structure that increases the internal electric field and hence gives greater gain. We found a 4% mirror gave higher output in this case, and maximum peak power is 70 W. The saturation at high powers is due to the fact that as we increased the pump power, the pump pulse length became shorter, and the OPSL buildup time became a factor.

Figure 3 shows the temporal pulse shapes of the pump and the 2 μm OPSL output under typical operating conditions. The pump was measured with a fast silicon photodiode and the OPSL with an InGaAs detector. The pump pulse is essentially Gaussian shaped temporally. The pump peak power was calculated by measuring the average power of the pump and dividing by the repetition rate and the pulse width at half-maximum. The OPSL turns on near the peak on the leading edge of the pump pulse. The threshold pump power was calculated by turning the pump power down until the OPSL just oscillated and calculating the pump power as above. This gives a pessimistic estimate of the pump power, since the actual threshold had to occur before the peak due to build up time in the OPSL resonator. The OPSL output power was also calculated by measuring the average power and the pulse length.

The spectrum of the OPSL was measured with an infrared spectrometer and the spectrum consisted of a single peak at 1995 nm, very near the design wavelength of 2.0 μm.

In conclusion, we have designed a near infrared OPSL with an antimonide-based resonant periodic gain structure grown lattice mismatched on a AlAs/GaAs Bragg mirror, grown samples, and evaluated them under pulsed conditions. The 70 Watt peak output at 2 μm is the highest reported power to date from a near infrared OPSL.

This work was funded by a U.S. Joint Technology Office Multidisciplinary Research Initiative Program Grant No. AFOSR FA9550-07-1-0573.

[1]J. Chilla, Q. Shu, H. Zhou, E. Weiss, M. Reed, and L. Spinelle, Proc. SPIE **6451**, 645109 (2007).
[2]L. Hunziker, Q. Shu, H. Zhou, D. Bauer, C. Ihli, G. Mahnke, M. Rebut, J. Chilla, A. Caprara, H. Zhou, E. Weill, and M. Reed, Proc. SPIE **6451**, 64510A (2007).
[3]M. Fallahi, L. Fan, Y. Kaneda, C. Hessenius, J. Hader, H. Li, J. V. Moloney, B. Dunert, W. Stolz, S. W. Koch, J. Murray, and R. Bedford, IEEE Photonics Technol. Lett. **20**, 1700 (2008).
[4]J. E. Hastie, S. Calvez, M. Dawson, T. Leinonen, A. Laakso, J. Lyytikainen, and M. Pessa, Opt. Express **13**, 77 (2005).
[5]J. M. Hopkins, N. Hempler, B. Rosener, N. Schulz, M. Rattunde, C. Manz, K. Kohler, J. Wagner, and D. Burns, Opt. Lett. **33**, 201 (2008).
[6]J. V. Sandusky and S. R. J. Brueck, IEEE Photonics Technol. Lett. **8**, 313 (1996).
[7]M. Kuznetsov, F. Hakimi, R. Sprague, and A. Mooradian, IEEE Photonics Technol. Lett. **9**, 1063 (1997).
[8]S. H. Huang, G. Balakrishnan, A. Khoshakhlagh, A. Jallipalli, L. R. Dawson, and D. L. Huffaker, Appl. Phys. Lett. **88**, 131911 (2006).
[9]SimuLase, from Nonlinear Control Strategies, Tucson, AZ.

REFERENCES

[1] M. Kuznetsov, *VECSEL Semiconductor Lasers : A Path to High-Power , Quality Beam and UV to IR Wavelength by Design*. 2010.

[2] A. C. Tropper and S. Hoogland, “Extended cavity surface-emitting semiconductor lasers,” *Prog. Quantum Electron.*, vol. 30, no. 1, pp. 1–43, Jan. 2006.

[3] R. Debusmann, N. Dhidah, V. Hoffmann, L. Weixelbaum, U. Brauch, T. Graf, M. Weyers, and M. Kneissl, “InGaN–GaN Disk Laser for Blue-Violet Emission Wavelengths,” *IEEE Photonics Technol. Lett.*, vol. 22, no. 9, pp. 652–654, May 2010.

[4] S.-H. Park, J. Kim, H. Jeon, T. Sakong, S.-N. Lee, S. Chae, Y. Park, C.-H. Jeong, G.-Y. Yeom, and Y.-H. Cho, “Room-temperature GaN vertical-cavity surface-emitting laser operation in an extended cavity scheme,” *Appl. Phys. Lett.*, vol. 83, no. 11, p. 2121, 2003.

[5] J. Hastie, S. Calvez, M. Dawson, T. Leinonen, A. Laakso, J. Lyytikäinen, and M. Pessa, “High power CW red VECSEL with linearly polarized TEM00 output beam.,” *Opt. Express*, vol. 13, no. 1, pp. 77–81, Jan. 2005.

[6] M. Rahim, F. Felder, M. Fill, and H. Zogg, “Optically pumped 5 μm IV-VI VECSEL with Al-heat spreader,” *Opt. Lett.*, vol. 33, no. 24, p. 3010, Dec. 2008.

[7] M. Rahim, M. Fill, F. Felder, D. Chappuis, M. Corda, and H. Zogg, “Mid-infrared PbTe vertical external cavity surface emitting laser on Si-substrate with above 1 W output power,” *Appl. Phys. Lett.*, vol. 95, no. 24, p. 241107, 2009.

[8] Y. Kaneda, J. M. Yarborough, L. Li, N. Peyghambarian, L. Fan, C. Hessenius, M. Fallahi, J. Hader, J. V Moloney, Y. Honda, M. Nishioka, Y. Shimizu, K. Miyazono, H. Shimatani, M. Yoshimura, Y. Mori, Y. Kitaoka, and T. Sasaki, “Continuous-wave all-solid-state 244 nm deep-ultraviolet laser source by fourth-harmonic generation of an optically pumped semiconductor laser using CsLiB_6O_10 in an external resonator,” *Opt. Lett.*, vol. 33, no. 15, p. 1705, Jul. 2008.

[9] T.-L. Wang, Y. Kaneda, J. Hader, J. V. Moloney, B. Kunert, W. Stolz, and S. W. Koch, “Strategies for power scaling VECSELs,” in *Proceedings of SPIE*, 2012, vol. 8242, p. 824209.

[10] J. V. Moloney, J. Hader, T.-L. Wang, Y. Ying, Y. Kaneda, J. M. Yarborough, T. J. Rotter, G. Balakrishnan, C. Hains, S. W. Koch, W. Stolz, B. Kunert, and R. Bedford, “Power Scaling of CW and Pulsed IR and mid-IR OPSLs,” in *Proceedings of SPIE*, 2011, vol. 7919, p. 79190S–1.

[11] B. Heinen, T.-L. Wang, M. Sparenberg, A. Weber, B. Kunert, J. Hader, S. W. Koch, J. V. Moloney, M. Koch, and W. Stolz, “106 W continuous-wave output power from vertical-external-cavity surface-emitting laser,” *Electron. Lett.*, vol. 48, no. 9, p. 516, 2012.

[12] L. E. Hunziker, Q.-Z. Shu, D. Bauer, C. Ihli, G. J. Mahnke, M. Rebut, J. R. Chilla, A. L. Caprara, H. Zhou, E. S. Weiss, and M. K. Reed, “Power-scaling of optically-pumped semiconductor lasers,” in *Proceedings of SPIE*, 2007, vol. 6451, p. 64510A–64510A–6.

[13] F. Zhang, B. Heinen, M. Wichmann, C. Möller, B. Kunert, A. Rahimi-Iman, W. Stolz, and M. Koch, “A 23-watt single-frequency vertical-external-cavity surface-emitting laser.,” *Opt. Express*, vol. 22, no. 11, pp. 12817–22, Jun. 2014.

[14] A. Laurain, C. Mart, J. Hader, J. V. Moloney, B. Kunert, and W. Stolz, “15 W Single Frequency Optically Pumped Semiconductor Laser With Sub-Megahertz Linewidth,” *IEEE Photonics Technol. Lett.*, vol. 26, no. 2, pp. 131–133, Jan. 2014.

[15] R. Hall, G. Fenner, J. Kingsley, T. Soltys, and R. Carlson, “Coherent Light Emission From GaAs Junctions,” *Phys. Rev. Lett.*, vol. 9, no. 9, pp. 366–368, Nov. 1962.

[16] M. I. Nathan, W. P. Dumke, G. Burns, F. H. Dill, and G. Lasher, “STIMULATED EMISSION OF RADIATION FROM GaAs p-n JUNCTIONS,” *Appl. Phys. Lett.*, vol. 1, no. 3, p. 62, 1962.

[17] N. Holonyak and S. F. Bevacqua, “COHERENT (VISIBLE) LIGHT EMISSION FROM Ga(As1−xPx) JUNCTIONS,” *Appl. Phys. Lett.*, vol. 1, no. 4, p. 82, 1962.

[18] T. M. Quist, R. H. Rediker, R. J. Keyes, W. E. Krag, B. Lax, a. L. McWhorter, and H. J. Zeigler, “SEMICONDUCTOR MASER OF GaAs,” *Appl. Phys. Lett.*, vol. 1, no. 4, p. 91, 1962.

[19] I. Hayashi, “Junction Lasers Which Operate Continuously At Room Temperature,” *Appl. Phys. Lett.*, vol. 17, no. 3, p. 109, 1970.

[20] H. Nelson, “Liquid-phase epitaxy — Its role in crystal growth technology,” *J. Cryst. Growth*, vol. 27, no. May, pp. 1–5, Dec. 1974.

[21] D. F. Welch and S. Member, “A Brief History of High-Power Semiconductor Lasers,” vol. 6, no. 6, pp. 1470–1477, 2000.

[22] J. P. van der Ziel, R. Dingle, R. C. Miller, W. Wiegmann, and W. a. Nordland, “Laser oscillation from quantum states in very thin GaAs−Al0.2Ga0.8As multilayer structures,” *Appl. Phys. Lett.*, vol. 26, no. 8, p. 463, 1975.

[23] R. Dingle and C. H. Henry, “QUANTUM EFFECTS IN HETEROSTRUCTURE LASERS,” U.S. Patent #3982207,1976.

[24] Y. Arakawa, “Multidimensional quantum well laser and temperature dependence of its threshold current,” *Appl. Phys. Lett.*, vol. 40, no. 11, p. 939, 1982.

[25] C. H. Henry, P. M. Petroff, R. a. Logan, and F. R. Merritt, “Catastrophic damage of AlxGa1−xAs double-heterostructure laser material,” *J. Appl. Phys.*, vol. 50, no. 5, p. 3721, 1979.

[26] R. Diehl, Ed., *High-Power Diode Lasers*, vol. 78. Berlin, Heidelberg: Springer Berlin Heidelberg, 2000.

[27] A. Mooradian, “High brightness cavity-controlled surface emitting GaInAs lasers operating at 980 nm,” in *Optical Fiber Communication Conference and Exhibit. Technical Digest Postconference Edition (IEEE Cat. 01CH37171)*, 2001, vol. 4, pp. PD17–P1–3.

[28] W. B. Jiang, S. R. Friberg, H. Iwamura, and Y. Yamamoto, “High powers and subpicosecond pulses from an external-cavity surface-emitting InGaAs/InP multiple quantum well laser,” *Appl. Phys. Lett.*, vol. 58, no. 8, p. 807, 1991.

[29] J. V. Sandusky and S. R. J. Brueck, “A CW external-cavity surface-emitting laser,” *IEEE Photonics Technol. Lett.*, vol. 8, no. 3, pp. 313–315, Mar. 1996.

[30] M. Kuznetsov, F. Hakimi, R. Sprague, and A. Mooradian, “Design and characteristics of high-power (>0.5-W CW) diode-pumped vertical-external-cavity surface-emitting semiconductor lasers with circular TEM/sub 00/

beams," *IEEE J. Sel. Top. Quantum Electron.*, vol. 5, no. 3, pp. 561–573, 1999.

[31] J. J. Zayhowski and A. Mooradian, "Single-frequency microchip Nd lasers," *Opt. Lett.*, vol. 14, no. 1, p. 24, Jan. 1989.

[32] A. Giesen, H. Hiigep, A. Voss, K. Wittig, U. Brauch, and H. Opower, "Scalable Concept for Diode-Pumped High-Power Solid-State Lasers," vol. 372, pp. 365–372, 1994.

[33] A. Giesen and J. Speiser, "Fifteen Years of Work on Thin-Disk Lasers: Results and Scaling Laws," *IEEE J. Sel. Top. Quantum Electron.*, vol. 13, no. 3, pp. 598–609, 2007.

[34] U. Keller and A. C. Tropper, "Passively modelocked surface-emitting semiconductor lasers," *Phys. Rep.*, vol. 429, no. 2, pp. 67–120, Jun. 2006.

[35] T. D. Raymond, W. J. Alford, M. H. Crawford, and a a Allerman, "Intracavity frequency doubling of a diode-pumped external-cavity surface-emitting semiconductor laser.," *Opt. Lett.*, vol. 24, no. 16, pp. 1127–9, Aug. 1999.

[36] M. Scheller, J. M. Yarborough, J. V Moloney, M. Fallahi, M. Koch, and S. W. Koch, "Room temperature continuous wave milliwatt terahertz source.," *Opt. Express*, vol. 18, no. 26, pp. 27112–7, Dec. 2010.

[37] M. A. Holm, D. Burns, A. I. Ferguson, and M. D. Dawson, "Actively stabilized single-frequency vertical-external-cavity AlGaAs laser," *IEEE Photonics Technol. Lett.*, vol. 11, no. 12, pp. 1551–1553, Dec. 1999.

[38] A. Ouvrard, A. Garnac, L. Cerutti, F. Genty, and D. Romanini, "Single-frequency tunable Sb-based VCSELs emitting at 2.3 μm," *IEEE Photonics Technol. Lett.*, vol. 17, no. 10, pp. 2020–2022, Oct. 2005.

[39] A. Garnache, A. A. Kachanov, F. Stoeckel, and R. Planel, "High-sensitivity intracavity laser absorption spectroscopy with vertical-external-cavity surface-emitting semiconductor lasers," *Opt. Lett.*, vol. 24, no. 12, p. 826, Jun. 1999.

[40] E. Bertseva, A. A. Kachanov, and A. Campargue, "Intracavity laser absorption spectroscopy of N2O with a vertical external cavity surface emitting laser," vol. 351, no. January, pp. 18–26, 2002.

[41] B. Cocquelin, G. Lucas-Leclin, P. Georges, I. Sagnes, and a. Garnache, “Design of a low-threshold VECSEL emitting at 852 nm for Cesium atomic clocks,” *Opt. Quantum Electron.*, vol. 40, no. 2–4, pp. 167–173, Jan. 2008.

[42] J. Paul, Y. Kaneda, T. Wang, C. Lytle, J. V Moloney, and R. J. Jones, “Doppler-free spectroscopy of mercury at 253.7 nm using a optically pumped external-cavity semiconductor laser,” *Opt. Lett.*, vol. 36, no. 1, pp. 61–63, 2011.

[43] J. R. Paul, C. R. Lytle, Y. Kaneda, J. Moloney, T.-L. Wang, and R. J. Jones, “Optically-pumped external-cavity semiconductor lasers for precision spectroscopy and laser cooling of atomic Hg,” vol. 8606, p. 86060R–86060R–9, Feb. 2013.

[44] W. Ketterle, K. B. Davis, M. A. Joffe, A. Martin, and D. E. Pritchard, “High densities of cold atoms in a dark spontaneous-force optical trap,” *Phys. Rev. Lett.*, vol. 70, no. 15, pp. 2253–2256, 1993.

[45] P. D. Lett, W. D. Phillips, S. L. Rolston, C. E. Tanner, R. N. Watts, and C. I. Westbrook, “Optical molasses,” *J. Opt. Soc. Am. B*, vol. 6, no. 11, p. 2084, 1989.

[46] H. Katori, M. Takamoto, V. Pal’chikov, and V. Ovsiannikov, “Ultrastable Optical Clock with Neutral Atoms in an Engineered Light Shift Trap,” *Phys. Rev. Lett.*, vol. 91, no. 17, p. 173005, Oct. 2003.

[47] H. Hachisu, K. Miyagishi, S. Porsev, a. Derevianko, V. Ovsiannikov, V. Pal’chikov, M. Takamoto, and H. Katori, “Trapping of Neutral Mercury Atoms and Prospects for Optical Lattice Clocks,” *Phys. Rev. Lett.*, vol. 100, no. 5, p. 053001, Feb. 2008.

[48] M. Y. A. Raja, S. R. J. Brueck, M. Osinski, C. F. Schaus, J. G. McInerney, T. M. Brennan, and B. E. Hammons, “Resonant periodic gain surface-emitting semiconductor lasers,” *IEEE J. Quantum Electron.*, vol. 25, no. 6, pp. 1500–1512, Jun. 1989.

[49] O. G. Okhotnikov, *Semiconductor Disk Lasers: Physics and Technology*. Wiley-VCH, 2010.

[50] N. Schulz, M. Rattunde, C. Ritzenthaler, B. Rösener, C. Manz, K. Köhler, J. Wagner, and U. Brauch, “Resonant optical in-well pumping of an (AlGaIn)(AsSb)-based vertical-external-cavity surface-emitting laser emitting at 2.35 μm,” *Appl. Phys. Lett.*, vol. 91, no. 9, p. 091113, 2007.

[51] C. Stewen, K. Contag, M. Larionov, A. Giesen, and H. Hügel, “A 1-kW CW Thin Disc Laser,” vol. 6, no. 4, pp. 650–657, 2000.

[52] S. Beyertt, U. Brauch, F. Demaria, N. Dhidah, A. Giesen, T. Kübler, S. Lorch, F. Rinaldi, and P. Unger, “Efficient Gallium – Arsenide Disk Laser,” *October*, vol. 43, no. 10, pp. 869–875, 2007.

[53] A. J. Maclean, R. B. Birch, P. W. Roth, A. J. Kemp, and D. Burns, “Limits on efficiency and power scaling in semiconductor disk lasers with diamond heatspreaders,” *J. Opt. Soc. Am. B*, vol. 26, no. 12, p. 2228, Nov. 2009.

[54] J. Rautiainen, J. Lyytikäinen, A. Sirbu, A. Mereuta, A. Caliman, E. Kapon, and O. G. Okhotnikov, “2.6 W optically-pumped semiconductor disk laser operating at 1.57-μm using wafer fusion.,” *Opt. Express*, vol. 16, no. 26, pp. 21881–6, Dec. 2008.

[55] A. J. Maclean, S. Member, A. J. Kemp, S. Calvez, J. Kim, T. Kim, M. D. Dawson, S. Member, and D. Burns, “Continuous Tuning and Efficient Intracavity Second-Harmonic Generation in a Semiconductor Disk Laser With an Intracavity Diamond Heatspreader,” vol. 44, no. 3, pp. 216–225, 2008.

[56] B. Rudin, A. Rutz, M. Hoffmann, D. J. H. C. Maas, A.-R. a-R. Bellancourt, E. Gini, T. Südmeyer, and U. Keller, “Highly efficient optically pumped vertical-emitting semiconductor laser with more than 20 W average output power in a fundamental transverse mode.,” *Opt. Lett.*, vol. 33, no. 22, pp. 2719–21, Nov. 2008.

[57] V. M. Korpijärvi, M. Guina, J. Puustinen, P. Tuomisto, J. Rautiainen, A. Härkönen, A. Tukiainen, O. Okhotnikov, and M. Pessa, “MBE grown GaInNAs-based multi-Watt disk lasers,” *J. Cryst. Growth*, vol. 311, no. 7, pp. 1868–1871, Mar. 2009.

[58] C. Manz, Q. Yang, M. Rattunde, N. Schulz, B. Rösener, L. Kirste, J. Wagner, and K. Köhler, “Quaternary GaInAsSb/AlGaAsSb vertical-external-cavity surface-emitting lasers—A challenge for MBE growth,” *J. Cryst. Growth*, vol. 311, no. 7, pp. 1920–1922, Mar. 2009.

[59] M. Zorn, P. Klopp, F. Saas, a. Ginolas, O. Krüger, U. Griebner, and M. Weyers, “Semiconductor components for femtosecond semiconductor disk lasers grown by MOVPE,” *J. Cryst. Growth*, vol. 310, no. 23, pp. 5187–5190, Nov. 2008.

[60] Z. L. Liau, “Semiconductor wafer bonding via liquid capillarity,” *Appl. Phys. Lett.*, vol. 77, no. 5, p. 651, 2000.

[61] F. van Loon, A. J. Kemp, A. J. Maclean, S. Calvez, J.-M. Hopkins, J. E. Hastie, M. D. Dawson, and D. Burns, “Intracavity diamond heatspreaders in lasers: the effects of birefringence.,” *Opt. Express*, vol. 14, no. 20, pp. 9250–60, Oct. 2006.

[62] K. Pierǧciěski, D. Pierǧciěska, M. Bugajski, C. Manz, and M. Rattunde, “Influence of the Intracavity Heatspreader on the VECSEL Temperature,” 2009, pp. 0–5.

[63] A. J. Kemp, J.-M. Hopkins, A. J. Maclean, N. Schulz, M. Rattunde, J. Wagner, and D. Burns, “Thermal Management in 2.3-μm Semiconductor Disk Lasers: A Finite Element Analysis,” *IEEE J. Quantum Electron.*, vol. 44, no. 2, pp. 125–135, Feb. 2008.

[64] A. J. Kemp, G. J. Valentine, J.-M. Hopkins, J. E. Hastie, S. A. Smith, S. Calvez, M. D. Dawson, and D. Burns, “Thermal management in vertical-external-cavity surface-emitting lasers: finite-element analysis of a heatspreader approach,” *IEEE J. Quantum Electron.*, vol. 41, no. 2, pp. 148–155, Feb. 2005.

[65] H. Lindberg, M. Strassner, J. Bengtsson, and a. Larsson, “InP-Based Optically Pumped VECSEL Operating CW at 1550 nm,” *IEEE Photonics Technol. Lett.*, vol. 16, no. 2, pp. 362–364, Feb. 2004.

[66] J.-M. Hopkins, N. Hempler, B. Rösener, N. Schulz, M. Rattunde, C. Manz, K. Köhler, J. Wagner, and D. Burns, “High-power, (AlGaIn)(AsSb) semiconductor disk laser at 2.0 μm,” *Opt. Lett.*, vol. 33, no. 2, p. 201, Feb. 2008.

[67] S. Kaspar, M. Rattunde, T. Topper, R. Moser, S. Adler, C. Manz, K. Kohler, and J. Wagner, “Recent Advances in 2-μm GaSb-Based Semiconductor Disk Laser—Power Scaling, Narrow-Linewidth and Short-Pulse Operation,” *IEEE J. Sel. Top. Quantum Electron.*, vol. 19, no. 4, pp. 1501908–1501908, Jul. 2013.

[68] J. B. Rodriguez, L. Cerutti, and E. Tournié, “GaSb-based, 2.2 μm type-I laser fabricated on GaAs substrate operating continuous wave at room temperature,” *Appl. Phys. Lett.*, vol. 94, no. 2, p. 023506, 2009.

[69] J. M. Yarborough, Y.-Y. Lai, Y. Kaneda, J. Hader, J. V. Moloney, T. J. Rotter, G. Balakrishnan, C. Hains, D. Huffaker, S. W. Koch, and R. Bedford,

"Record pulsed power demonstration of a 2 μm GaSb-based optically pumped semiconductor laser grown lattice-mismatched on an AlAs/GaAs Bragg mirror and substrate," *Appl. Phys. Lett.*, vol. 95, no. 8, p. 081112, 2009.

[70] Y.-Y. Lai, J. M. Yarborough, Y. Kaneda, J. Hader, J. V. Moloney, T. J. Rotter, G. Balakrishnan, C. Hains, and S. W. Koch, "340-W Peak Power From a GaSb 2-μm Optically Pumped Semiconductor Laser (OPSL) Grown Mismatched on GaAs," *IEEE Photonics Technol. Lett.*, vol. 22, no. 16, pp. 1253–1255, Aug. 2010.

[71] D. N. Bose, "Growth and Characterization of Compound Semiconductors for Optoelectronics," *Laser News*, vol. 10, no. 2, 1999.

[72] J. Chilla, Q. Shu, H. Zhou, E. Weiss, M. Reed, and L. Spinelli, "Recent advances in optically pumped semiconductor lasers," in *Proceedings of SPIE*, 2007, pp. 645109–645109–10.

[73] J. L. a. Chilla, H. Zhou, E. Weiss, A. L. Caprara, Q.-Z. Shou, S. V. Govorkov, M. K. Reed, and L. Spinelli, "Blue & Green Optically-Pumped Semiconductor Lasers for Display," in *Proceedings of SPIE*, 2005, vol. 5740, pp. 41–47.

[74] M. Fallahi, Y. Kaneda, C. Hessenius, J. Hader, J. V. Moloney, B. Kunert, W. Stolz, S. W. Koch, J. Murray, and R. Bedford, "5-W Yellow Laser by Intracavity Frequency Doubling of High-Power Vertical-External-Cavity Surface-Emitting Laser," *IEEE Photonics Technol. Lett.*, vol. 20, no. 20, pp. 1700–1702, Oct. 2008.

[75] V. Ostroumov, C. Simon, H. Schwarze, R. von Elm, W. Seelert, and J. Lindfors, "1 W 488 nm cw air-cooled Optically Pumped Semiconductor Laser," 2008, vol. 6871, pp. 687118–687118–7.

[76] Coherent, "Short Upper State Lifetime Eliminates ' Green Problem ,' Setting the Industry Standard for Lowest Overall Noise." [Online]. Available: http://www.coherent.com/downloads/Verdi G Adv 2 - No Green Noise Final.pdf.

[77] "ULTRAFAST-LASER PUMPING: OPSL has no 'green noise,'" *Laser Focus World*, 2009.

[78] T. Baer, "Large-amplitude fluctuations due to longitudinal mode coupling in diode-pumped intracavity-doubled Nd:YAG lasers," *J. Opt. Soc. Am. B*, vol. 3, no. 9, p. 1175, Sep. 1986.

[79] M. Schafer, W. Hoyer, M. Kira, S. W. Koch, and J. V Moloney, “Influence of dielectric environment on quantum-well luminescence spectra,” *J. Opt. Soc. Am. B*, vol. 25, no. 2, p. 187, 2008.

[80] J. Hader, S. W. Koch, and J. V. Moloney, “Microscopic theory of gain and spontaneous emission in GaInNAs laser material,” *Solid. State. Electron.*, vol. 47, no. 3, pp. 513–521, Mar. 2003.

[81] J. Hader, J. V. Moloney, and S. W. Koch, “Microscopic modeling of gain and luminescence in semiconductors,” *IEEE J. Sel. Top. Quantum Electron.*, vol. 9, no. 3, pp. 688–697, May 2003.

[82] J. Hader, G. Hardesty, M. J. Yarborough, Y. Kaneda, J. V. Moloney, B. Kunert, W. Stolz, and S. W. Koch, “Predictive Microscopic Modeling of VECSELs,” *IEEE J. Quantum Electron.*, vol. 46, no. 5, pp. 810–817, May 2010.

[83] W. W. Chow and S. W. Koch, *Semiconductor-Laser Fundamentals*. Springer, 1999.

[84] M. Bennett, M. F. Schatz, H. Rockwood, and K. Wiesenfeld, “Huygens’s clocks,” *Proc. R. Soc. A Math. Phys. Eng. Sci.*, vol. 458, no. 2019, pp. 563–579, Mar. 2002.

[85] R. Adler, “A Study of Locking Phenomena in Oscillators,” *Proc. IRE*, vol. 34, no. 6, pp. 351–357, Jun. 1946.

[86] R. Kurorawa, “Injection Locking of Microwave Solid-State Oscillators,” vol. 61, no. 10, 1973.

[87] B. Razavi, “A study of injection locking and pulling in oscillators,” *IEEE J. Solid-State Circuits*, vol. 39, no. 9, pp. 1415–1424, Sep. 2004.

[88] C. J. Buczek, R. J. Freiberg, and M. L. Skolnick, “Laser injection locking,” *Proc. IEEE*, vol. 61, no. 10, pp. 1411–1431, 1973.

[89] A. D. Farinas, E. K. Gustafson, R. L. Byer, and A. I. Model, “Frequency and intensity noise in an injection-locked , solid-state laser,” vol. 12, no. 2, pp. 328–334, 1995.

[90] A. E. Siegman, *Lasers*. University Science Books, 1986.

[91] E. A. Cummings, M. S. Hicken, and S. D. Bergeson, “Demonstration of a 1-W injection-locked continuous-wave titanium:sapphire laser,” *Appl. Opt.*, vol. 41, no. 36, p. 7583, Dec. 2002.

[92] E. D. Black, “An introduction to Pound–Drever–Hall laser frequency stabilization,” *Am. J. Phys.*, vol. 69, no. 1, p. 79, 2001.

[93] C. Peucheret, “Note on Fabry-Perot Interferometers,” 2011.

[94] C. N. Man and a Brillet, “Injection locking of argon-ion lasers.,” *Opt. Lett.*, vol. 9, no. 8, pp. 333–4, Aug. 1984.

[95] B. Couillaud, a Ducasse, E. Freysz, and L. Sarger, “Experimental study of the injection-locked continous-wave ring dye laser.,” *Opt. Lett.*, vol. 9, no. 10, pp. 435–7, Oct. 1984.

[96] L. Goldberg, H. F. Taylor, J. F. Weller, and D. R. Scifres, “Injection locking of coupled-stripe diode laser arrays,” *Appl. Phys. Lett.*, vol. 46, no. 3, p. 236, 1985.

[97] L. Goldberg and J. F. Weller, “Injection locking and single-mode fiber coupling of a 40-element laser diode array,” *Appl. Phys. Lett.*, vol. 50, no. 24, p. 1713, 1987.

[98] L. Goldberg and M. K. Chun, “Injection locking characteristics of a 1 W broad stripe laser diode,” *Appl. Phys. Lett.*, vol. 53, no. 20, p. 1900, 1988.

[99] C. D. Nabors, a D. Farinas, T. Day, S. T. Yang, E. K. Gustafson, and R. L. Byer, “Injection locking of a 13-W cw Nd:YAG ring laser.,” *Opt. Lett.*, vol. 14, no. 21, pp. 1189–91, Nov. 1989.

[100] S. T. Yang, Y. Imai, M. Oka, N. Eguchi, and S. Kubota, “Frequency-stabilized, 10-W continuous-wave, laser-diode end-pumped, injection-locked Nd:YAG laser.,” *Opt. Lett.*, vol. 21, no. 20, pp. 1676–1678, Oct. 1996.

[101] K. Takeno, T. Ozeki, S. Moriwaki, and N. Mio, “100 W, single-frequency operation of an injection-locked Nd:YAG laser,” *Opt. Lett.*, vol. 30, no. 16, p. 2110, Aug. 2005.

[102] Y. Cha, K. Ko, G. Lim, J. Han, H.-M. Park, T.-S. Kim, and D.-Y. Jeong, “External-cavity frequency doubling of a 5-W 756-nm injection-locked Ti:sapphire laser,” *Opt. Express*, vol. 16, no. 7, p. 4866, Mar. 2008.

[103] S. Chiow, S. Herrmann, H. Mueller, and S. Chu, “6 W, 1 kHz linewidth, tunable continuous-wave near-infrared laser,” *Opt. Express*, vol. 17, no. 7, p. 3, Jan. 2009.

[104] Q. Zhou, L. Chen, and X. Xu, “Numerical analysis of the output power of the injection-locked cw Ti:sapphire lasers,” *Opt. Commun.*, vol. 284, no. 13, pp. 3378–3382, Jun. 2011.

[105] W. Koechner, *Solid-State Laser Engineering*, vol. 1. New York, NY: Springer New York, 2006.

[106] R. W. P. Drever, J. L. Hall, F. V. Kowalski, J. Hough, G. M. Ford, a. J. Munley, and H. Ward, “Laser phase and frequency stabilization using an optical resonator,” *Appl. Phys. B*, vol. 31, no. 2, pp. 97–105, Jun. 1983.

[107] J. M. Yarborough and J. Hobart, “No Title,” in *Proceedings of the Conference on Laser Engineering and Applications, post-deadline paper*, 1973.

[108] J. M. Yarborough and J. L. Hobart, “TUNING APPARATUS FOR AN OPTICAL OSCILLATOR,” US 3934210,1976.

[109] B. E. A. Saleh and M. C. Teich, *Fundamentals of Photonics*, 2nd editio. Wiley-Interscience, 2007.

[110] D. Burns, J.-M. Hopkins, A. J. Kemp, B. Rösener, N. Schulz, C. Manz, K. Köhler, M. Rattunde, and J. Wagner, “Recent developments in high-power short-wave mid-infrared semiconductor disk lasers,” in *Proceedings of SPIE*, 2009, vol. 7193, no. 0, pp. 719311–719311–13.

[111] M. Mangold, V. J. Wittwer, O. D. Sieber, M. Hoffmann, I. L. Krestnikov, D. a Livshits, M. Golling, T. Südmeyer, and U. Keller, “VECSEL gain characterization.,” *Opt. Express*, vol. 20, no. 4, pp. 4136–48, Feb. 2012.

[112] T. Wang, Y. Kaneda, J. M. Yarborough, J. Hader, J. V Moloney, A. Chernikov, S. Chatterjee, S. W. Koch, B. Kunert, and W. Stolz, “High-Power Optically Pumped Semiconductor Laser at 1040 nm,” vol. 22, no. 9, pp. 661–663, 2010.

[113] R. W. Fox, C. W. Oates, and L. W. Hollberg, “STABILIZING DIODE LASERS TO HIGH-FI NESSE CAVITIES,” in *Cavity-Enhanced Spectroscopies, Volume 40 (Experimental Methods in the Physical Sciences)*, vol. 40, Academic Press, 2003, pp. 1–46.

[114] “Sorbothane.” [Online]. http://www.sorbothane.com/blog/technical-data/.

[115] Y.-Y. Lai, K. Winn, J. M. Yarborough, Y. Merzlyak, and Y. Kaneda, “Injection-locked optically-pumped vertically external cavity surface emitting laser (VECSEL),” in *SPIE LASE*, 2014, p. 89660Z.

[116] K. Kawahara, “Application of High-damping Alloy M2052 *,” *Key Eng. Mater.*, vol. 319, pp. 217–223, 2006.

[117] T. Tanji, S. Moriwaki, N. Mio, T. Tomaru, T. Suzuki, and T. Shintomi, “Measurement of damping performance of M2052 alloy at cryogenic temperatures,” *J. Alloys Compd.*, vol. 355, no. 1–2, pp. 207–210, Jun. 2003.

[118] T. C. Briles, D. C. Yost, A. Cingöz, J. Ye, and T. R. Schibli, “Simple piezoelectric-actuated mirror with 180 kHz servo bandwidth.,” *Opt. Express*, vol. 18, no. 10, pp. 9739–46, May 2010.

[119] L. A. Coldren and S. W. Corzine, *Diode Lasers and Photonic Integrated Circuits*. 1995.

[120] A. E. Siegman, “Lasers,” University Science Books, 1986, p. 294.

[121] A. Sanchez, A. J. Strauss, R. L. Aggarwal, and R. E. Fahey, “Crystal growth, spectroscopy, and laser characteristics of Ti:Al2O3,” *IEEE J. Quantum Electron.*, vol. 24, no. 6, pp. 995–1002, Jun. 1988.

[122] J. Hader, T.-L. Wang, J. V. Moloney, B. Heinen, M. Koch, S. W. Koch, B. Kunert, and W. Stolz, “On the measurement of the thermal impedance in vertical-external-cavity surface-emitting lasers,” *J. Appl. Phys.*, vol. 113, no. 15, p. 153102, 2013.

[123] A. E. Siegman, “How to (Maybe) Measure Laser Beam Quality,” *Osa Tops*, vol. 17, no. October 1997, pp. 184–199, 1998.

[124] R. Paschotta, H. R. Telle, and U. Keller, “Noise of Solid-State Lasers,” in *Solid-State Lasers and Applications*, Alphan Sennaroglu, Ed. CRC Press, 2007, pp. 473–506.

[125] T. Okoshi, K. Kikuchi, and A. Nakayama, “Novel method for high resolution measurement of laser output spectrum,” *Electron. Lett.*, vol. 16, no. 16, p. 630, 1980.